

Co-Simulation of Power System Transients Using Dynamic Phasor and Electromagnetic Transient Simulators

By

Kumara Mudunkotuwa

A Thesis Submitted to the Faculty of Graduate Studies
in partial fulfilment of the requirements for the degree of
Doctor of Philosophy

Department of Electrical and Computer Engineering
Faculty of Engineering
The University of Manitoba
Winnipeg, Manitoba, Canada

Copyright © Kumara Mudunkotuwa 2018

Abstract

The purpose of this research is to develop algorithms for co-simulation using a dynamic phasor (DP) simulation program and an electromagnetic transient (EMT) simulator. The DP-EMT co-simulator offers flexibility in deciding the harmonic contents to be preserved in the dynamic phasor domain. Additionally, the co-simulator offers significant reduction in computational time of large networks compared with pure EMT simulators.

The EMT simulator models a part of the network for which fast transients are prevalent and detailed modelling is necessary. The dynamic phasor simulator models the rest of the network, which allows larger simulation steps while keeping the accuracy during low-frequency transients. Specialized algorithms are developed for accurate mapping between instantaneous EMT samples and counterpart dynamic phasors. The thesis describes the mathematical foundations of the DP-EMT interface and provides demonstrations using illustrative examples. Several large networks are also studied to assess the accuracy of the interface and the performance in reducing the computational time.

The findings of the thesis demonstrate that the co-simulation methods developed enable simulation of large electrical networks with adjustable accuracy in terms of retention of high-frequency transients via selection of the time-step ratio of the two simulators. The results also confirm that significant computational savings, which may even exceed an order of magnitude, may be expected in co-simulation of large networks. The findings of the thesis show a clear contribution to the advancement of transient simulation of complex modern power systems.

Acknowledgments

I would like to extend my sincere gratitude to Dr. Shaahin Filizadeh for his continuous encouragement, guidance, and valuable suggestions. I consider myself privileged to have had the opportunity to work under his supervision. I would also like to thank my advisory committee members for their comments and feedbacks throughout the course of this work.

I would like to express my sincere thanks to Dr. Dharshana Muthumuni for encouraging me to undertake Ph.D. studies and also my colleagues at the Manitoba HVDC Research Centre for their support and valuable discussions on research topics.

I must also thank the academic and technical staff of the Department of Electrical and Computer Engineering for their help. I am also grateful to the Natural Science and Engineering Research Council (NSERC), and the Faculty of Graduate Studies for various forms of support they provided.

This acknowledgement will not be complete without thanking my family. I extend my gratitude to my parents, and to my sisters. Finally, my sincere thanks go to my wife, Tharanga, and my two daughters, Senuli and Nethali, for their patience, understanding, love, and support during the hard times.

Contents

Front Matter

| | |
|---|-----------|
| Contents | III |
| List of Tables | VI |
| List of Figures | VII |
| List of Acronyms | XI |
| 1 Introduction | 1 |
| 1.1 Background | 1 |
| 1.2 Research Motivation | 3 |
| 1.3 Objectives | 4 |
| 1.4 Thesis Organization | 5 |
| 2 Mathematical Foundations of Dynamic Phasor Modeling Approach | 6 |
| 2.1 Introduction | 6 |
| 2.2 History of the Dynamic Phasor Approach | 6 |
| 2.3 Fundamentals of the Dynamic Phasor Concept | 8 |
| 2.4 Frequency Shifting | 10 |
| 2.4.1 Frequency-Adaptive Simulation of Transients | 11 |
| 2.5 Quasi-Periodic Modeling Approach | 12 |
| 2.5.1 Relationship between $\mathbf{X}(t)$ and $\langle x \rangle_h(t)$ | 14 |
| 2.6 Modeling of Electrical Networks | 15 |
| 2.6.1 Dynamic Phasor-Based Network Component Models | 17 |
| 2.6.2 Nodal Analysis | 20 |
| 2.7 DP and EMT Comparison | 20 |
| 3 Interfacing DP and EMT Simulators | 23 |

| | | |
|----------|---|-----------|
| 3.1 | Introduction..... | 23 |
| 3.2 | Subsystem Definition..... | 24 |
| 3.3 | Coupling Techniques | 24 |
| 3.4 | Partitioning at Transmission Lines | 26 |
| 3.5 | DP-EMT Interface | 31 |
| 3.5.1 | Instantaneous EMT to DP Conversion - Analytic Signal Approach | 32 |
| 3.5.2 | Instantaneous EMT to DP Conversion - Fourier Approach..... | 33 |
| 3.5.3 | Representing only by the Fundamental..... | 33 |
| 3.5.4 | Improvement by Including the DC Offset | 35 |
| 3.6 | A Novel DP Extraction Technique | 37 |
| 3.6.1 | Testing of the Proposed DP Extraction Technique..... | 39 |
| 3.6.2 | Simulation Example..... | 42 |
| 3.6.3 | Introducing Damping | 43 |
| 3.6.4 | TS-EMT Interfacing..... | 44 |
| 3.7 | Chapter Summary and Contribution | 46 |
| 4 | Multi-Rate DP-EMT Co-Simulation | 47 |
| 4.1 | Introduction..... | 47 |
| 4.2 | Use of Transmission Line Delay..... | 48 |
| 4.2.1 | Simulation of Large Networks..... | 51 |
| 4.3 | Use of MATE Technique..... | 54 |
| 4.3.1 | MATE Formulation | 55 |
| 4.3.2 | Adapted MATE Formulation for the DP-EMT | 58 |
| 4.3.3 | Multi-Rate DP-EMT Solution using MATE | 60 |
| 4.3.4 | Simulation of a Large Network..... | 63 |
| 4.4 | Chapter Summary and Contribution | 65 |
| 5 | Simulation Examples | 66 |
| 5.1 | Introduction..... | 66 |
| 5.2 | Synchronous Machine Model | 67 |
| 5.2.1 | Validation of the CP-VBR Synchronous Machine Model..... | 68 |

| | | |
|----------|---|-----------|
| 5.3 | Simulation Example 1 | 72 |
| 5.3.1 | Speed-Up Gain..... | 77 |
| 5.4 | Simulation Example 2..... | 78 |
| 5.4.1 | Speed-Up Gain..... | 83 |
| 5.4.2 | Impact on the Speed-Up Gain of the DP Network | 84 |
| 6 | Contributions, Conclusions and Recommendations for Future Work | 86 |
| 6.1 | Introduction..... | 86 |
| 6.2 | Main Contribution of the Thesis | 87 |
| 6.2.1 | Thesis Publications | 88 |
| 6.3 | Conclusions and Future Work | 88 |
| 6.3.1 | Suggestions for Future Work..... | 91 |
| | Bibliography | 92 |
| | Appendix-A: Quasi-Periodic Approach..... | 101 |
| | Appendix-B: VBR Formulation..... | 105 |
| | Appendix-C: CP-VBR Formulation | 107 |
| | Appendix-D: Mapping between $qd0$ and abc | 109 |
| | Appendix-E: IEEE Test Systems Data | 110 |

List of Tables

| | |
|--|----|
| Table 2-1 Dynamic phasor and discretized equivalent companion models of basic circuit elements | 19 |
| Table 2-2 Per-unit impedance of line segments (base values: 230 kV/100 MVA) | 21 |
| Table 4-1 CPU time to complete a 10 s simulation | 54 |
| Table 5-1 Per-unit impedance of network elements (base values: 230 kV/ 100 MVA).. | 69 |
| Table 5-2 Transmission line (B ₈ to B ₉) positive-sequence parameters..... | 72 |
| Table 5-3 Simulation time comparison..... | 77 |
| Table 5-4 Rated values of Machines..... | 79 |
| Table 5-5 AVR and excitation system parameters | 80 |

List of Figures

| | |
|---|----|
| Figure 2-1 Fourier spectrum of a bandpass signal | 10 |
| Figure 2-2 Simple test system..... | 21 |
| Figure 2-3 Current through line-segment π_2 of the network in Figure 2-2 using two separate simulators: an EMT simulator and a DP simulator..... | 22 |
| Figure 3-1 Time axis of a TS-EMT hybrid simulation | 25 |
| Figure 3-2 TS-EMT boundary condition | 25 |
| Figure 3-3 Equivalent impedance model of lossless line..... | 27 |
| Figure 3-4 Decoupled simple test system | 30 |
| Figure 3-5 Current through line-segment π_2 of the network in Figure 2-2 (using an EMT simulator) and Figure 3-4 (using two separate simulators: an EMT simulator and a DP simulator) | 30 |
| Figure 3-6 Current through line-segment π_2 of the network in Figure 3-4..... | 35 |
| Figure 3-7 Current through line-segment π_2 of the network in Figure 3-4..... | 36 |
| Figure 3-8 Full augmentation of the fundamental dynamic phasor | 38 |
| Figure 3-9 Test system for the proposed dynamic phasor extraction technique..... | 39 |
| Figure 3-10 Test for magnitude jump and phase jump | 40 |
| Figure 3-11 Test for DC offset and harmonic..... | 41 |
| Figure 3-12 Current through line-segment π_2 of the network in Figure 3-4..... | 42 |
| Figure 3-13 DP extraction with damping..... | 43 |
| Figure 3-14 Current through line-segment π_2 in TS-EMT co-simulation..... | 45 |
| Figure 4-1 DP-EMT multi-rate simulation strategy using traveling delay | 49 |

| | |
|--|----|
| Figure 4-2 Multi-rate simulation results of the network in Figure 3-4..... | 50 |
| Figure 4-3 IEEE 12-bus system with the DP-EMT interfaces at buses 1 and 5 | 52 |
| Figure 4-4 Simulation results of the IEEE 12-bus system using the DP-EMT simulator | 53 |
| Figure 4-5 Two subsystems connected by three linking branches | 55 |
| Figure 4-6 Partitioned DP network..... | 59 |
| Figure 4-7 Thévenin equivalent representation of the System-A in Figure 4-6 | 60 |
| Figure 4-8 Time line of DP-EMT multi-rate simulation strategy using MATE..... | 60 |
| Figure 4-9 Multi-rate simulation results of the network in Figure 3-4..... | 62 |
| Figure 4-10 Segmented IEEE 118-bus test system..... | 63 |
| Figure 4-11 Instantaneous current and voltage waveforms at bus 9 (top two plots) and 8 (bottom two plots)..... | 64 |
| Figure 5-1 Simple test system with a synchronous machine | 69 |
| Figure 5-2 Comparison of synchronous machine models in DP (CP-VBR) and EMT (PSCAD Norton Current Injection) | 70 |
| Figure 5-3 Comparison at different time-step | 71 |
| Figure 5-4 Segmented IEEE 118-bus test system with a wind farm | 73 |
| Figure 5-5 Type-4 windfarm model..... | 73 |
| Figure 5-6 Instantaneous current and voltage waveforms at bus 10 (top two plots) and bus 30 (bottom two plots) for EMT (20- μ s) and DP-EMT (20- μ s: 20- μ s) simulations | 75 |
| Figure 5-7 Instantaneous current and voltage waveforms at bus 10 (top two plots) and bus 30 (bottom two plots) for EMT (20- μ s) and DP-EMT (500- μ s: 20- μ s) simulations | 76 |
| Figure 5-8 Terminal voltage (rms, fundamental), and real and reactive power at the windfarm terminal for EMT (20- μ s) and DP-EMT (500- μ s:20- μ s) simulations..... | 76 |

| | |
|--|----|
| Figure 5-9 IEEE 39-bus system with the DP-EMT interfaces at bus 26 | 78 |
| Figure 5-10 DP-EMT interface (only part of the network is shown) | 80 |
| Figure 5-11 Simple PI-based AVR and excitation system | 80 |
| Figure 5-12 Waveforms at the synchronous machine at bus 36 | 81 |
| Figure 5-13 Waveforms at the synchronous machine at bus 37 | 82 |
| Figure 5-14 CPU Time variation with the DP time-step, IEEE 39-bus system..... | 83 |
| Figure 5-15 CPU Time variation with the DP time-step, IEEE 118-bus system..... | 85 |

List of Symbols

| | |
|------------------------------|---|
| Z | Impedance |
| Y | Admittance |
| ω | Angular frequency (rad/s) |
| ω_c | Base angular frequency or carrier angular frequency (rad/s) |
| f | Frequency (Hz) |
| f_c | Base frequency or carrier frequency (Hz) |
| Z_c | Characteristic impedance |
| Y_c | Characteristic admittance |
| τ | Transmission time-delay |
| Δt | Simulation time-step |
| t | Time |
| j | Imaginary unit |
| $i(t)$ | Instantaneous current |
| $v(t)$ | Instantaneous voltage |
| $\mathbf{I}(t)$ | Current dynamic phasor |
| $\mathbf{V}(t)$ | Voltage dynamic phasor |
| $\mathbf{I}_{\text{his}}(t)$ | History current dynamic phasor |
| \Re | Real part of a complex number |
| \mathcal{D} | dynamic phasor operator |
| \mathcal{F} | Fourier Transform |

List of Acronyms

| | |
|--------|---|
| CPU | Central Processing Unit |
| DP | Dynamic Phasor |
| DP-EMT | Dynamic Phasor - Electromagnetic Transient |
| EMT | Electromagnetic Transient |
| FDNE | Frequency Dependent Network Equivalent |
| FAST | Frequency - Adaptive Simulation of Transients |
| FFT | Fast Fourier Transform |
| MATE | Multi-Area Thévenin Equivalent |
| TS | Transient Stability |
| TS-EMT | Transient Stability - Electromagnetic Transient |

Chapter 1

Introduction

1.1 Background

Power system engineers use different simulation platforms for various types of analysis and design studies. These platforms differ in the way the system components are modelled, the extent of harmonics considered, and their resulting computational intensity. For example, transient stability type (TS-type) simulation platforms assume operation under quasi-steady-state conditions [1], [2], and neglect fast electromagnetic transients. Differential equations of dynamic devices in the network are formed and solved in conjunction with constant admittance-matrix equations (i.e., conventional phasor representation) of the network. TS-type simulators represent the low-frequency electromechanical dynamics of rotating devices [3] and fundamental-frequency behaviour of devices such as HVDC converters. These simulators enable the use of large simulation time-steps (milliseconds), which is essential in order to be able to simulate large networks consisting of thousands of nodes in a computationally affordable manner.

1.1 Background

On the other hand, electromagnetic transient (EMT) simulators consider a far more detailed representation of network elements and are particularly suited for analysis of fast switching transients or high-frequency power-electronic converters. Typical simulation time-steps in EMT studies (microseconds) are significantly smaller than TS-type simulations. Therefore, EMT simulations are computationally more demanding than TS-type simulators and are normally used in systems that are much smaller in size.

EMT simulation of large electrical networks is a challenging task due to the inherent computational intensity of EMT models and solution methods. Several methods have been proposed to extend the applicability of EMT simulators in the study of large and complex power systems. Simplifications to individual component models and systems, which is widely applied to high-frequency power electronic converters and is referred to as averaging, is one such method [4]-[6]. Alternatively, dynamic equivalents represent a portion of a large network by aggregating several components in a reduced-order model to relieve the computational intensity of simulation of the whole network [7]-[9]. Dynamic equivalents often yield substantial reduction in the number of nodes to be included in the system's equivalent admittance-matrix, which in turn relieves matrix inversion and computation tasks. In both the averaged-value and dynamic equivalent modeling approaches, a single EMT simulator will solve the entire network containing regular EMT-type and averaged or dynamic equivalent models.

Hybrid simulation environments have been developed to address the bottlenecks of conventional simulators [2], [10]-[14] by interfacing two or more simulators. Hybrid TS-EMT [3] simulation involves partitioning a large system into two or more subsystems. Small subsystems in which a detailed representation is required are modelled in an EMT-

1.2 Research Motivation

type simulator, while large subsystems that do not demand a detailed representation and in which fast transients can reasonably be ignored are modelled in a TS-type simulator. Such segmentation allows a hybrid simulator to avoid unnecessarily detailed EMT-type modelling of large systems while retaining details where necessary. Other examples of hybrid simulators are also reported, including between finite-element analysis and EMT simulation [15], and software and processor-in-the loop simulation [16], [17]. Hybrid real-time simulation environments are reviewed in [18].

1.2 Research Motivation

As described in the previous section, a hybrid simulation approach enables EMT-type simulation of large networks. Most of the research presented in the literature on hybrid simulation has been focused on TS-EMT interfaces. Dynamic phasors have attracted a great deal of attention for their ability to better represent a larger frequency spectrum of system transients than conventional phasors [19], [20]. Advantages of dynamic phasor (DP)-EMT co-simulation were discussed in [21]. A method to simulate natural (EMT) and envelop (DP) waveforms in one simulator is discussed in [23]. Direct interfacing of the DP and EMT simulators was recently explored in [24], which was concluded with recommendations for further research to investigate instability issues encountered.

The accuracy of the hybrid simulation between EMT and TS-type simulators is improved by using a dynamic phasor based interface model between the EMT and TS simulators [25]. Since the DP approach is an accurate way of simulating the electromagnetic transients in the neighborhood of fundamental frequency [20] and the TS-

1.3 Objectives

type simulation completely neglects electromagnetic transients of the network, one can argue that the DP-EMT co-simulation approach should offer a higher degree of accuracy than the TS-EMT hybrid simulation. Further, DP-EMT simulation reduces the computational time substantially by sacrificing a small level of accuracy at high frequencies; as a result DP simulators can capture slow transients accurately at larger simulation time-step.

These aforementioned factors have motivated this research to develop algorithms to interface a DP simulator with an EMT-type simulator while maintaining the accuracy of the simulation results as much as possible and also to ensure that the numerical stability of the co-simulator is preserved under various system conditions.

1.3 Objectives

The principal objective of this research is to develop algorithms to co-simulate dynamic phasor and EMT programs efficiently while maintaining numerical stability and accuracy.

The research goals pursued are as follows:

- a) To perform literature review on various concepts related to DP modeling. Further, to continue investigation on existing TS-EMT and DP-EMT co-simulation techniques;
- b) To implement a co-simulator (prototype) to simulate electrical networks using both EMT and DP approaches, and to validate the prototype against a commercial-grade EMT simulator (PSCAD/EMTDC);

1.4 Thesis Organization

- c) To develop a technique to extract the dynamic phasor equivalent of an arbitrary signal efficiently and accurately;
- d) To develop a multi-rate technique to co-simulate the DP and EMT simulators at two different time-steps;
- e) To extend the co-simulation technique to achieve large simulation time-steps (e.g., 1000- μ s or more) for the DP simulator;
- f) To investigate the performance of the DP-EMT co-simulator on large electrical systems (such as the IEEE 118-bus system) with various dynamic devices including power electronic converters and synchronous machines.

1.4 Thesis Organization

This thesis consists of six chapters. Chapter 2 explains the findings of the literature survey on dynamic phasor concept, mathematical formulations, and modeling approaches in network simulation. Chapter 3 describes a DP-EMT interfacing technique using a generic transmission line interface, including mathematical foundations and a novel DP extraction technique; it also demonstrates them using an illustrative example and compares the results with benchmark EMT simulation results. Chapter 4 proposes two multi-rate DP-EMT co-simulation approaches with illustrative examples. Chapter 5 demonstrates the application of the proposed co-simulation approaches to simulate moderately large electrical systems with dynamic devices. Chapter 6 presents thesis contributions, conclusions, and recommendations for future work.

Chapter 2

Mathematical Foundations of Dynamic Phasor Modeling Approach

2.1 Introduction

This chapter provides a brief history of the time-varying phasor concept in power system simulation. Further, fundamental and contemporary concepts of dynamic phasors are discussed. Afterwards it is shown that the dynamic phasor modelling approach can be employed to represent passive electrical components in nodal analysis of electric circuits. This representation is then compared with the standard EMT approach. The chapter is concluded with simulation results of selected example case studies.

2.2 History of the Dynamic Phasor Approach

In the middle of the last century, time-varying complex signals were first introduced in communication theory in order to unambiguously define the amplitude and phase of instantaneous real signals [26]. Thereafter, the time-varying phasor concept, also known as

2.2 History of the Dynamic Phasor Approach

the analytical signal approach, was used in many areas of signal processing and communication engineering.

The steady-state phasor concept was introduced at the turn of the 20th century to analyze electrical circuits under sinusoidal steady state operation [27], [28]. Later, a quasi-steady-state approach was used in transient stability-type simulation, where electrical quantities were assumed to be varying slowly to model network elements using conventional phasor representation [31]. However, the time-varying phasor concept was not used by power system engineers until early 1990's. Significant application of this concept in power engineering field was focused on analyzing quasi-periodic operating conditions of power-electronic converters (e.g., dc/dc converters), which was also known as generalized state-space averaging technique [29]. This modeling approach was used to obtain an averaged circuit model of a power electronic converter with an arbitrary degree of accuracy. The waveforms of the converter circuit are approximated over a sliding window of fixed length using Fourier series expansion, wherein the complex Fourier coefficients are time-varying phasors. The inherent frequency-selectivity of this averaging technique [30] allows the model's accuracy to be controlled by choosing a proper value for the harmonic orders included.

Although the averaging technique described above can be considered as the first significant application of the time-varying phasor concept in power engineering, the usefulness of the concept to compute power system transients was first studied in [31]. This paper established the required mathematical formulations and also proved that time-

2.3 Fundamentals of the Dynamic Phasor Concept

varying phasors can be used to accurately compute fast electromagnetic transients in linear electrical networks.

The time-varying phasor concept later evolved to be known as ‘dynamic phasor’ [32], [33] or ‘shifted-frequency-analysis’ [20] approaches. This thesis uses the term ‘dynamic phasor’ (DP in short) to refer to any time-varying phasor quantity in power system simulation.

2.3 Fundamentals of the Dynamic Phasor Concept

An arbitrary time-varying real signal $x(t)$ can be written in the form shown in (2-1) for a given base frequency ω_c .

$$x(t) = a(t) \cos(\omega_c t + \phi(t)) \quad (2-1)$$

where $a(t)$ and $\phi(t)$ are instantaneous magnitude and phase, respectively [19]. In addition, it is often advantageous to write (2-1) as the real part of a complex signal with amplitude $a(t)$ and phase $\phi(t)$ such that

$$x(t) = \Re[a(t)e^{j\phi(t)}e^{j\omega_c t}]. \quad (2-2)$$

A complex signal $\underline{x}(t)$ can be introduced such that

$$\underline{x}(t) = a(t)e^{j\phi(t)}e^{j\omega_c t}. \quad (2-3)$$

As the carrier term (i.e., $e^{j\omega_c t}$) in (2-3) does not contain any additional information, the original $x(t)$ signal can be reproduced by knowing only the term $a(t)e^{j\phi(t)}$ [34]. This term represents the dynamic phasor of the real signal $x(t)$ with respect to the base frequency [35]. The process of obtaining the dynamic phasor component from $\underline{x}(t)$ by eliminating

2.3 Fundamentals of the Dynamic Phasor Concept

the carrier term is also described as the frequency-shifting operation [20], [35]. In addition, this thesis uses (i) the dynamic phasor operator, \mathcal{D} , to denote the shifting operation by f_c , and (ii) capital bold letters to represent any dynamic phasor quantities.

$$\mathbf{X}(t) = \mathcal{D}[\underline{x}(t)] = a(t)e^{j\phi(t)} \quad (2-4)$$

It is straightforward to show that any frequency variations may be represented as a phase shift and included in dynamic phasors obtained using a fixed base-frequency. In order to show this, assume the frequency of the signal given in (2-1) varies by $\Delta\omega$:

$$x_1(t) = a(t)\cos((\omega_c + \Delta\omega)t + \phi(t)) \quad (2-5)$$

Alternatively, one can re-write (2-5) as follows:

$$x_1(t) = a(t)\cos(\omega_c t + (\Delta\omega t + \phi(t))) \quad (2-6)$$

It is then straightforward to notice that a dynamic phasor at the fundamental frequency of ω_c can be written for (2-6) as follows:

$$\mathbf{X}_1(t) = a(t)e^{j(\phi(t) + \Delta\omega t)} = \mathbf{X}(t)e^{j\Delta\omega t} \quad (2-7)$$

This shows that waveforms that may experience frequency variations may still be represented using properly shifted dynamic phasors at a constant base-frequency. Equation (2-8) can be obtained by differentiating (2-3) with respect to time as follows:

$$\mathcal{D}\left[\frac{d\underline{x}(t)}{dt}\right] = \frac{d\mathcal{D}[\underline{x}(t)]}{dt} + j\omega\mathcal{D}[\underline{x}(t)] \quad (2-8)$$

2.4 Frequency Shifting

A dynamic phasor given as in (2-4) can be used to represent fast electromagnetic transients in linear electrical networks without any limitation enforced by the frequency spectrum of the transients [31]. However, in order to take full advantage of the dynamic phasor approach, larger simulation time-steps should be used. If the frequency content of the real signal $x(t)$ concentrates around the base frequency (i.e., carrier f_c), then the frequency content of the dynamic phasor will concentrate around the origin of the frequency spectrum [21], [33] and [35].

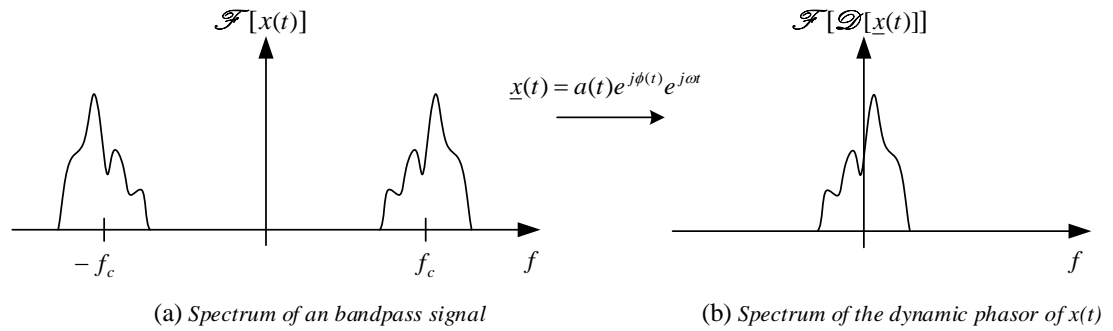


Figure 2-1 Fourier spectrum of a bandpass signal

The frequency spectrum of the complex signal $\underline{x}(t)$ in (2-3) can be shifted by the frequency f_s , which is referred to as shift frequency, as follows:

$$[\underline{x}(t)]_{\text{shift_by_}f_s} = \underline{x}(t)e^{-j\omega_s t}. \quad (2-9)$$

The carrier frequency or the base frequency of a typical power system is 60 or 50 Hz. Typically electromechanical transients followed by disturbances are concentrated around the base frequency [36]. If the shift frequency of such a signal is made equal to the carrier frequency of the signal (i.e., $f_s = f_c$), then the shifted waveforms create bandpass signals

2.4 Frequency Shifting

of narrow bandwidth where the Fourier spectrum concentrates around the origin [37].

According to (2-3), (2-4) and (2-9), a dynamic phasor is a frequency shifted signal of $\underline{x}(t)$ by f_c .

$$[\underline{x}(t)]_{\text{shift_by_}f_c} = \mathcal{D}[\underline{x}(t)] = \mathbf{X}(t) \quad (2-10)$$

As the frequency spectrum of the dynamic phasor of a slowly varying electromechanical transient signal concentrates around the origin, larger time-steps can be used to accurately capture slow transients while compromising the accuracy of the fast electromagnetic transients.

2.4.1 Frequency-Adaptive Simulation of Transients

The frequency-adaptive simulation of transients (FAST) concept proposed in [23] shows a methodology to simulate both natural and envelope waveforms in one simulator. This approach uses the shift frequency as a simulation parameter in addition to the time-step. When simulation of a transient requires high resolution, for instance after a disturbance such as a fault, the natural waveform is tracked by selecting a shift frequency of zero (i.e., $f_s = 0$) and a small time-step. In this sense the simulator works as an EMT simulator. Once the frequency contents of the waveforms start to concentrate around the carrier frequency, then the shift frequency is selected equal to the carrier frequency (i.e., $f_s = f_c$) and larger time-steps are selected. In this situation the simulator performs as a DP simulator. The FAST algorithm uses recursive discrete Fourier transform (RDFT) to determine the frequency contents of the waveforms. Further it recalculates the nodal admittance matrix

2.5 Quasi-Periodic Modeling Approach

and reinitializes the system to ensure smooth transition between the two simulating regimes.

The FAST approach switches between EMT and DP simulating regimes during a single simulation run. However, the co-simulation approach described in this thesis partitions the system so as to simulate a part of the system in EMT and another part in DP simultaneously. The FAST approach may face difficulty in a situation where proprietary models from vendors (e.g., wind turbines) are involved, as both EMT and corresponding dynamic phasor models must be available to switch between. Also in case of transitions (e.g., EMT to DP), the substituting model must be reinitialized in a condition where the network transients are not settled; such initialization processes will be difficult to implement with the modeling differences in the DP and EMT domains. Additionally, the co-simulation approach facilitates interfacing of an external DP simulator to an existing EMT simulator without introducing structural changes to the programs.

2.5 Quasi-Periodic Modeling Approach

Any periodic function $x(t)$ with period time T , i.e. $x(t) = x(t + ht)$ for any integer h can be written as infinite Fourier series [38]. Using complex exponential functions, the Fourier series is written in complex form as shown in (2-11).

$$x(t) = \sum_{h=-\infty}^{+\infty} X_h e^{j\omega_h t} \quad (2-11)$$

The complex Fourier coefficient X_h in (2-11) is time-invariant as $x(t)$ is periodic. However, power system quantities are not strictly periodic unless in steady state. The

2.5 Quasi-Periodic Modeling Approach

notion of Fourier expansion of a periodic waveform can be extended to waveforms without strict periodicity if a sliding window of time is considered, over which a portion of the waveform is viewed [29]. Consider an arbitrary signal $x(t)$ and a sliding window of length T , which at time t covers the interval $(t-T, t]$. The Fourier series expansion of $x(t)$ over this window is shown below:

$$x(t-T+s) = \sum_{h=-\infty}^{+\infty} \langle x \rangle_h(t) e^{j\frac{2\pi}{T}h(t-T+s)} \quad (2-12)$$

where $s \in (0, T]$ and,

$$\langle x \rangle_h(t) = \frac{1}{T} \int_0^T x(t-T+s) e^{-j\frac{2\pi}{T}h(t-T+s)} ds \quad (2-13)$$

The complex Fourier coefficients $\langle x \rangle_h(t)$ in (2-12) are time-variant as the interval under consideration slide as a function of time [29]. In case the sliding window passes over a periodic waveform where the period is T , complex Fourier coefficients becomes time-invariant. Conversely, these Fourier coefficients become time-variant when the sliding window passes over a non-periodic waveform. In that case, each complex coefficient is a dynamic phasor that describes the time-evolution of the h -th harmonic of $x(t)$ over the considered window, as shown in (2-12). It is observed readily that for waveforms with strict periodicity, the resulting dynamic phasors are identical to the ones obtained by conventional Fourier series expansion. The above formulation is widely used in the analysis of power-electronic converters under quasi-periodic operating conditions and is referred to as generalized state-space averaging [29]. It is straightforward to note that once the Fourier components of a signal are obtained, one can opt to use a small number of the constituent harmonics in a low-frequency (averaged) representation of the signal. The

2.5 Quasi-Periodic Modeling Approach

dynamic phasor approach presented in [21] approximates the original waveform $x(\cdot)$ using a subset of coefficients of the Fourier series as follows:

$$x(t-T+s) \approx \sum_{h \in K} \langle x \rangle_h(t) e^{j \frac{2\pi}{T} h(t-T+s)} \quad s \in (0, T], \quad (2-14)$$

where K is the set of Fourier coefficients approximating the original waveform.

It must be noted that selection of a fixed window-length, T , in (2-12) does not pose a restriction on the waveform frequency. In other words, a fixed window-length does not imply fixed frequency. This is important when analyzing quasi-periodic waveforms that may experience frequency variations, such as those in a power system during frequency swings.

In applying the Fourier operator, the following two properties often prove useful. (2-15) describes the dynamic phasor of the derivative of a signal; (2-16) shows the dynamic phasor representation of the product of two signals and is widely used in the analysis of power-electronic converters where multiplicative switching functions are used to mathematically describe a converter's input-output relationship [29].

$$\left\langle \frac{dx(t)}{dt} \right\rangle_h = \frac{d}{dt} \langle x \rangle_h(t) + jh\omega_c \langle x \rangle_h(t) \quad \omega_c = 2\pi/T \quad (2-15)$$

$$\langle x \cdot y \rangle_h = \sum_{i=-\infty}^{+\infty} \langle x \rangle_{h-i} \langle y \rangle_i \quad (2-16)$$

2.5.1 Relationship between $\mathbf{X}(t)$ and $\langle x \rangle_h(t)$

Of importance is that the dynamic phasor $\langle x \rangle_h(t)$ in (2-12) is a time-averaged quantity over a sliding window of period T . On the other hand, $\mathbf{X}(t)$ in (2-4) is not a time-averaged

2.6 Modeling of Electrical Networks

quantity. Also, $\langle x \rangle_h(t)$ is represented with respect to the base frequency $h\omega_c$, whereas $\mathbf{X}(t)$ is represented with respect to the base frequency ω_c . Except a situation wherein $x(t)$ is purely sinusoidal, (2-12) shows the requirement of more than one time-averaged dynamic phasor variable to represent the overall dynamics of $x(t)$. However, $\mathbf{X}(t)$ represents the overall dynamics of the $x(t)$ irrespective of the frequency content.

In order to understand how $\langle x \rangle_h(t)$ and $\mathbf{X}(t)$ are interrelated, the infinite series in (2-12) can be expanded and rearranged as follows:

$$x(t-T+s) = \Re \left[\left(\langle x \rangle_0(t) e^{-j\omega_c(t-T+s)} + 2 \sum_{h=1}^{\infty} \langle x \rangle_h(t) e^{j(h-1)\omega_c(t-T+s)} \right) e^{j\omega_c(t-T+s)} \right] \quad (2-17)$$

This is similar to (2-2) and hence the dynamic phasor of the $x(t)$ can be expressed in terms of the $\langle x \rangle_h(t)$ as shown in (2-18).

$$\mathbf{X}(t-T+s) = \langle x \rangle_0(t) e^{-j\omega_c(t-T+s)} + 2 \sum_{h=1}^{\infty} \langle x \rangle_h(t) e^{j(h-1)\omega_c(t-T+s)} \quad (2-18)$$

Equation (2-18) shows a way to find the dynamic phasor $\mathbf{X}(t)$ of an arbitrary signal $x(t)$ using the Fourier approach.

2.6 Modeling of Electrical Networks

The solution of a linear electrical network can be found by applying Laplace transformation to a set of linear differential equations that represent the network's dynamics. The result is a system of linear algebraic equations where the solution can be taken in Laplace domain and transferred back to the time domain using the inverse Laplace transformation. This

2.6 Modeling of Electrical Networks

process requires an excessive amount of computational time when the network is large [39].

State-space and nodal analysis methods are the most common network equation formulation techniques used to compute electromagnetic transients in power system [40]. In the state-space technique, network dynamics are represented by a set of first-order differential equations [41]. However, this formulation process needs extensive processing time when the network size is large [42]. Systematic approaches for network formulation using topology theory and the concept of a normal tree are presented in [39], [42]. Once the formulation is done, a suitable numerical integration technique can be used to find state variables as a function of time. State matrices are not dependent on the simulation time-step. Therefore, the time-step can be varied during a simulation without having to recalculate the state matrices [43].

EMT-type programs use nodal analysis techniques together with the companion circuit concept, which makes use of trapezoidal integration scheme to model inductors and capacitors using resistors and current sources [44]. This approach generates an equivalent conductance matrix that is highly sparse in nature; additionally the time-step appears in the matrix elements. This matrix is factorized (triangularized) to solve the system of linear equations for nodal voltages. In case of switching events, the conductance matrix has to be re-factorized. As the time-step term appears in the elements of the conductance matrix, the conductance matrix has to be recalculated if the time-step is varied. As a result, EMT simulators typically run at a fixed time-step to avoid runtime matrix recalculations and re-factorization. This solution approach can be applied to obtain the solution of a network

2.6 Modeling of Electrical Networks

modeled in the dynamic phasor domain. The following sub-sections discuss this approach in detail.

2.6.1 Dynamic Phasor-Based Network Component Models

The voltage and current relationship of a resistor in the dynamic phasor domain is as follows:

$$\mathbf{V}(t) = R \mathbf{I}(t) \quad (2-19)$$

The time-domain voltage-current relationships of inductors and capacitors are given by differential equations. The differential equation that describes the voltage and current relationship of an inductor is expressed as:

$$v(t) = L \frac{di(t)}{dt} \quad (2-20)$$

Equation (2-20) can be converted into dynamic phasor form by introducing the complex signals $\underline{v}_L(t)$ and $\underline{I}_L(t)$ in the form of (2-3) as follows:

$$\underline{v}(t) = L \frac{d\underline{i}(t)}{dt} \quad (2-21)$$

The dynamic phasor form of (2-20) can be obtained by employing the dynamic phasor operation on (2-21) and using the relationships in (2-4) and (2-8) as follows:

$$\mathbf{V}(t) = L \frac{d \mathbf{I}(t)}{dt} + j\omega_c L \mathbf{I}(t) \quad (2-22)$$

where, $\mathbf{V}(t)$ and $\mathbf{I}(t)$ are the dynamic phasor quantities of instantaneous quantities $v(t)$ and $i(t)$, respectively.

Dynamic phasors are complex-valued functions of a real variable t (i.e., time). Further, (2-22) is a continuous function and hence it can be discretized using Dommel's numerical

2.6 Modeling of Electrical Networks

integration substitution technique. This thesis uses the trapezoidal integration technique for the numerical integrator substitution due to its simplicity, stability, and reasonable accuracy in most circumstances [43]. The discretized form of (2-22) using the trapezoidal method is shown follows:

$$\mathbf{I}(t) = \left[\frac{\Delta t/2L}{1 + j\omega_c \Delta t/2} \right] \mathbf{V}(t) + \left[\frac{\Delta t/2L}{1 + j\omega_c \Delta t/2} \right] \mathbf{V}(t - \Delta t) + \left[\frac{1 - j\omega_c \Delta t/2}{1 + j\omega_c \Delta t/2} \right] \mathbf{I}(t - \Delta t) \quad (2-23)$$

In (2-23), $\mathbf{I}(t - \Delta t)$ and $\mathbf{V}(t - \Delta t)$ are values from the previous time-step. Therefore, (2-23) can be written in the form of a Norton equivalent (or a companion model) similar to an EMT model as follows:

$$\mathbf{I}(t) = \mathbf{YV}(t) + \mathbf{I}_{\text{his}}(t), \quad (2-24)$$

where

$$\mathbf{I}_{\text{his}}(t) = \mathbf{YV}(t - \Delta t) + \left[\frac{1 - j\omega_c \Delta t/2}{1 + j\omega_c \Delta t/2} \right] \mathbf{I}(t - \Delta t) \quad (2-25)$$

$$\mathbf{Y} = \left[\frac{\Delta t/2L}{1 + j\omega_c \Delta t/2} \right].$$

$\mathbf{I}_{\text{his}}(t)$ is called the history current term as it is only dependent on the past time-step values of the current and voltage. $\mathbf{Y}(t)$ is the discretized form of the equivalent admittance of the inductor.

Similarly, the differential equation for a capacitor can be discretized and obtained as follows.

$$\mathbf{I}(t) = \mathbf{YV}(t) + \mathbf{I}_{\text{his}}(t) \quad (2-26)$$

where

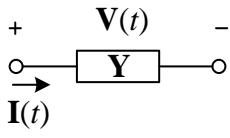
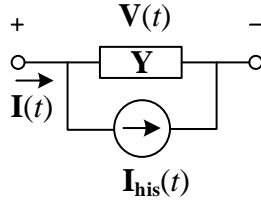
2.6 Modeling of Electrical Networks

$$\mathbf{I}_{\text{his}}(t) = -\mathbf{Y}^* \mathbf{V}(t - \Delta t) - \mathbf{I}(t - \Delta t) \quad (2-27)$$

$$\mathbf{Y} = 2C/\Delta t + j\omega_c C$$

Table 2-1 shows basic circuits elements along with their equivalent companion representations in dynamic phasor domain.

Table 2-1 Dynamic phasor and discretized equivalent companion models of basic circuit elements

| Resistor: | Inductor: | Capacitor: |
|---|--|--|
| Elements in time domain | | |
| $v(t) = Ri(t)$ | $\frac{di(t)}{dt} = \frac{1}{L}v(t)$ | $\frac{dv(t)}{dt} = \frac{1}{C}i(t)$ |
| Elements in dynamic phasor domain | | |
| $\mathbf{V}(t) = R\mathbf{I}(t)$ | $\frac{d}{dt}\mathbf{I}(t) = \frac{1}{L}\mathbf{V}(t) - j\omega_c\mathbf{I}(t)$ | $\frac{d}{dt}\mathbf{V}(t) = \frac{1}{C}\mathbf{I}(t) - j\omega_c\mathbf{V}(t)$ |
| Elements in dynamic phasor domain discretised using trapezoidal integration method (time-step = Δt) | | |
|  |  | |
| $\mathbf{Y} = \frac{1}{R}$ | $\mathbf{Y} = \frac{\Delta t/2L}{1 + j\omega_c \Delta t/2}$ $\mathbf{I}(t) = \mathbf{Y}\mathbf{V}(t) + \mathbf{I}_{\text{his}}(t)$ $\mathbf{I}_{\text{his}}(t) = \mathbf{Y}\mathbf{V}(t - \Delta t) + \left[\frac{1 - j\omega_c \Delta t/2}{1 + j\omega_c \Delta t/2} \right] \mathbf{I}(t - \Delta t)$ | $\mathbf{Y} = 2C/\Delta t + j\omega_c C$ $\mathbf{I}(t) = \mathbf{Y}\mathbf{V}(t) + \mathbf{I}_{\text{his}}(t)$ $\mathbf{I}_{\text{his}}(t) = -\mathbf{Y}^* \mathbf{V}(t - \Delta t) - \mathbf{I}(t - \Delta t)$ |

2.7 DP and EMT Comparison

2.6.2 Nodal Analysis

The numerical integration substitution technique discussed in Section 2.6.1 transfers all of the network equations into algebraic forms that have nodal voltages, branch currents, and their history terms as time-varying quantities. In order to obtain the solution of this system of equations, Dommel's method of nodal analysis can be employed. In this approach, nodal equations of the system are represented in the following matrix form.

$$[\mathbf{Y}][\mathbf{V}(t)] = [\mathbf{I}(t)] + [\mathbf{I}_{\text{his}}(t)] \quad (2-28)$$

where

$[\mathbf{Y}]$ is the nodal equivalent admittance matrix

$[\mathbf{V}(t)]$ is the nodal voltage vector

$[\mathbf{I}(t)]$ is the nodal current injection (by external devices) vector

$[\mathbf{I}_{\text{his}}(t)]$ is the nodal history current vector

In order to compute $[\mathbf{V}(t)]$ using (2-28), the LU decomposition method is widely used. This method exploits the sparse nature of the $[\mathbf{Y}]$ matrix storing only the nonzero elements of the triangularized matrix.

2.7 DP and EMT Comparison

A simple test system to illustrate both the EMT and DP-based simulations is shown in Figure 2-2. In this balanced three-phase system, two voltage sources are connected at the ends of a segmented 230-kV, 60-Hz transmission line. Per-unit impedances of each line segment, modelled as a π -section, are tabulated in Table 2-2. Initial conditions of the

2.7 DP and EMT Comparison

sources are selected to transfer 315 MW from ac system 1 to ac system 2. A line-to-ground fault is applied at bus B_4 at $t = 1.0$ s and cleared at $t = 1.12$ s. The fault impedance is modelled as a variable resistor with off and on values of $1 \text{ M}\Omega$ and $0.01 \text{ }\Omega$, respectively. Simulations are conducted once with an EMT simulator and once with a DP simulator with a carrier frequency of 60 Hz. For the DP-based solution, the procedure of conversion to the dynamic phasor domain and discretization using trapezoidal method described in Section 2.6 is employed.

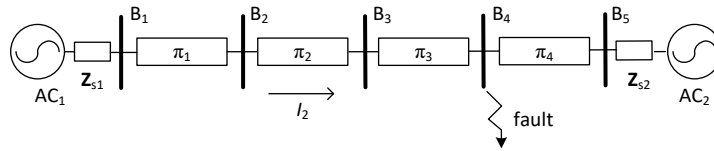


Figure 2-2 Simple test system

Table 2-2 Per-unit impedance of line segments (base values: 230 kV/100 MVA)

| Segment | R [pu] | X [pu] | B [pu] |
|-----------------------|----------|----------|----------|
| π_1 | 0.00115 | 0.00911 | 1.83e-02 |
| π_2 | 0.00336 | 0.03306 | 5.55e-02 |
| π_3 and π_4 | 0.00168 | 0.01333 | 2.77e-02 |
| Z_{S1} and Z_{S2} | - | 0.00071 | - |

A simulation time-step of $20\text{-}\mu\text{s}$ was used in both simulators and the results are shown in Figure 2-3. Equation (2-1) was used to convert the phasor quantities in DP simulator into instantaneous waveforms.

2.7 DP and EMT Comparison

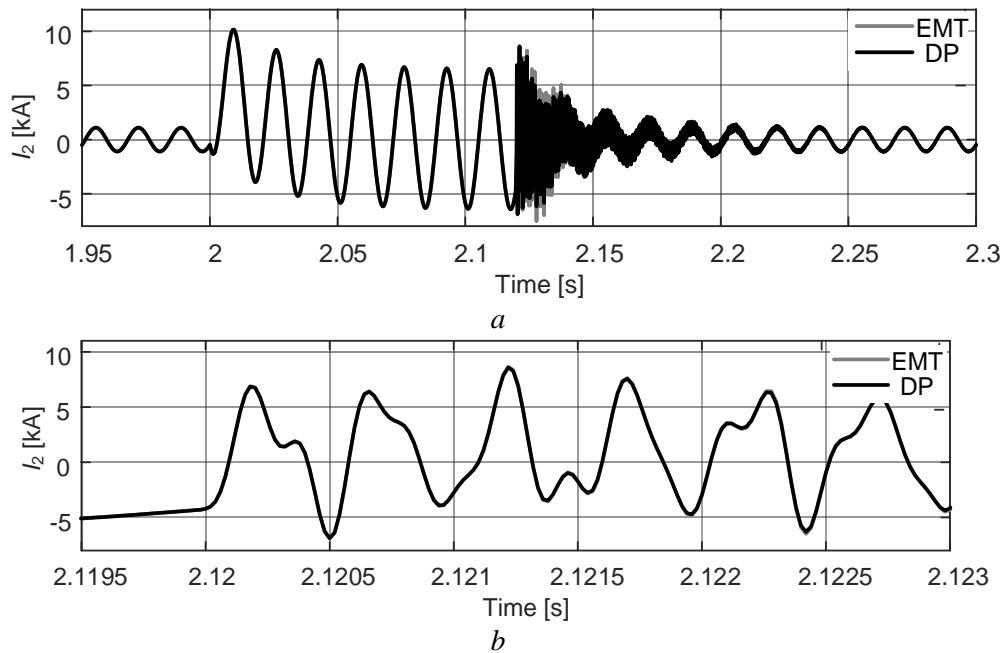


Figure 2-3 Current through line-segment π_2 of the network in Figure 2-2 using two separate simulators: an EMT simulator and a DP simulator

a. Full system response

b. Zoomed-in view of fault-clearance transient

The traces in Figure 2-3 show complete conformity between the EMT and DP simulators, both for the pre-and post-fault steady state operation, and during the fast transients caused by the clearing of the fault. This exemplifies the validity of dynamic phasor-based solution to study fast network transients as described in [31].

Chapter 3

Interfacing DP and EMT Simulators

3.1 Introduction

Co-simulation techniques couple two or more constituent simulators. Multi-physics co-simulations are used to study interactions between multiple physical models or multiple simultaneous physical phenomena such as in electrothermal analysis. TS-EMT simulations are not multi-physics simulations but rather multi-model coupling of two simulators for the study of the same phenomena [22]. As explained in Section 1.1, different power system simulation tools use different modeling approaches and assumptions to model power system dynamics. TS-EMT co-simulation is also referred to as a *hybrid simulation* since the two simulators use different modeling approaches. The numerical stability and accuracy of such a hybrid simulator strongly depends on the coupling technique used for co-simulation. Therefore, it is challenging to maintain both accuracy and numerical stability of a hybrid simulator. This chapter describes the mathematical foundations of the DP-EMT interface and demonstrates them using an illustrative example.

3.2 Subsystem Definition

Hybrid simulation models consist of two or more subsystems. Subsystems in hybrid power system models are usually categorised as *detailed* and *external* [3], [45]. More than one detailed or external subsystem in a hybrid system model is possible [3], [22]. In this thesis, each detailed subsystem is modeled in the EMT platform, which typically includes a power electronic device that demands small time-steps. In order to improve the accuracy, the detailed system can be extended to include parts of the network around the concerned power electronic device [45]. Further, this thesis uses the DP approach to model the external system.

Once the detailed system is defined, partitioning (or segmentation) is done at user-selected locations. These locations are typically called boundary busses or interface busses, in which external and detailed systems are interfaced.

3.3 Coupling Techniques

This thesis first investigates the coupling techniques discussed in the literature on TS-EMT co-simulation. In TS-EMT co-simulation, two simulators are run at different time-steps. For instance, the EMT side runs at a smaller time-step (denoted as Δt) while the TS side runs at larger time-step (denoted as ΔT). If the larger time-step is selected as an integer multiple of the smaller time-step, both systems are solved together every integer multiple of ΔT . During the intermediate time steps (i.e., $t+\Delta t$, $t+2\Delta t$, ...), only the EMT side is

3.3 Coupling Techniques

solved. Figure 3-1 shows the time axis of a TS-EMT hybrid simulation with a 1: n time-step ratio.

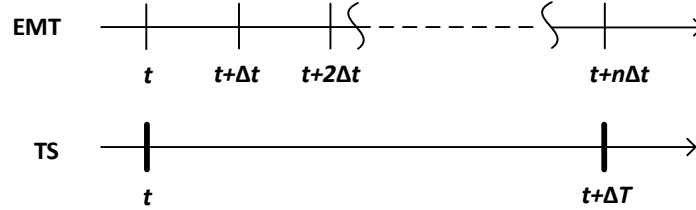


Figure 3-1 Time axis of a TS-EMT hybrid simulation

Equivalent networks are used to define the boundary conditions at the interfacing busses and the validity of the hybrid simulator directly depends on the accuracy of the equivalent model [3]. For instance, the TS network can be represented as a fundamental frequency Norton equivalent connected to the interface bus at the EMT side to obtain the solution of the EMT network and vice versa [46]. A more accurate equivalent is proposed in [45] using Frequency Dependent Network Equivalent (FDNE) where the accuracy of the equivalent is extended over a wider range of frequencies.

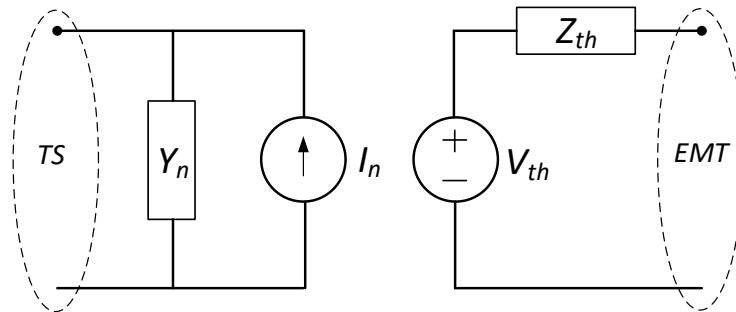


Figure 3-2 TS-EMT boundary condition

Figure 3-2 shows a boundary condition applied in a TS-EMT interface discussed in [22], [47]. In this approach, the external (TS) system is represented by a Thévenin equivalent at the boundary of the detailed (EMT) system. Similarly, a Norton equivalent of the detailed

3.4 Partitioning at Transmission Lines

system is used at boundaries of the external system. A systematic way of calculation this equivalent source values is presented in [22], [47].

The solution of the hybrid system is obtained using ‘explicit’ or ‘implicit’ coupling approaches. In explicit coupling, two simulators run independently, exchanging data at regular intervals [48]. Often, extrapolation is used to predict the quantities of the Thévenin equivalent at intermediate time steps. However, no iteration is done between the TS and EMT solutions to correct the predicted values [2]. In contrast, an implicit coupling approach uses an iterative approach (e.g., Newton’s method) to solve the TS and EMT equations simultaneously.

Explicit coupling between the DP and EMT side is preferable as no iterative solution between the DP and EMT side is needed. Further, this approach will allow interfacing of a DP simulator with an existing EMT simulator without changing the internal architecture of either simulator. However, to achieve this, the nodal equations of the DP and EMT sides need to be decoupled.

3.4 Partitioning at Transmission Lines

Transmission lines or cables introduce a delay to the transient at one end when it appears at the other end [49]. EMT simulators often use Bergeron’s line model [33] to represent transmission lines and cables. As a travelling wave model, it introduces natural decoupling in the nodal equations of EMT simulators [1]. The latency of a transmission line implies that samples of voltage and current at one end of the line will be available at the other end

3.4 Partitioning at Transmission Lines

only after a certain delay, which is determined by the line length. Therefore if system partitioning is done at transmission lines, coupling between the subsystems' nodal equations (i.e., detailed and external) only happens through history current terms, which can be calculated from the past values. Commercial EMT simulators exploit the subsystem concept to improve program efficiency during switching events [49] by confining the conductance matrix re-triangularization process within the subsystem. Also this decoupled subsystem concept allows parallel processing techniques in multiprocessor environments [1].

Figure 3-3 shows the equivalent impedance model [44] of a lossless line between nodes m and k of an arbitrary network.

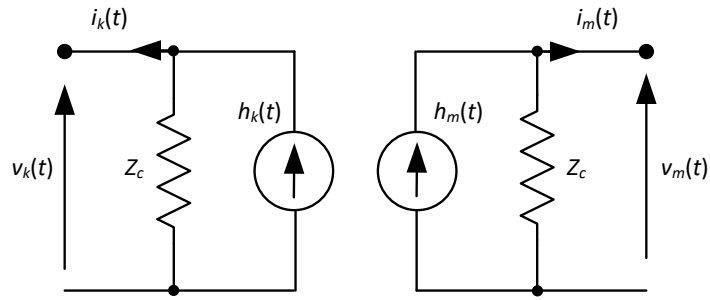


Figure 3-3 Equivalent impedance model of lossless line

Kirchhoff's current law at nodes k and m yields:

$$i_m(t) = h_m(t) - \frac{v_m(t)}{Z_c} \quad (3-1)$$

$$i_k(t) = h_k(t) - \frac{v_k(t)}{Z_c} \quad (3-2)$$

where the history currents can be calculated by previous voltage and currents at the opposite side as follows.

3.4 Partitioning at Transmission Lines

$$h_m(t) = \frac{v_k(t-\tau)}{Z_c} - i_k(t-\tau) \quad (3-3)$$

$$h_k(t) = \frac{v_m(t-\tau)}{Z_c} - i_m(t-\tau) \quad (3-4)$$

In (3-3) and (3-4), τ represents the travel-time of the traveling wave from one end of the line to the other. Substituting $i_m(t-\tau)$ and $i_k(t-\tau)$ from (3-1) and (3-2) gives:

$$h_k(t) = \frac{2v_m(t-\tau)}{Z_c} - h_m(t-\tau) \quad (3-5)$$

$$h_m(t) = \frac{2v_k(t-\tau)}{Z_c} - h_k(t-\tau) \quad (3-6)$$

Dynamic phasor form of the (3-5) and (3-6) are written as follows.

$$\mathbf{H}_k(t) = \left(\frac{2\mathbf{V}_m(t-\tau)}{Z_c} - \mathbf{H}_m(t-\tau) \right) e^{-j\tau\omega_c} \quad (3-7)$$

$$\mathbf{H}_m(t) = \left(\frac{2\mathbf{V}_k(t-\tau)}{Z_c} - \mathbf{H}_k(t-\tau) \right) e^{-j\tau\omega_c} \quad (3-8)$$

In the simulation examples of this section a special case of (3-5) and (3-6) is considered where τ is equal to the simulation time-step size Δt . This corresponds to a transmission line whose latency is one simulation time-step, and for which (3-5) and (3-6) will simplify to:

$$h_k(t) = \frac{2v_m(t-\Delta t)}{Z_c} - h_m(t-\Delta t) \quad (3-9)$$

$$h_m(t) = \frac{2v_k(t-\Delta t)}{Z_c} - h_k(t-\Delta t) \quad (3-10)$$

where

$$Z_c = \sqrt{L/C} \text{ and } LC = (\Delta t)^2. \quad (3-11)$$

3.4 Partitioning at Transmission Lines

If a fictitious transmission line is to be used for segmentation, its L and C components need to be selected so that a one time-step travel-time is achieved. Normally, this is done by borrowing inductance from neighbouring elements and adjusting the C value in (3-11) according to the simulation time-step. An example of such segmentation is shown in Figure 3-4 where the simple network shown in Figure 2-2 is segmented at bus 3. In this example, the inductance value (L) is chosen as 0.01 H considering the impedences of π_2 and π_3 . Then the capacitance value (C) is calculated as 0.04 μF for a simulation time-step of 20 μs . To have minimum impact on the original system, these L and C values are deducted from the two neighbouring π -sections. The modified line sections are denoted as $\pi_{2\text{-new}}$ and $\pi_{3\text{-new}}$. Using (3-11), Z_c is determined to be 500 Ω .

Simulation studies of the decoupled network in Figure 3-4 are shown in Figure 3-5 (a) and (b). The decoupled system was simulated, once in the EMT simulator and then in the DP simulator. For comparison, the EMT traces of the non-decoupled system are also plotted in the same graph. The traces confirm that the given artificial decoupling has negligible impact on the accuracy of low-frequency transients. However, difference can be observed in high frequency transients between the non-decoupled and the decoupled networks. Further, these results confirm that artificial decoupling can preserve the accuracy of the low frequency transients if the L and C elements are carefully selected.

3.4 Partitioning at Transmission Lines

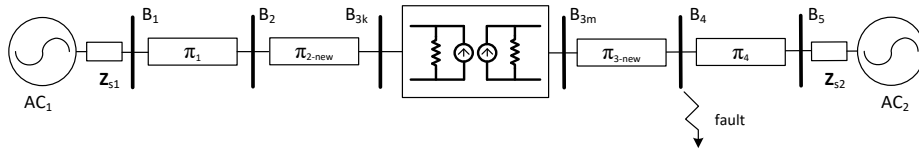


Figure 3-4 Decoupled simple test system

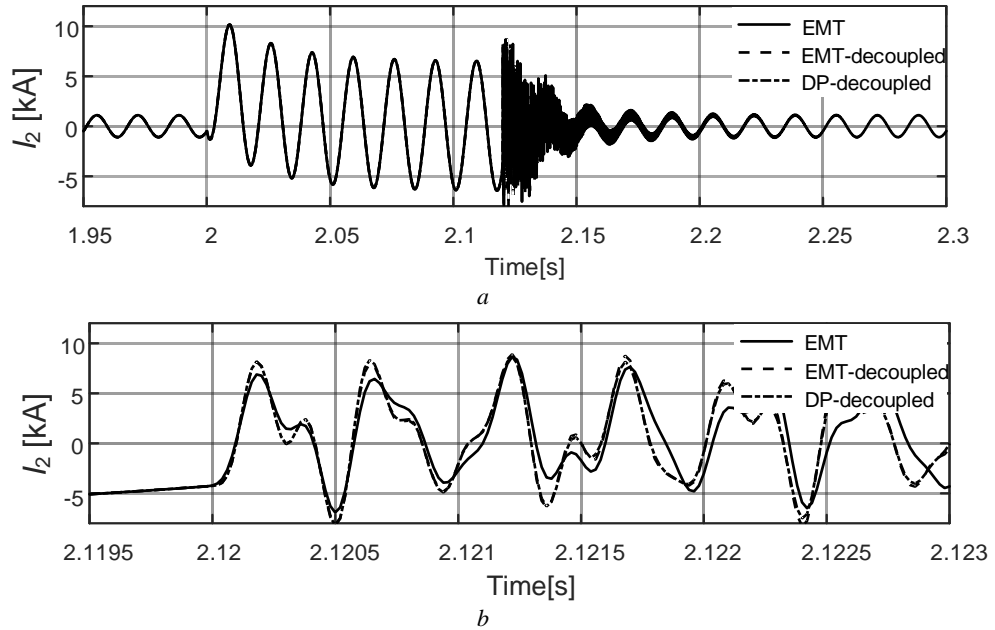


Figure 3-5 Current through line-segment π_2 of the network in Figure 2-2 (using an EMT simulator) and Figure 3-4 (using two separate simulators: an EMT simulator and a DP simulator)

a. Full system response

b. Zoomed-in view of fault-clearance transient

Note that the one time-step delay using an artificial lossless line model described above is only a means for segmentation of a network at an arbitrary location where a physical transmission line may not exist; otherwise, this method is applicable to physical transmission lines of arbitrary length as well.

3.5 DP-EMT Interface

Interfacing via transmission lines (physical or artificial) becomes challenging when the subsystems on the two sides of the interface are simulated and solved using different simulation methods. The equivalent impedance model of the DP-EMT interface is similar to the one shown in Figure 3-3 in which $\mathbf{V}_k(t)$, $\mathbf{I}_k(t)$ and $\mathbf{H}_k(t)$ replace the corresponding quantities on the node k side of the interface assuming that nodes k and m represent the dynamic phasor and EMT sides of the interface, respectively.

Using (2-2), dynamic phasor quantities (i.e., $\mathbf{V}_k(t-\tau)$ and $\mathbf{H}_k(t-\tau)$) are readily converted to instantaneous quantities and then (3-6) can be employed to determine the current injection (i.e., $h_m(t)$) at node m .

In order to determine the history current at node k , equation (3-7) is used. The instantaneous quantities at the EMT side (i.e., $v_m(t-\tau)$ and $h_m(t-\tau)$) have to be converted to DP quantities. However, conversion of an instantaneous quantity in EMT side to a dynamic phasor equivalent is not straightforward. In essence, this requires conversion of a signal from the EMT simulator to an equivalent dynamic phasor to be used in the dynamic phasor side of the interface. Different ways to extract dynamic phasors from the instantaneous waveform are discussed next.

3.5.1 Instantaneous EMT to DP Conversion - Analytic Signal Approach

Determining the dynamic phasor equivalent of an arbitrary signal is an ill-posed problem, as there are infinite $a(t)$ and $\phi(t)$ pairs that will yield the given signal $x(t)$ (i.e., satisfy (2-2)). Even though all these pairs are mathematically legitimate, not all of them are physically sensible as they violate reasonable physical conditions. [50] has established four conditions in order to determine the extracted complex signal has a physical meaning.

In [26], the analytic signal approach was first introduced to unambiguously define the magnitude and phase of a real signal. Also [20], [21] and [33] use this analytic signal approach to define the complex signal $\underline{x}(t)$ given in (2-3). This method converts a real signal $x(t)$ into a complex signal or an analytic signal $\underline{x}(t)$ as follows:

$$\underline{x}(t) = x(t) + jH[x(t)] \quad (3-12)$$

where H denotes the Hilbert transformation defined as

$$H[x(t)] = \frac{1}{\pi} \int_{-\infty}^{\infty} \frac{x(\tau)}{t - \tau} d\tau. \quad (3-13)$$

However, [50] shows that the analytic signal magnitude may be unbounded (i.e., it can go to infinity) and also can produce signals with very high rate of change of phase. Also digital Hilbert transformation cannot be realised exactly and approximations are involved as shown in [51].

3.5.2 Instantaneous EMT to DP Conversion - Fourier Approach

Another method to extract a dynamic phasor is to follow the basic definition of Fourier decomposition on a sliding window as was explained in Section 2.4. In this approach, (2-13) is used to find the time-averaged complex Fourier coefficient of an arbitrary harmonic h . Then, employing (2-18) the corresponding dynamic phasor is calculated. However, in practical situations the infinite series given in (2-18) has to be truncated at a finite number.

3.5.3 Representing only by the Fundamental

Fast Fourier Transformation (FFT) using one-cycle moving window to extract the fundamental component of instantaneous signal is widely used in TS-EMT interfacing [2], [22]. In this case, the infinite series in (2-18) is truncated to retain only the fundamental component. Then $\mathbf{X}(t)$ can be expressed as follows:

$$\mathbf{X}(t) \approx 2\langle x \rangle_1(t) \quad (3-14)$$

Using (2-13), the fundamental complex Fourier coefficients of $v_m(t-\tau)$ and $h_m(t-\tau)$ can be extracted. Then, (2-18) and (3-7) gives

$$\mathbf{H}_k(t) \approx 2 \left(\frac{2\langle v_m \rangle_1(t-\tau)}{Z_c} - \langle h_m \rangle_1(t-\tau) \right) e^{-j\tau\omega_c}. \quad (3-15)$$

Figure 3-6 (a) shows a comparison of the results obtained for the simulation of the fault scenario in Section 2.7 for the decoupled network shown in Figure 3-4. The figure shows both the EMT and the DP-EMT traces when the system is segmented at bus B_3 . The portion of the system to the right of bus B_3 is modelled in EMT and the portion to the left of the

bus is modelled using dynamic phasors. Both subsystems are simulated with a time-step of 20 μs and transmission delay of the line is 20 μs .

Although the DP-EMT trace follows the EMT waveform during the pre-fault steady-state regime, it has poor performance during the transient caused by the fault (i.e., for $t > 2.0$ s and prior to re-settling into steady state). This is directly caused by (i) the averaging operation over one sliding cycle to calculate $\mathbf{H}_k(t)$, and (ii) the fact that only one frequency component (the fundamental) is used in the Fourier representation of EMT waveforms. Averaging acts as a low-pass filter and disallows proper transfer of transients during the fault from one end to another, thereby deteriorating simulation accuracy.

Marked improvement in the DP-EMT interface is obtained by explicitly expressing the history terms in the interface line model in Figure 3-3. To do so (3-7) is rearranged by substituting from (3-8) as follows.

$$\mathbf{H}_k(t) = \left(\frac{2\mathbf{V}_m(t-\Delta t)}{Z_c} - \left(\frac{2\mathbf{V}_k(t-\tau-\Delta t)}{Z_c} - \mathbf{H}_k(t-\tau-\Delta t) \right) e^{-j\omega_c\tau} \right) e^{-j\omega_c t} \quad (3-16)$$

Here, the dynamic phasor quantities $\mathbf{V}_k(t-\tau-\Delta t)$ and $\mathbf{H}_k(t-\tau-\Delta t)$ are already known from previous time-steps of the simulation. The unknown dynamic phasor quantity $\mathbf{V}_m(t-\tau)$ can be calculated using the approximation in (3-14). Traces of the Figure 3-6 (b) show that this approach produces an improved response during the fault. However, high frequency transients following fault clearing are heavily damped out.

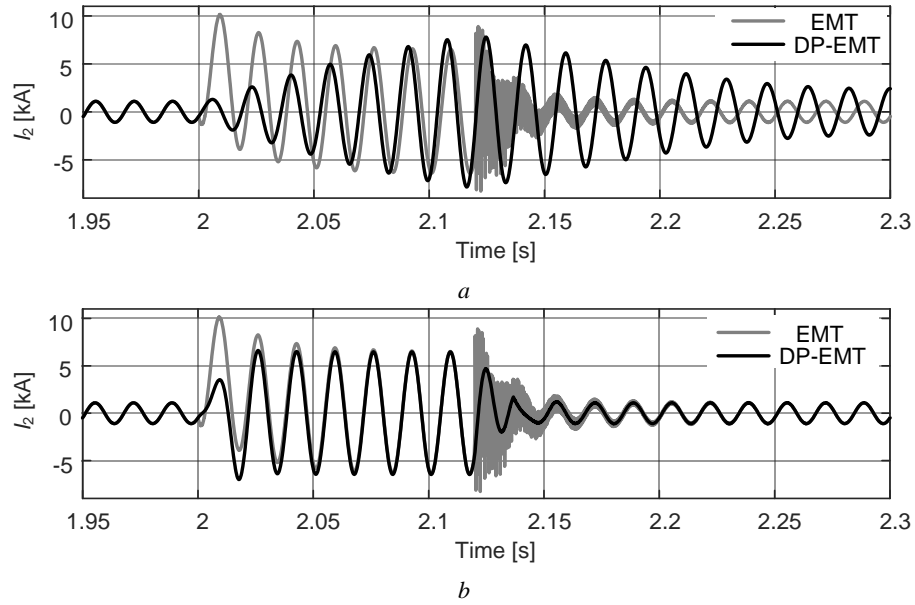


Figure 3-6 Current through line-segment π_2 of the network in Figure 3-4

a. DP-EMT interface with fundamental component

b. DP-EMT interface with fundamental component and eliminated current samples

3.5.4 Improvement by Including the DC Offset

In previous sections dynamic phasors were approximated by their fundamental Fourier coefficients. Dynamic phasors become more accurate by considering other components of the Fourier spectrum. Under normal operating conditions, ac quantities will have no dc component. However, during a fault or other transients, temporary dc offsets may be present. Therefore, including the dc component may offer noticeable accuracy improvements. As such in this section the dc component of the voltage waveform $v_m(t - \Delta t)$ is calculated using (2-13) with $h = 0$, and included in the calculation of the dynamic phasor quantity. In this case the infinite series in (2-18) is truncated to keep the dc and fundamental component as follows:

$$\mathbf{X}(t) \approx \langle x \rangle_0(t) e^{-j\omega_c t} + 2\langle x \rangle_1(t) \quad (3-17)$$

It must, however, be noted that dynamic phasor simulation is done for the base frequency ω_c ; therefore, the calculated dc component is represented as a dynamic phasor at the fundamental frequency of ω_c rather than at zero frequency. In (3-17), multiplying the dc components by $e^{-j\omega_c t}$ shifts the dc component to the frame of the fundamental component. In other words, the dc component of the waveform appears as a fundamental-frequency component with varying amplitude and phase.

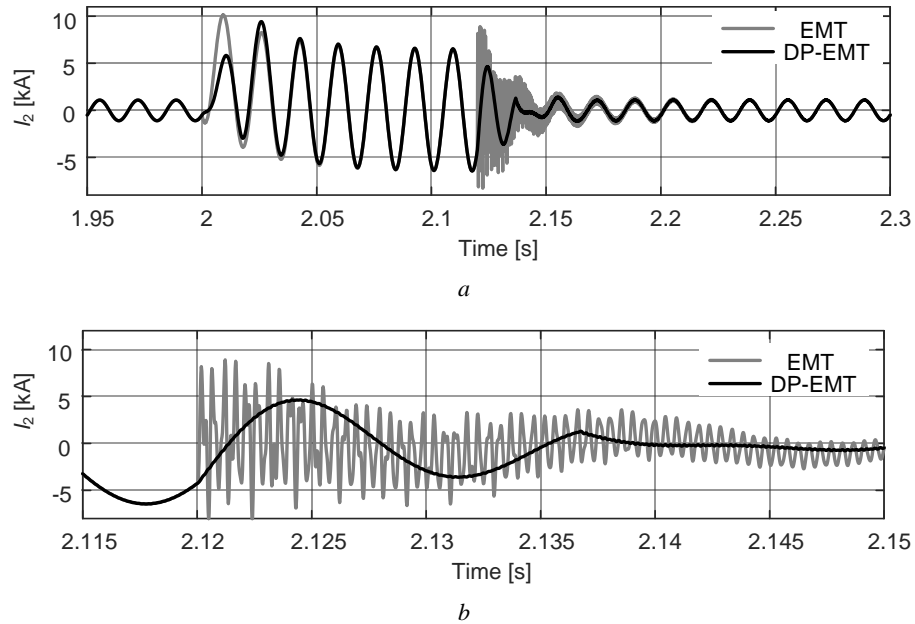


Figure 3-7 Current through line-segment π_2 of the network in Figure 3-4

a. DP-EMT interface with dc augmentation

b. Zoomed-in view of the transient after fault clearance

Simulation results of the segmented network using dc-augmented dynamic phasors are shown in Figure 3-7(a) and (b), and show much closer conformity to the EMT traces resulting from the dc component. However, the DP-EMT results still do not follow the fast transients after fault clearance. This is due to the averaging of the EMT signal in (2-13).

3.6 A Novel DP Extraction Technique

One may expect that the accuracy of the simulation results of the DP-EMT interface must improve further if a large number of terms in (2-18) are considered to calculate the dynamic phasors. Similar accuracy improvement is partially observed in Section 3.5.4 where the fundamental component of the EMT signal to be transferred is augmented with its dc components. This approach, however, is computationally demanding and will hinder the speed gain that one would expect from DP-EMT co-simulation. The highest Fourier component depends on the time-step of the simulation based on the Nyquist frequency. Despite this seemingly reasonable expectation, Appendix A shows that the dynamic phasor equivalent of a time-varying real signal cannot be computed with acceptable accuracy even if large numbers of Fourier terms are used if the real signal has abrupt changes.

Alternatively, this thesis proposes an approach that extracts the entire harmonic contents of an EMT waveform (essentially all harmonics embedded in the EMT waveform) and shifts them altogether to the fundamental-component frame. Consider an arbitrary waveform $x(t)$ and its Fourier expansion over the window $(t-T, t]$. The waveform can be expressed in terms of its fundamental and harmonic contents as follows.

$$x((t-T+s)) = A_1 \cos(\omega_c(t-T+s) + \phi_1) + \sum_{\substack{h=-\infty \\ h \neq 1, -1}}^{\infty} \langle x \rangle_h(t) e^{jh\omega_c(t-T+s)} \quad (3-18)$$

where, and A_1 and ϕ_1 are the magnitude and phase angle of the fundamental component, respectively. The summation term in (3-18) represents all harmonic contents of the

3.6 A Novel DP Extraction Technique

waveform (including dc). Note that the actual signal $x(t)$ is readily available through the EMT simulator and its fundamental component is calculated using (2-13) with $h = 1$. (3-18) can be re-arranged to explicitly show all harmonic contents of the signal in the fundamental-component frame as follows.

$$x((t - T + s)) = A_1 \cos(\omega_c(t - T + s) + \phi_1) + \underbrace{\left(\sum_{\substack{h=-\infty \\ h \neq 1, -1}}^{\infty} \langle x \rangle_h(t) e^{j(h-1)\omega_c(t-T+s)} \right)}_{X_r(t)} e^{j\omega_c(t-T+s)} \quad (3-19)$$

The term $\mathbf{X}_r(t)$ includes all harmonic components of the signal $x(t)$ and shows them in the frame of its fundamental component. With both $x(t)$ and its fundamental component at hand, $\mathbf{X}_r(t)$ is easily calculated as follows.

$$\mathbf{X}_r(t) = (x(t) - A_1 \cos(\omega_c t + \phi_1)) e^{-j\omega_c t} \quad (3-20)$$

Once $\mathbf{X}_r(t)$ is obtained using (3-20), it is augmented to the already available fundamental component. During transients, this causes such modulation of the amplitude and phase angle of the fundamental component that will exactly replicate the original waveform $x(t)$. The process of calculating this fully augmented fundamental is shown in Figure 3-8.

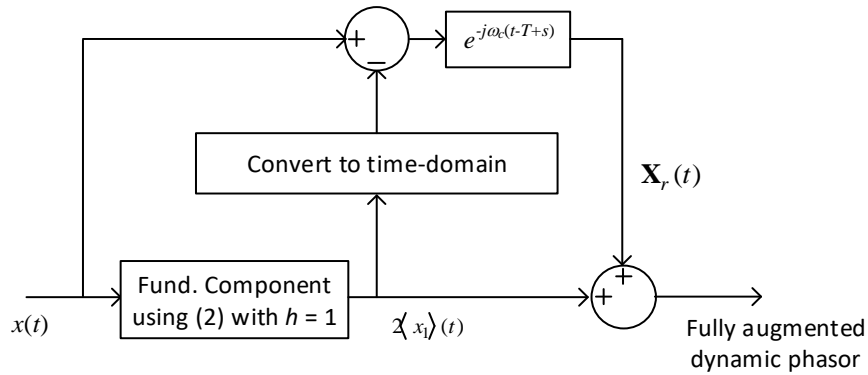


Figure 3-8 Full augmentation of the fundamental dynamic phasor

3.6.1 Testing of the Proposed DP Extraction Technique

The test setup shown in Figure 3-9 is used to demonstrate that the proposed method can calculate the dynamic phasor of a given input signal. First, the dynamic phasor $\mathbf{U}(t)$ of the input signal $u(t)$ is calculated using the proposed technique. Secondly using (2-2), the corresponding real signal $u'(t)$ of the input $\mathbf{U}(t)$ is calculated. In this exercise, four different signals are tested as listed below:

1. A signal with magnitude jump by 80%
2. A signal with phase jump by π
3. A signal with DC offset
4. A signal with 2% , 5th harmonic content

Figure 3-10 and Figure 3-11 show a comparison between input and output signals of the test system. They also show the magnitude and phase signals corresponding to the dynamic phasor signal $\mathbf{U}(t)$. These plots shows that the input and output signals are perfectly matching (up to 6th decimal place) and hence confirm accuracy of the proposed technique.

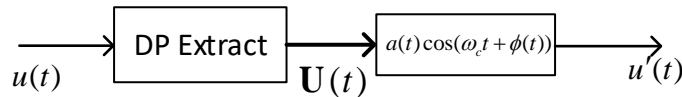


Figure 3-9 Test system for the proposed dynamic phasor extraction technique

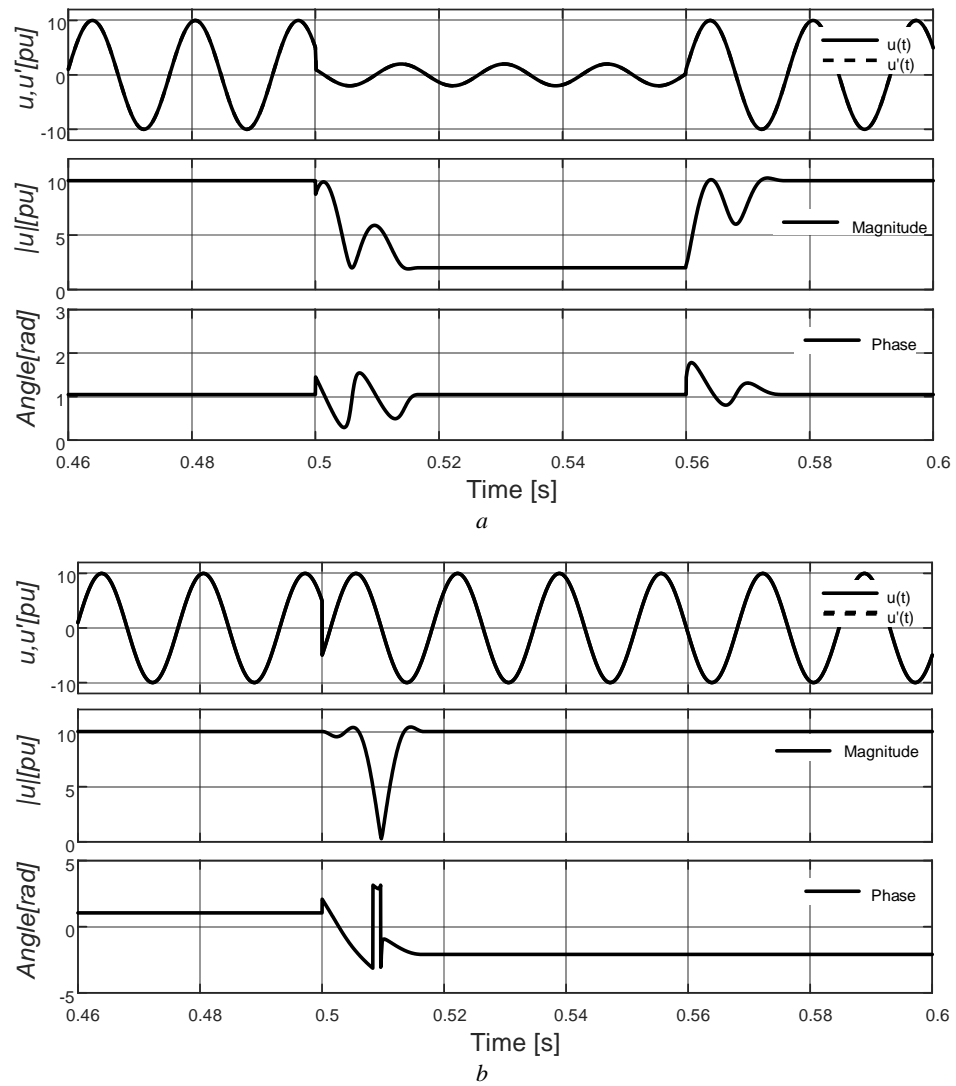


Figure 3-10 Test for magnitude jump and phase jump

a. Test for magnitude jump by 80%

b. Test for phase jump by π

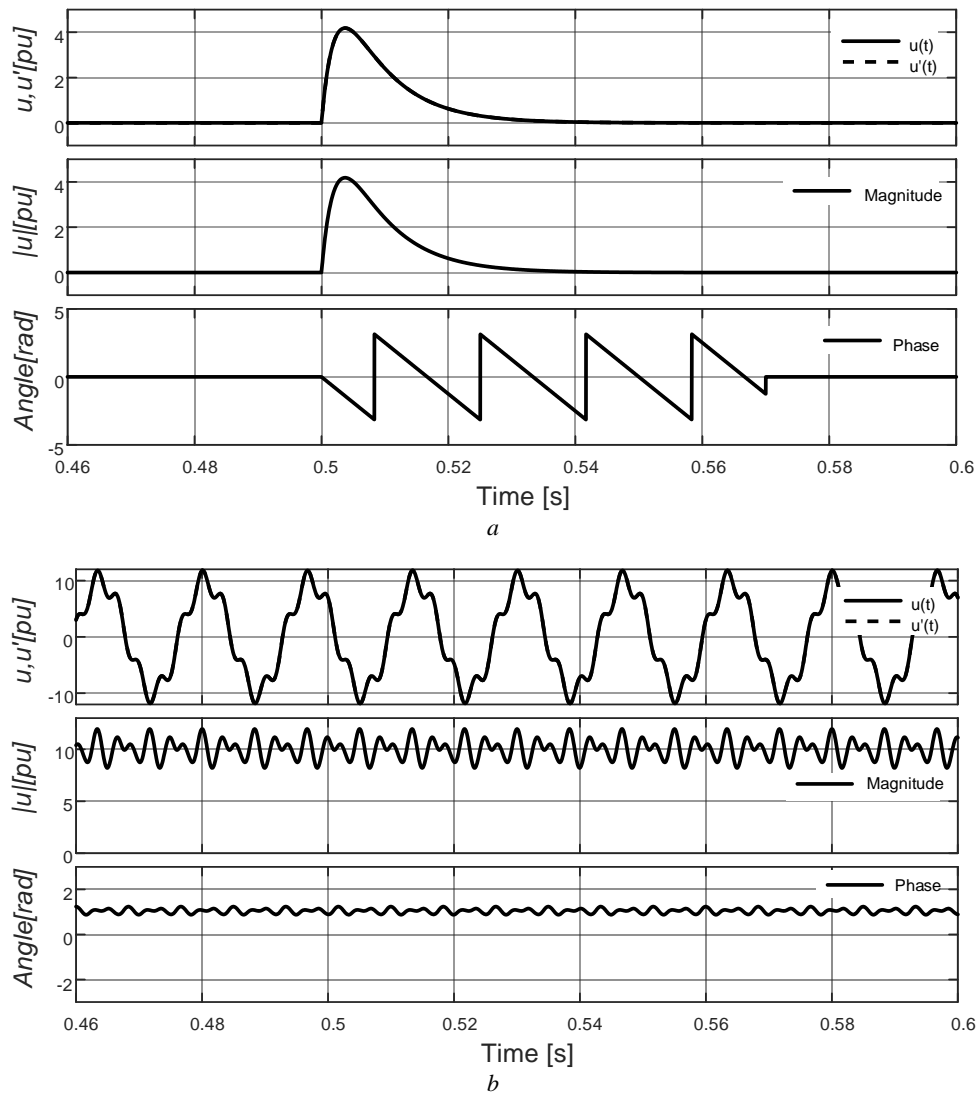


Figure 3-11 Test for DC offset and harmonic

a. Test for a DC offset

b. Test for 2%, 5th harmonic content

3.6.2 Simulation Example

The simulation results of the sample network in Figure 3-4 using the DP-EMT interface with the fully-augmented fundamental are shown in Figure 3-12(a) and (b). The traces show complete conformity during all stages of the response, including the high-frequency oscillations following fault clearance as depicted in Figure 3-12(b). This confirms that accurate DP-EMT interface is realizable with the proposed DP extraction technique.

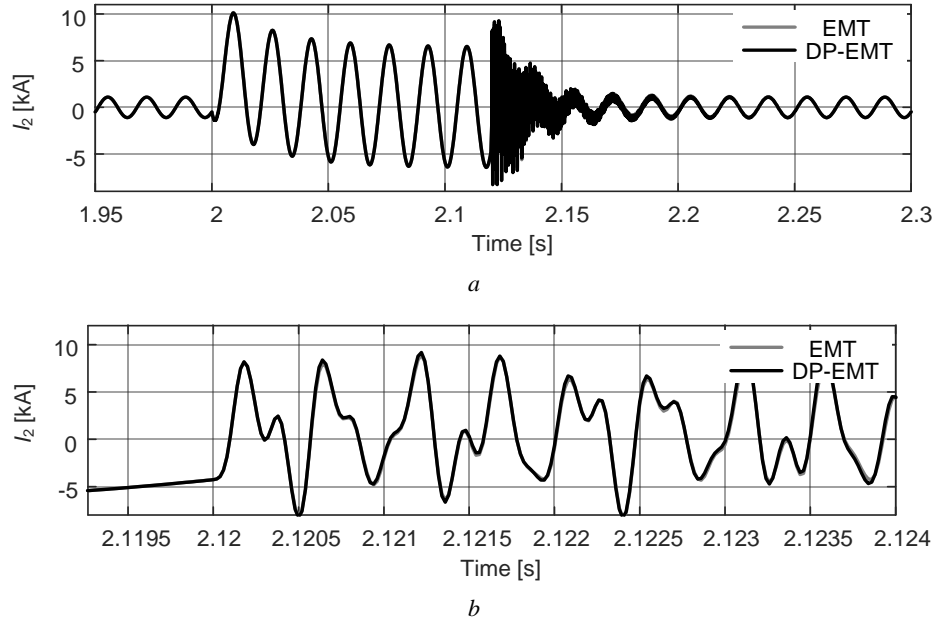


Figure 3-12 Current through line-segment π_2 of the network in Figure 3-4

- a. DP-EMT interface with full harmonic augmentation
- b. Zoomed-in view of the transient after fault clearance

3.6.3 Introducing Damping

The proposed DP extraction technique offers flexibility to introduce damping to the DP extraction process. Figure 3-13 shows a damping factor α introduced to the $\mathbf{X}_r(t)$ component. In this way, damping can be selectively introduced to the non-fundamental component of the transient.

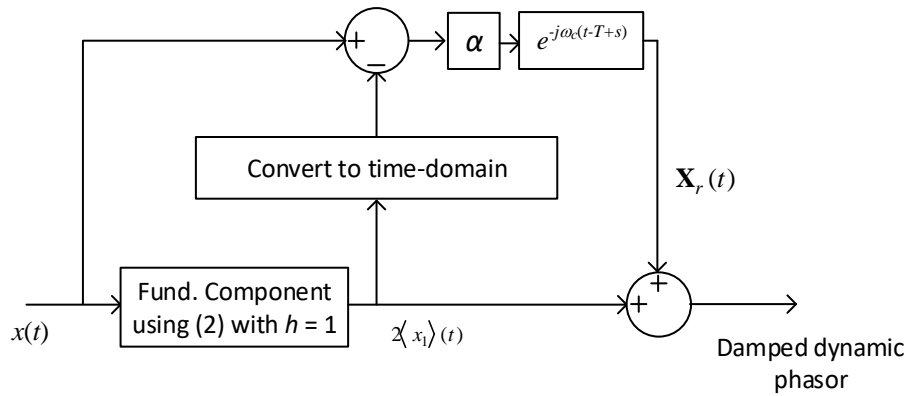


Figure 3-13 DP extraction with damping

Throughout the course of this research it was observed that damping is not required if the DP-EMT co-simulation runs at one-to-one time-step ratio. For instance, the simulation example presented in Section 3.6.2 uses no damping (i.e., $\alpha = 1$). This can be explained as the one-to-one time-step ratio does not introduce inaccuracies to the numerical solution of the two sides of the interface as the novel DP extraction process can capture all frequency components in the transient present at the EMT side.

On the other hand, the multi-rate co-simulation approaches discussing in this thesis (in Chapter 4 and 5) use interpolation to determine intermediate points, as such the data-point granularity between the two sides of the interface is different. Therefore, the multi-rate

simulation naturally introduces additional inaccuracies to the solution, which could lead to numerical instability of simulations. For instance, the EMT side running at a smaller time-step can capture high frequency transients that may not be able to handle at the DP side that runs at a larger time-step. These high frequency transients have to be absorbed by some means such as additional filters at the EMT side of the interface.

Another method to handle this imbalance is to use damping factor shown in Figure 3-13, which provide a flexible way to introduce damping. Therefore, all multi-rate DP-EMT simulation examples presented in Chapter 4 and 5 use 1.0% damping (i.e., $\alpha = 0.99$). This value is selected empirically.

3.6.4 TS-EMT Interfacing

The thesis mainly focuses on a DP-EMT interface. The applicability of the novel DP extraction technique in TS-EMT co-simulation is lightly investigated. The simple network in Figure 3-4 is tested for TS-EMT co-simulation where the k and m sides of the system represent the TS and EMT sides, respectively. TS modeling approach depends on quasi-steady-state conditions, which assume the changes in network voltage and currents are fast compared to the dynamics of rotating machines [2]. Based on this assumption, the network elements are represented by conventional steady-state phasors and dynamic devices are represented by time-varying current sources. As a result of this, when EMT and TS simulators are interfaced there will be a large mismatch between two solutions due to these differences in modeling between two simulators. Hence, the TS-EMT interface has to absorb high-frequency components of the EMT signals to maintain the numerical stability

3.6 A Novel DP Extraction Technique

of the simulation. Investigations revealed that the damping factor discussed in the previous section can be used to achieve numerical stability of the TS-EMT interface. The simulation results of the sample network in Figure 3-4 using the TS-EMT interface with different damping factors are shown in Figure 3-14(a)-(c).

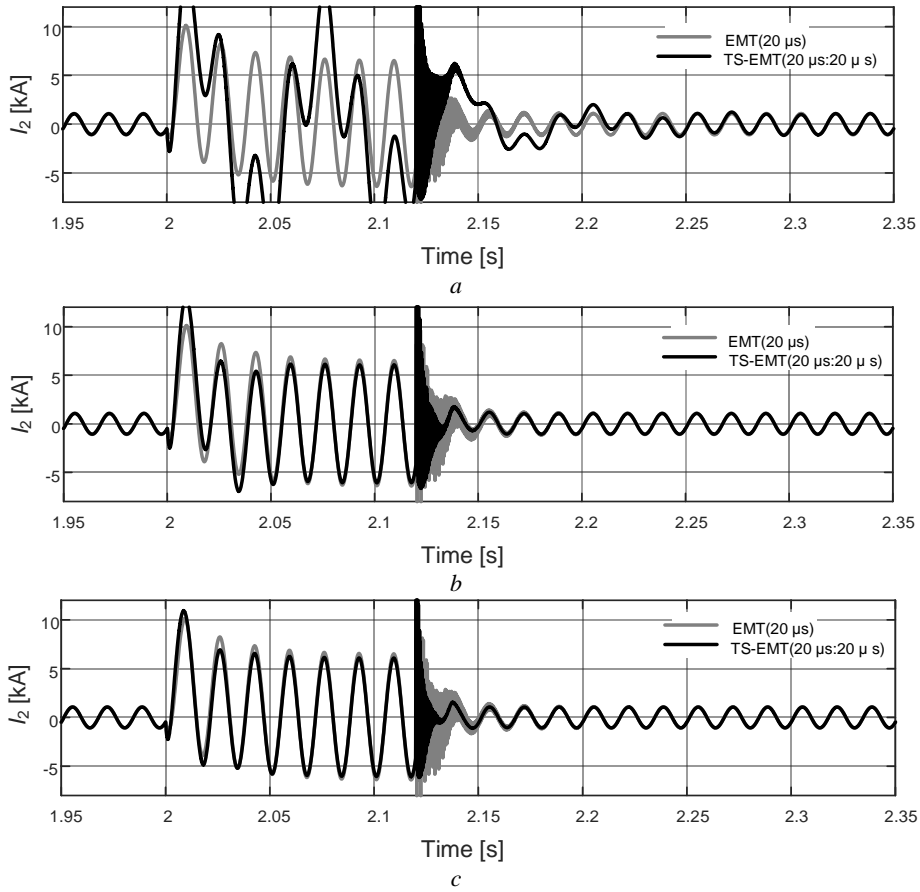


Figure 3-14 Current through line-segment π_2 in TS-EMT co-simulation

a. TS-EMT interface with $\alpha = 0.97$

b. TS-EMT interface with $\alpha = 0.95$

c. TS-EMT interface with $\alpha = 0.93$

3.7 Chapter Summary and Contribution

The chapter described how simulated samples are converted from the EMT domain to counterpart dynamic phasors and vice versa, and transmitted across the transmission line interface. In particular, a novel, computationally efficient method was presented for conversion of EMT samples to dynamic phasors, which retained the full harmonic spectrum of the EMT waveform and represented it as a dynamic phasor at fundamental frequency. The proposed DP extraction technique offers flexibility to introduce controlled numerical damping. Further, it was demonstrated that the presented DP-EMT co-simulation strategy with full harmonic augmentation is able to exactly replicate EMT simulation results when a sufficiently small simulation time-step is used in both constituent simulators.

Chapter 4

Multi-Rate DP-EMT Co-Simulation

4.1 Introduction

The simulation studies shown in the previous chapters were conducted with the same time-step for both the EMT and dynamic phasor simulators. Dynamic phasor-based modelling approach allows larger time-steps to be used if fewer details are considered. This will directly benefit the computational intensity and thereby the speed of simulations. Simulation at different time-steps will have implications on data transfer through the interface. Since data-point granularity between the two sides will be different, interpolation (or extrapolation) needs to be employed to create samples that equalize the granularity at the interface. A two time-step simulation approach using the latency of the transmission line was first proposed in [52]. Numerical stability and accuracy aspects of multi-rate EMT simulation by exploiting the inherent latency of transmission lines are presented in [53]. This chapter presents multi-rate DP-EMT co-simulation approaches using the latency of transmission line and multi area Thévenin equivalent technique with illustrative examples.

4.2 Use of Transmission Line Delay

Assume that the DP and EMT sides of the network are simulated using time-steps of ΔT and Δt , respectively, and that the travel-time of the transmission line interface (i.e., τ) is greater than the time-step size of the DP side. This implies that the one-step interface used earlier is no longer applicable. However, this situation can be handled, as is conventionally done in EMT simulators, by keeping history values in a buffer whose length is $N = \tau / \Delta t$. Without significant practical limitation, it is further assumed that ΔT is an integer multiple of Δt . The time-step ratio, n , is defined as follows.

$$\Delta T = n\Delta t \quad (4-1)$$

Figure 4-1 shows a DP-EMT multi-rate simulation strategy using the travel-time of a transmission line. In this strategy, the DP subsystem is only solved at every integer multiple of the large time-step, ΔT , and EMT subsystem is solved at every integer multiple of the small time-step, Δt . As a result of (4-1), DP and EMT solutions are synchronized at $k\Delta T$, where k is an integer. Furthermore, between two consecutive complete DP solutions, there are $n-1$ instances of the small time-step where only the EMT solution is calculated. As shown in Figure 4-1(a), in order to calculate the DP side current injection at $k\Delta T$, past information (i.e., voltage and current) from the EMT side calculated at $k\Delta T - \tau$ is required. Similarly, to calculate the EMT side current injection at $k\Delta T$, DP-side information at $k\Delta T - \tau$ is required. This information may not be readily available as the DP solution at $k\Delta T - \tau$ is not necessarily ‘calculated’. The required intermediate data points, however, can be estimated by linearly interpolating the DP solutions at $(k-2)\Delta T$ and $(k-1)\Delta T$. In this scheme,

4.2 Use of Transmission Line Delay

interpolation is done for the dynamic phasor quantities; as a result, the error is less for low-frequency transients around the base frequency.

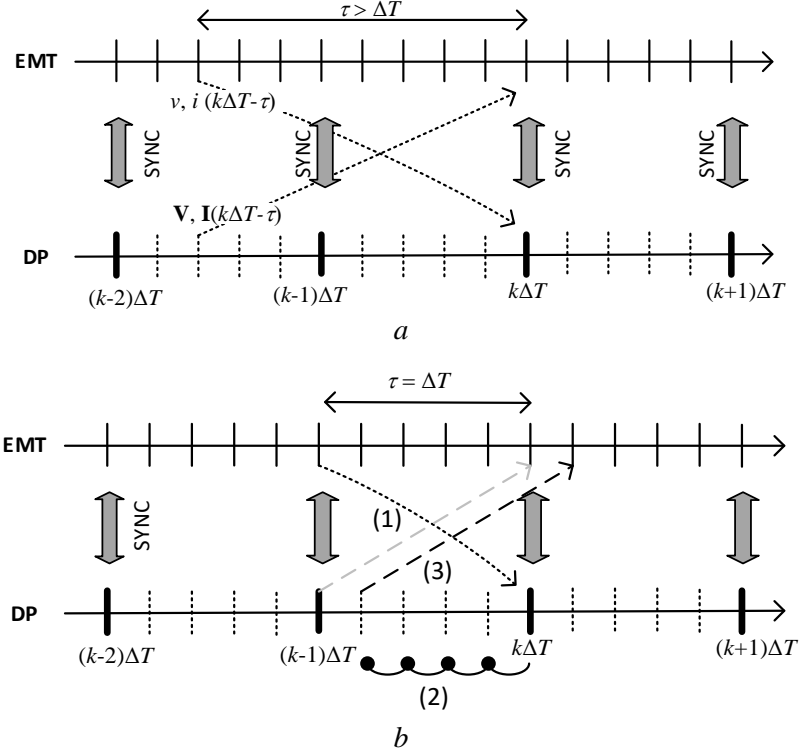


Figure 4-1 DP-EMT multi-rate simulation strategy using traveling delay

a. 1:5 time-step ratio and $\tau > \Delta T$

b. 1:5 time-step ratio and $\tau = \Delta T$

Figure 4(b) shows the time line of a two time-step DP-EMT simulation for a 1:5 time-step ratio and $\tau = \Delta T$. The sequence of operations for this scenario is as follows:

- 1) At synchronisation point $k\Delta T$, obtain the solution of both EMT and DP sides using the history values at $(k-1)\Delta T$.
- 2) Find the intermediate DP quantities by interpolating the values at $(k-1)\Delta T$ and $k\Delta T$.
- 3) Continue EMT simulation using interpolated DP values until next synchronization point at $(k+1)\Delta T$.

4.2 Use of Transmission Line Delay

Simulation results of the network in Figure 3-4 for a DP-EMT co-simulation conducted with time-steps of 100- μ s and 10- μ s for the dynamic phasor and EMT simulators, respectively, are shown in Figure 4-2. The parameters of the lossless line interface are changed to obtain a travel-time through the interface equal to the time-step of the dynamic phasor side (i.e., 100- μ s). Figure 4-2 also shows EMT simulation results (no interfacing) for a simulation time-step of 10- μ s for comparison. As seen the interface successfully transfers all low-frequency transient information and shows conformity in following slow transients after fault clearance, showing the low-pass filtering effect of interpolation. Note that this is not a limitation imposed by the interfacing technique, but is rather a by-product of the simulation at two different time-steps.

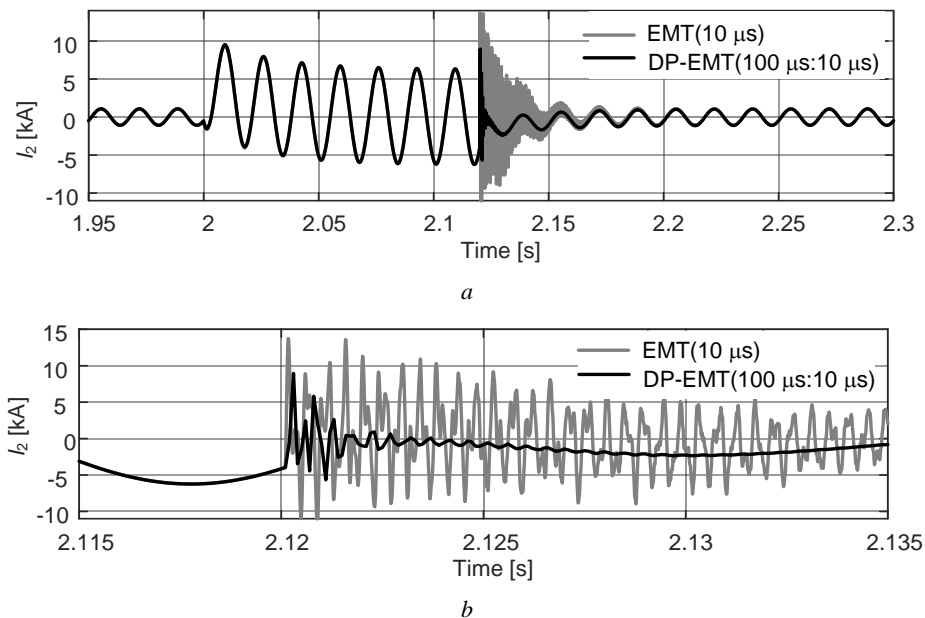


Figure 4-2 Multi-rate simulation results of the network in Figure 3-4

- a. DP-EMT co-simulation with full harmonic augmentation*
- b. Zoomed-in view of the transient after fault clearance*

4.2 Use of Transmission Line Delay

The maximum DP-side time-step of the DP-EMT co-simulation approach discussed is dependent on the transmission line delay. If the two subsystems are connected via a transmission line that has a travel time delay of τ , then a two time-step simulation strategy can be implemented if the condition $\Delta T \leq \tau$ is satisfied. The approximate minimum length (l_{\min}) of a transmission line to satisfy this condition assuming the speed of light at 3×10^5 km/s as follows:

$$l_{\min} \approx 3 \times 10^5 \times \Delta T \quad (4-2)$$

For example, this implies that in order to run the DP-side of co-simulator at a 500- μ s time-step, a 150-km (minimum) transmission line must be available.

4.2.1 Simulation of Large Networks

To assess the performance of the proposed interfacing algorithm, networks consisting of a larger number of nodes, including IEEE 12-bus [54], 39-bus and 118-bus systems [55], are considered. All test system data are given in Appendix E. These networks are simulated using both an EMT simulator and the proposed DP-EMT co-simulator with different time-steps. Computing time required for each simulation is recorded and used for comparative assessment of speed gains.

A single-line diagram of the IEEE 12-bus system is shown in Figure 4-3. The system model (three-phase) is implemented in both EMT and DP-EMT simulators. Transmission lines are modelled as π -sections. Portions of the series inductance (L) and shunt capacitance (C) of lines TX1 and TX3 where segmentation is applied are included in the interfaces where Z_c is 500 Ω and travelling delay (τ) is 200- μ s. The EMT model is executed with a

4.2 Use of Transmission Line Delay

20- μ s time-step. DP-EMT simulations are conducted with 200- μ s:20- μ s time-steps (10:1 ratio) and results are shown in Figure 4-4, when three-phase solid line-to-ground faults lasting 6 cycles are applied at buses 1 and 2. Figure 4-4 clearly shows the ability of the co-simulator in capturing low-frequency transients.

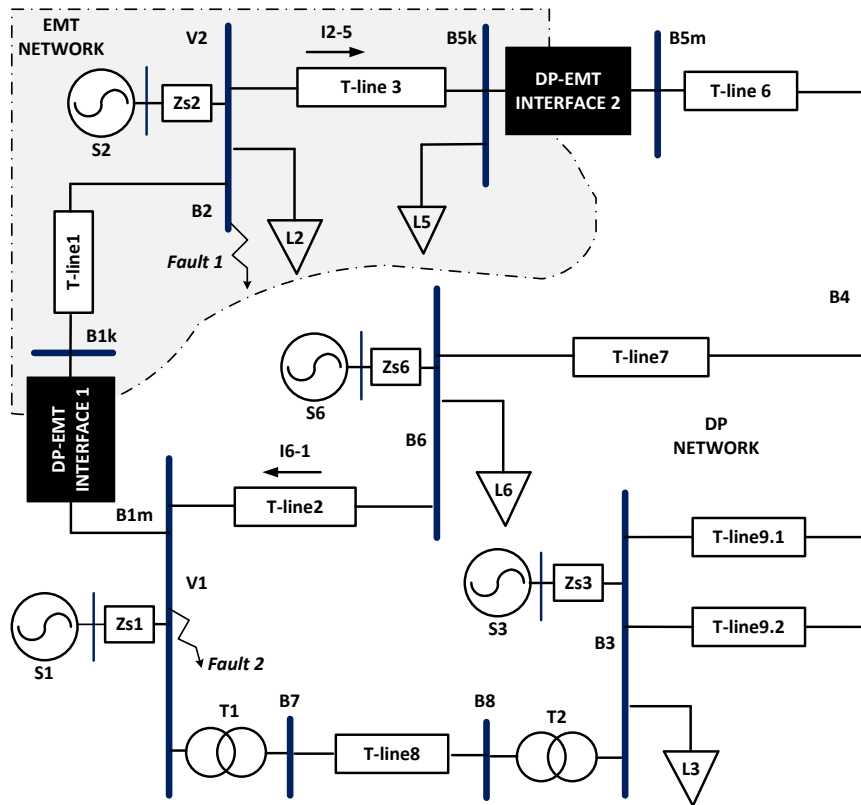
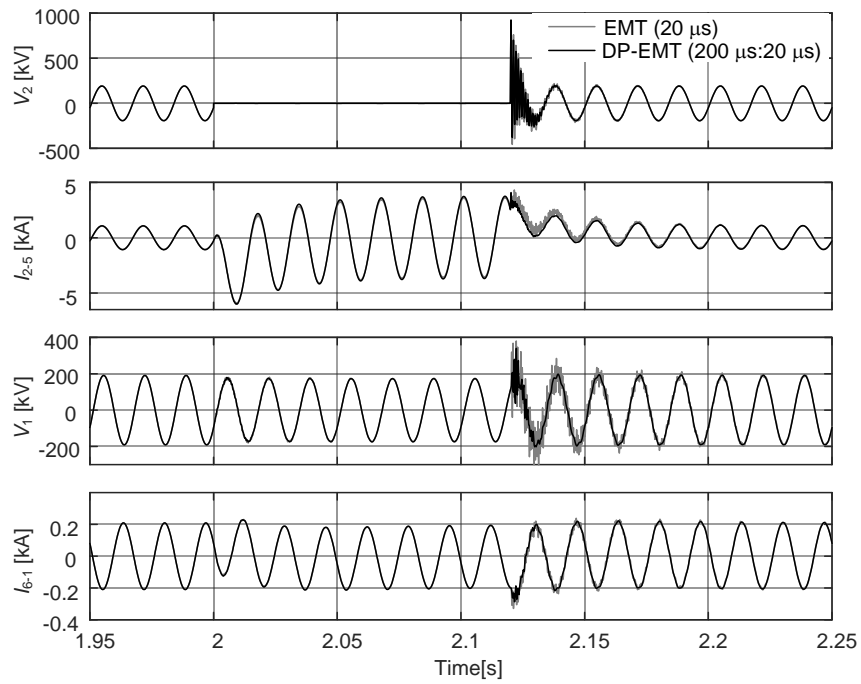


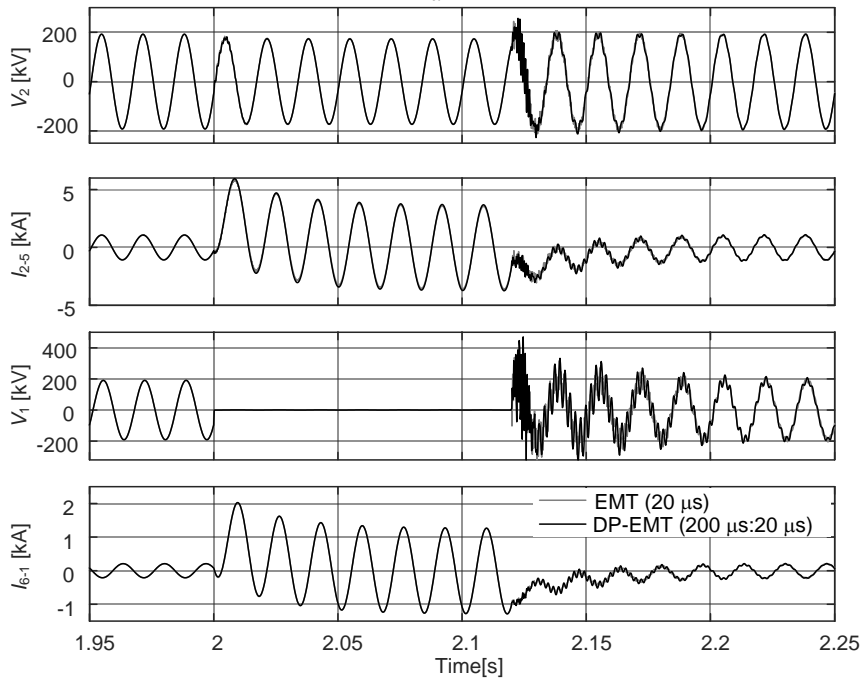
Figure 4-3 IEEE 12-bus system with the DP-EMT interfaces at buses 1 and 5

Simulation of the IEEE 12-bus network is also conducted with a 50:1 time-step ratio; additionally, IEEE 39-bus and IEEE 118-bus networks are also simulated using the DP-EMT simulator with 10:1 and 50:1 time-step ratios as shown in Table 4-1, where corresponding computing times are given.

4.2 Use of Transmission Line Delay



a



b

Figure 4-4 Simulation results of the IEEE 12-bus system using the DP-EMT simulator

- a.* Transients following fault-1
- b.* Transients following fault-2

4.3 Use of MATE Technique

Table 4-1 CPU time to complete a 10 s simulation

| Test system | CPU-time and speed-up gain rel. to the EMT simulation (in brackets) | | |
|--------------|---|---|--|
| | EMT ($\Delta t = 20\text{-}\mu\text{s}$) | DP-EMT (200- μs :20- μs) | DP-EMT (1000- μs :20- μs) |
| IEEE 12-bus | 7.5 | 6.0 s, (1.25) | 3.9 s, (1.92) |
| IEEE 39-bus | 21.4 | 12.5 s, (1.71) | 6.1 s, (3.50) |
| IEEE 118-bus | 164.2 | 32.1 s, (5.12) | 7.4 s, (22.19) |

In the co-simulation results in Table 4-1, the EMT portion of each network contains 3 buses with a single source, where in practice this source may represent a complex subsystem such as a detailed wind-farm model. Note that the savings in computing time are significant in particular when the network size grows, as evidenced by the speed-up gains for the IEEE 118-bus system in comparison to those of the smaller 39-bus and 12-bus networks.

4.3 Use of MATE Technique

The maximum DP-side time-step of the DP-EMT co-simulation approach discussed in the previous section depends on the transmission line delay. In order to have large traveling delays, long transmission lines need to be considered. For instance, a transmission line of 300 km must be available to simulate the DP-side network at a 1000- μs time-step. This limits the flexibility of the co-simulation technique due to the fact that long transmission lines are not always available at the location of the interface. Further, the transmission line models found in the literature that enable use of larger time-steps than the travel time delay do not provide decoupling between their two ends [56]. Therefore such transmission line models are not suitable for use in this approach to achieve large time-step ratios. In order

4.3 Use of MATE Technique

to overcome this issue, this thesis proposes a novel multi-rate DP-EMT approach based upon the “Multi-Area Thévenin Equivalents” (or MATE) concept described in [57].

4.3.1 MATE Formulation

In the MATE technique, the network is first partitioned into subsystems and a partial solution (Thévenin source voltage) is obtained for each subsystem by considering them as independent entities. Then the simplified systems with multimode Thévenin equivalents are used to calculate currents through linking branches. Finally, the complete solution is obtained by injecting linking branch currents to appropriate nodes of each subsystem.

The MATE concept described in [57] can be applied to the system in Figure 4-5 as follows.

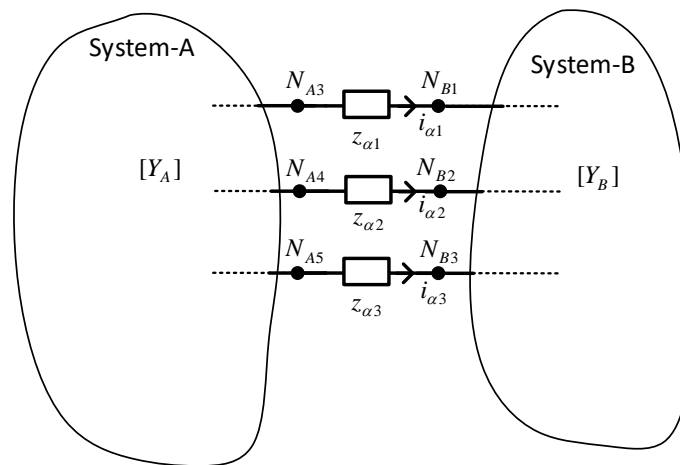


Figure 4-5 Two subsystems connected by three linking branches

The system A has N nodes and system B has M nodes. There are three linking branches between the systems A and B. The following notations are used:

4.3 Use of MATE Technique

| | |
|--|--|
| $[Y_A], [Y_B]$ | Admittance matrices of subnetworks A and B |
| $i_{\alpha 1}, i_{\alpha 2}, i_{\alpha 3}$ | Currents through linking branches from A to B |
| $z_{\alpha 1}, z_{\alpha 2}, z_{\alpha 3}$ | Impedance of the linking branches |
| $[h_A], [h_B]$ | Nodal current injection of subnetworks A and B |

The equations of the three linking branches are given by

$$\begin{aligned}
 v_{A3} - v_{B1} - z_{\alpha 1} i_{\alpha 1} &= 0, \\
 v_{A4} - v_{B2} - z_{\alpha 2} i_{\alpha 2} &= 0, \\
 v_{A5} - v_{B3} - z_{\alpha 3} i_{\alpha 3} &= 0.
 \end{aligned}
 \tag{4-3}$$

Using modified nodal analysis, the network equations of systems A and B can be put into a “common container” as follows:

| | | | | | |
|----------|----------|----------|----------|------------|-------|
| | <i>A</i> | <i>B</i> | α | | |
| <i>A</i> | $[Y_A]$ | 0 | p | v_A | h_A |
| <i>B</i> | 0 | $[Y_B]$ | q | v_B | h_B |
| α | p^t | q^t | $-[z]$ | i_α | 0 |

$=$

$\tag{4-4}$

where

4.3 Use of MATE Technique

$$p = \begin{bmatrix} 0 & 0 & 0 \\ 0 & 0 & 0 \\ 1 & 0 & 0 \\ 0 & 1 & 0 \\ 0 & 0 & 1 \\ 0 & 0 & 0 \\ \cdot & \cdot & \cdot \\ \cdot & \cdot & \cdot \\ \cdot & \cdot & \cdot \\ 0 & 0 & 0 \end{bmatrix}_{N \times 3}, \quad q = \begin{bmatrix} -1 & 0 & 0 \\ 0 & -1 & 0 \\ 0 & 0 & -1 \\ 0 & 0 & 0 \\ \cdot & \cdot & \cdot \\ \cdot & \cdot & \cdot \\ \cdot & \cdot & \cdot \\ 0 & 0 & 0 \end{bmatrix}_{M \times 3} \quad \text{and} \quad z = \begin{bmatrix} z_{\alpha 1} & 0 & 0 \\ 0 & z_{\alpha 2} & 0 \\ 0 & 0 & z_{\alpha 3} \end{bmatrix}_{3 \times 3} \quad (4-5)$$

,

$$i_{\alpha} = [i_{\alpha 1}, i_{\alpha 2}, i_{\alpha 3}]^T.$$

Multiplying rows A and B of (4-4), respectively, by $[Y_A]^{-1}$ and $[Y_B]^{-1}$, this equation can be written as

| | | | | | | |
|----------|---|---|--------------|--------------|---|--------------|
| | A | B | α | | | |
| A | 1 | 0 | a | | | |
| B | 0 | 1 | b | | | |
| α | 0 | 0 | Z_{α} | | | |
| | | | | v_A | | e_A |
| | | | | v_B | = | e_B |
| | | | | i_{α} | | e_{α} |

where

$$a = [Y_A]^{-1} p,$$

$$b = [Y_B]^{-1} q,$$

$$e_A = [Y_A]^{-1} h_A,$$

$$e_B = [Y_B]^{-1} h_B,$$

4.3 Use of MATE Technique

$$\begin{aligned} Z_{\alpha} &= p^t a + q^t b + z; Z_{th_A} = p^t a \text{ and } Z_{th_B} = q^t b, \\ e_{\alpha} &= p^t e_A + q^t e_B; E_{th_A} = p^t e_A \text{ and } E_{th_B} = q^t e_B. \end{aligned} \quad (4-7)$$

The currents in the linking branches are calculated as follows:

$$[i_{\alpha}] = [Z_{\alpha}]^{-1} [e_{\alpha}]. \quad (4-8)$$

In the MATE solution process using (4-7), E_{th_A} and E_{th_B} are calculated considering the systems A and B as totally isolated (i.e., without considering the linking branches). Then using (4-8), the linking current vector $[i_{\alpha}]$ is calculated. The complete solution of the subsystem is obtained by injecting the linking currents to the corresponding nodes and solving the sub systems independently.

In case of numerical computing, the MATE solution process will cost more CPU time as it involves additional steps over solving the entire system at once. However, this drawback is insignificant when multi-rate solution between two subsystems is considered.

4.3.2 Adapted MATE Formulation for the DP-EMT

Since the network equation formulations in DP and EMT sides are different (i.e., complex and real), the MATE technique is not readily applicable to the DP-EMT co-simulation. However, MATE approach can be used only for the DP side, if the DP and EMT sides are decoupled using a transmission line as described in Chapter 3.

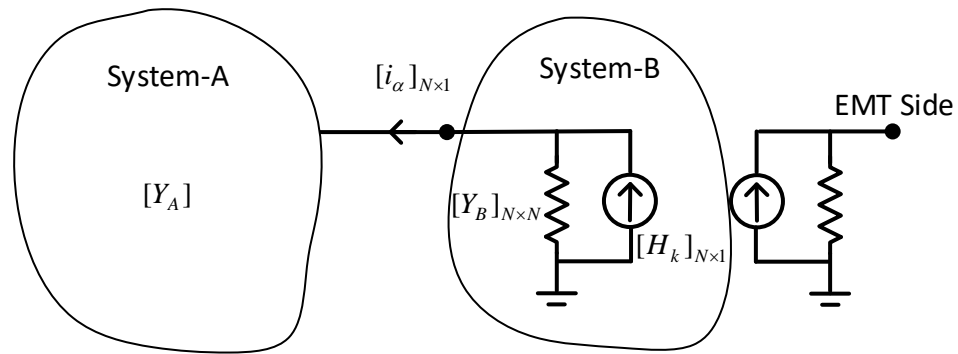


Figure 4-6 Partitioned DP network

Consider a DP-EMT hybrid system where the two sides are connected via a transmission line interface as shown in Figure 4-6. There are N interfacing branches at the interface. For instance, a three phase transmission line will have three interfacing branches. In order to employ the MATE technique, the DP network is partitioned into two subsystems such that the system A represents the external electrical system and the system B represents the nodal current injection circuits of the transmission line interface (i.e., history current sources and the characteristic impedances).

As the system B topology is specifically known, the generalised MATE formulation shown in equations (4-3)-(4-8) can be further simplified. For instance, the impedances of the linking branches are considered to be zero and the system B only consists of nodal current injection sources. Figure 4-7 shows the Thévenin equivalent representation of the system using the MATE approach. The Thévenin source quantities (i.e., E_{th_A} and Z_{th_A}) of the system A are calculated using (4-7).

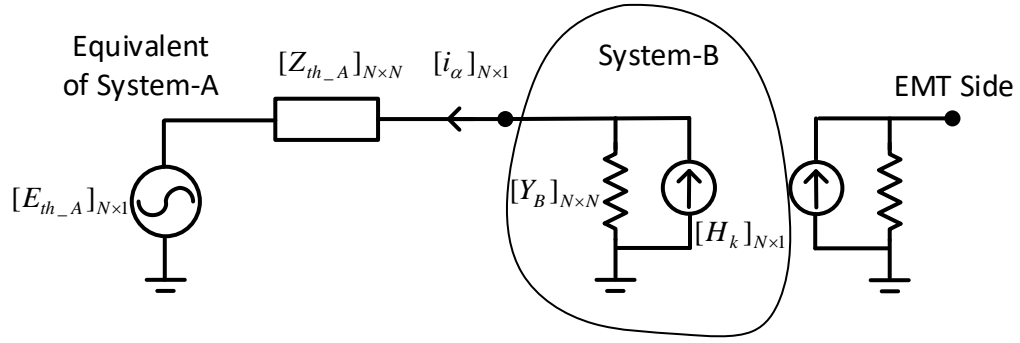


Figure 4-7 Thévenin equivalent representation of the System-A in Figure 4-6

4.3.3 Multi-Rate DP-EMT Solution using MATE

Assume that the DP and EMT sides of the network are simulated using time-steps of ΔT and Δt , respectively. Without significant practical limitation, it is further assumed that ΔT is an integer multiple of Δt . The time-step ratio, n , is defined as follows.

$$\Delta T = n\Delta t \tag{4-9}$$

Figure 4-8 shows the time line of the DP-EMT multi-rate simulation strategy using the MATE technique.

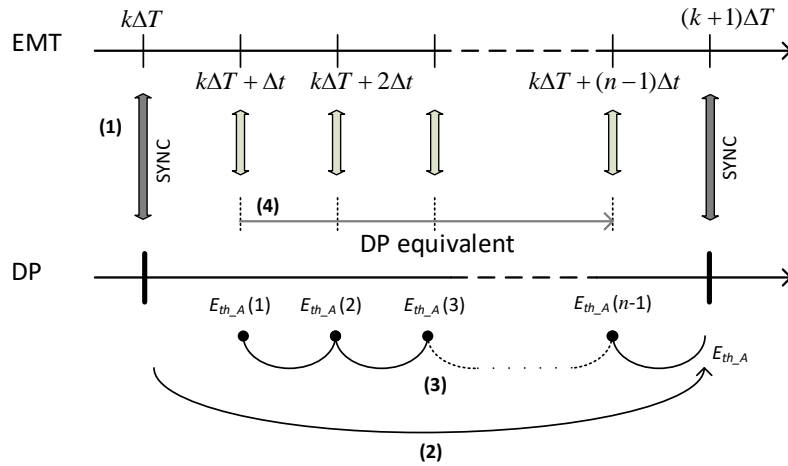


Figure 4-8 Time line of DP-EMT multi-rate simulation strategy using MATE

4.3 Use of MATE Technique

In this strategy, the DP subsystem is only solved at every integer multiple of the large time-step, ΔT , and the EMT subsystem is solved at every integer multiple of the small time-step, Δt . As a result of (4-9), DP and EMT solutions are synchronized at $k\Delta T$. Furthermore, between two consecutive complete DP solutions, there are $n-1$ instances of the small time-step Δt . Once the complete DP solution is obtained at $k\Delta T$, equation (4-7) are used to calculate the Thévenin source matrix at $(k+1)\Delta T$. Intermediate Thévenin source values are calculated by interpolating the Thévenin source values at $k\Delta T$ and $(k+1)\Delta T$. The DP solutions at the intermediate time steps (i.e., $k\Delta T + \Delta t$, $k\Delta T + 2\Delta t$, ...) are calculated considering only the Thévenin equivalent and the system B as shown in Figure 4-7.

The sequence of operations for this scheme is as follows:

- 1) At synchronisation point $k\Delta T$, obtain the solution of both EMT and complete DP side solution.
- 2) Using the DP network solution at $k\Delta T$, calculate the Thévenin source matrix E_{th_A} at $(k+1)\Delta T$.
- 3) Find the intermediate Thévenin source matrices by interpolating Thévenin source matrices at $(k+1)\Delta T$ and $k\Delta T$.
- 4) Continue EMT simulation using Thévenin equivalent at DP side until next synchronization point at $(k+1)\Delta T$.

The simulation results of the sample network in Figure 3-4 using the MATE technique at different time-step ratios are shown in Figure 4-9. Each subplot also shows the EMT simulation results with 20- μ s time-step as the baseline for comparison.

4.3 Use of MATE Technique

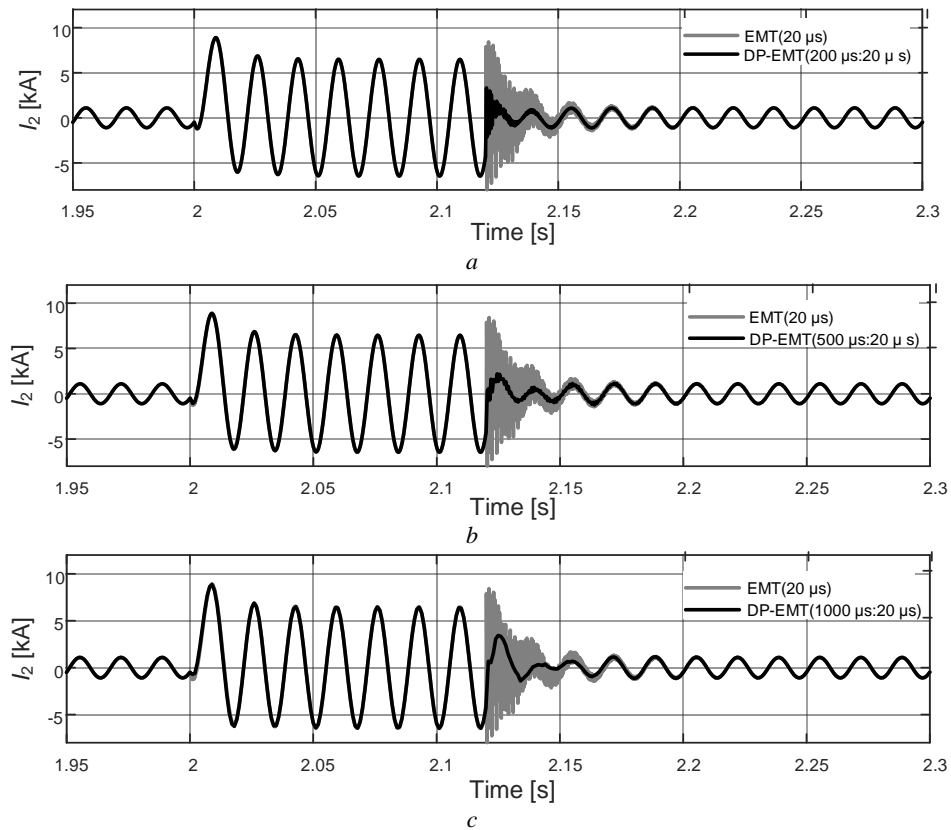


Figure 4-9 Multi-rate simulation results of the network in Figure 3-4

- a. DP-EMT co-simulator with 200- μ s:20- μ s time-step ratio*
- b. DP-EMT co-simulator with 500- μ s:20- μ s time-step ratio*
- c. DP-EMT co-simulator with 1000- μ s:20- μ s time-step ratio*

As seen in Figure 4-9, the proposed multistep DP-EMT interface employing the MATE technique is able to successfully transfer all low-frequency transient information and shows conformity in following slow transients after fault clearance. Further, high frequency oscillations immediately after fault clearance show different levels of damping for different time-step ratios. Further investigations have revealed that this is due to the aliasing effect because the frequency of the transient waveform is higher than the sampling frequency. In this example, high-frequency oscillations in the current waveform are resulted by switching operating of the resistive branch that represents the fault in a practical situation. Typically,

4.3 Use of MATE Technique

real-world fault clearance happens close to the zero-crossing point of the current waveform (at the circuit breaker), hence post fault-clearance transients may not have high frequency oscillations as shown in this simulation. However, this example purposely considered the non-zero-crossing fault clearance operation to investigate the impact of such transients on the multi-rate DP-EMT co-simulation.

4.3.4 Simulation of a Large Network

The performance of the proposed multi-rate DP-EMT simulation technique, which uses the MATE approach, is evaluated for the IEEE 118-bus system. In this co-simulation, buses 9 and 10 are modeled in the EMT and the rest of the network is modeled in the DP domain as shown in Figure 4-10. The transmission line between the buses 9 and 8 is selected for the interface. The system is simulated with 1000- μ s:20- μ s time-steps (50:1 ratio). Figure 4-11 shows the transient response of the system when a three-phase, solid line-to-ground fault lasting 6 cycles is applied at bus 9. Further, each subplot also shows the full EMT simulation results with 20- μ s time-steps for comparison.

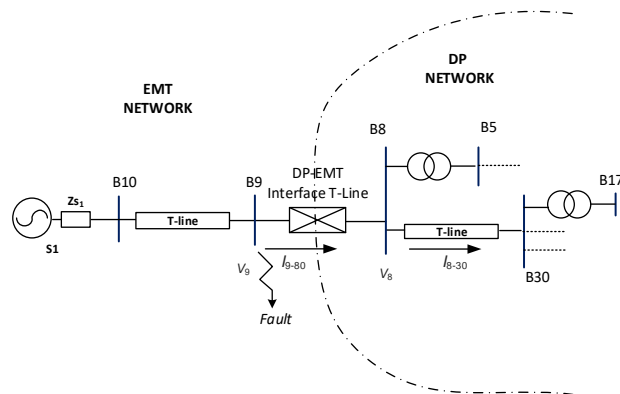


Figure 4-10 Segmented IEEE 118-bus test system

4.3 Use of MATE Technique

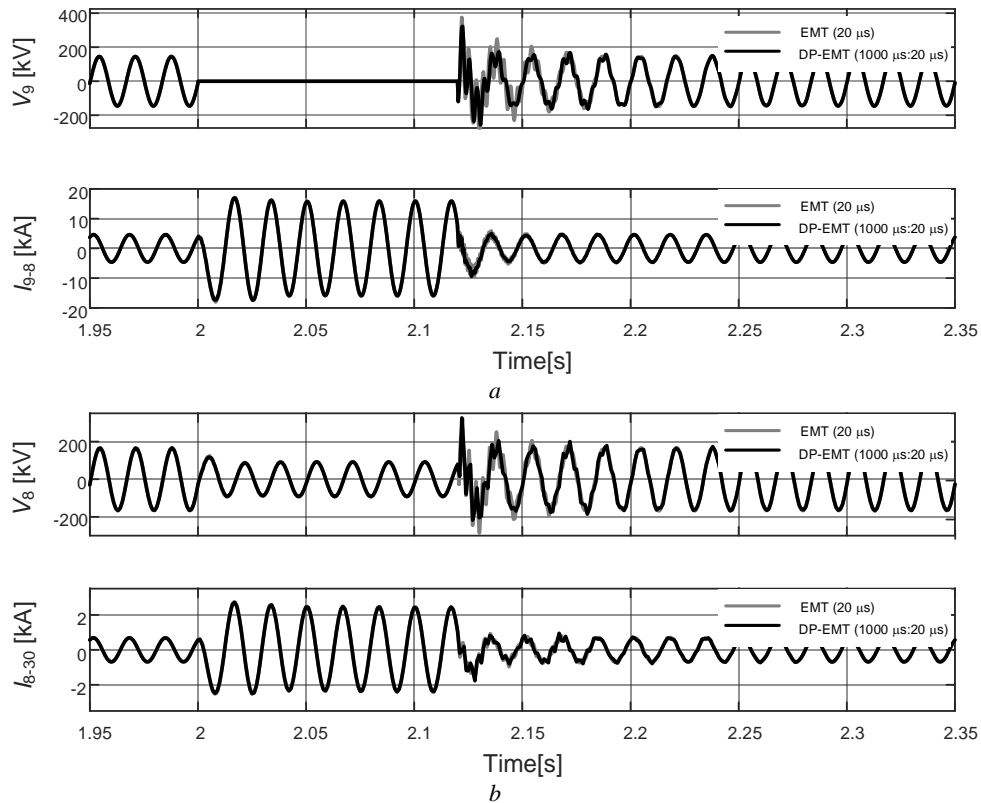


Figure 4-11 Instantaneous current and voltage waveforms at bus 9 (top two plots) and 8 (bottom two plots)

a. EMT side plots of the DP-EMT co-simulator with 1000- μ s:20- μ s time-step ratio

b. DP side plots of the DP-EMT co-simulator with 1000- μ s:20- μ s time-step ratio

Simulation results in Figure 4-11 clearly show the ability of the multi-rate co-simulator in capturing low-frequency transients accurately. The CPU time required to run a 10 s duration is measured at 9.3 s whereas the fully EMT simulation required 164.2 s. This gives a speed gain of 17.6 over full EMT simulation. Therefore, the proposed DP-EMT multi-rate simulation technique provides substantial saving in simulation time for this scenario.

4.4 Chapter Summary and Contribution

A multi-rate co-simulation strategy using the traveling delay of the interfacing transmission line was presented. The implications of this strategy on the length of the interfacing transmission line were also discussed. In order to overcome the limitation in the transmission line delay approach a novel DP-EMT multi-rate co-simulation strategy was presented using the MATE technique.

Chapter 5

Simulation Examples

5.1 Introduction

The multi-rate DP-EMT co-simulation approaches discussed in Chapter 4 are applied to considerably larger networks. Significant simulation speed gain can be achieved from the DP-EMT co-simulation when the DP subsystem becomes larger and comprises many dynamic devices. In this exercise, it is essential to have a DP model for a synchronous machine as synchronous machines are virtually always an integral part of any large power system. This chapter first discusses the dynamic phasor implementation of the synchronous machine model. Then several simulation examples are presented using the IEEE 39-bus and IEEE 118-bus systems. Further, the DP simulator is integrated with a commercial EMT simulator (PSCAD/EMTDC) and one simulation example is presented with IEEE 118-bus system where a windfarm is simulated at the EMT side.

5.2 Synchronous Machine Model

Synchronous machine modeling for power system simulation has been a popular research topic. With the advent of digital computers numerous machine models have been developed by focusing on different aspects of their modeling. The user has to select a proper model for a particular application considering various factors such as the required level of accuracy, speed of simulation, location of the fault (internal or external), etc. The interfacing technique used to exchange data between a machine model and the external network is important to maintain numerical stability for simulation at larger time-steps [58]. Several synchronous machine models implemented in DP applications can be found in literature. The machine models proposed in [20] and [59] have rotor-position-dependent interfacing circuits to connect with the external network. Such an interfacing method is not efficient for large system simulation as the network matrix has to be recalculated for every time-step of the simulation.

As a result of direct machine-network interfacing, the voltage-behind-reactance (VBR) synchronous machine formulation offers numerical stability to the simulation [58]. The stator voltage equation of the VBR formulation can be expressed as follows [60]:

$$v_{abc} = R_s i_{abc} + \frac{d}{dt} [L''_{abc}(\theta_r) i_{abc}] + e''_{abc} \quad (5-1)$$

The stator resistance matrix R_s , sub-transient inductance $L''_{abc}(\theta_r)$, and sub-transient voltages e''_{abc} are defined in Appendix B. The VBR synchronous model is numerically inefficient to simulate large networks as a result of the sub-transient inductance matrix

5.2 Synchronous Machine Model

being dependent on the rotor position except in the special case where L''_{md} and L''_{mq} are equal, i.e., a round-rotor synchronous machine [61].

In order to overcome the deficiency of the VBR method, different approaches have been proposed to make the sub-transient inductance matrix independent from rotor position. One method uses an artificial damper winding with tuned parameters [61] and another approach derives the implicit constant-parameter VBR (CP-VBR) formulation and then uses a numerical approximation to break the algebraic loop [62]. Appendix C shows the CP-VBR formulation in detail. This thesis implements the CP-VBR synchronous machine model proposed for shifted frequency application [63]. Appendix D shows the formulas used to convert the stator dynamic phasor quantities to d-q quantities and vice versa. This synchronous machine model implementation does not consider the magnetic saturation effects within the machine.

5.2.1 Validation of the CP-VBR Synchronous Machine Model

The implemented CP-VBR synchronous machine model is validated against a Norton current-source type model in a commercial EMT simulator (PSCAD/EMTDC). A simple test system illustrated in Figure 5-1 is used in both the EMT and DP-based simulations. In this balanced three-phase system, two sources are connected at the ends of a segmented 230-kV, 60-Hz R - L network. Per-unit impedances of each segment are tabulated in Table 5-1. The source at the left end is represented by the corresponding machine model (CP-VBR or Norton current-source type) and the source at right end is represented by a voltage source. A three-phase, 835-MVA, 230-kV, 60-Hz, two-pole machine with inertia of 5.6 s

5.2 Synchronous Machine Model

is considered. The machine has the following per-unit impedance parameters on the bases of 835 MVA/230 kV [64].

$$r_s = 0.003 \text{ pu}, X_{ls} = 0.19 \text{ pu}, X_{mq} = 1.61 \text{ pu}, r'_{kq1} = 0.00178 \text{ pu}, X'_{lkq1} = 0.8125 \text{ pu},$$

$$r'_{kq2} = 0.00841 \text{ pu}, X'_{lkq2} = 0.0939 \text{ pu}, X_{md} = 1.61 \text{ pu}, r'_{fd} = 0.000929 \text{ pu}, X'_{lfd} = 0.1414 \text{ pu},$$

$$r'_{kd} = 0.001334 \text{ pu}, X'_{lkd} = 0.08125 \text{ pu}.$$

Initial conditions of the sources are selected to transfer 750 MW from the synchronous machine to the infinite source. A line-to-ground fault is applied at bus B₂ at $t = 2.0$ s and cleared at $t = 2.1$ s. The fault impedance is modelled as a variable resistor with off and on values of 1 M Ω and 0.01 Ω , respectively. Simulations are conducted once with the DP simulator and once with the PSCAD/EMTDC simulator both with a 40- μ s time-step.

Table 5-1 Per-unit impedance of network elements (base values: 230 kV/ 100 MVA)

| Segment | R [pu] | X [pu] |
|---------|--------|--------|
| Z_t | - | 0.0250 |
| $R-L$ | 0.0006 | 0.0092 |
| Z_c | - | 0.0071 |

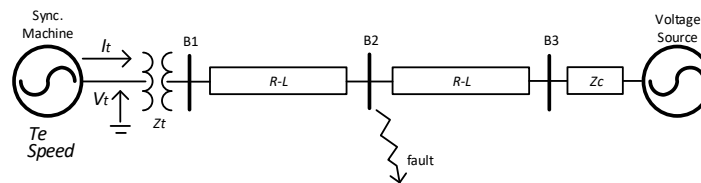


Figure 5-1 Simple test system with a synchronous machine

5.2 Synchronous Machine Model

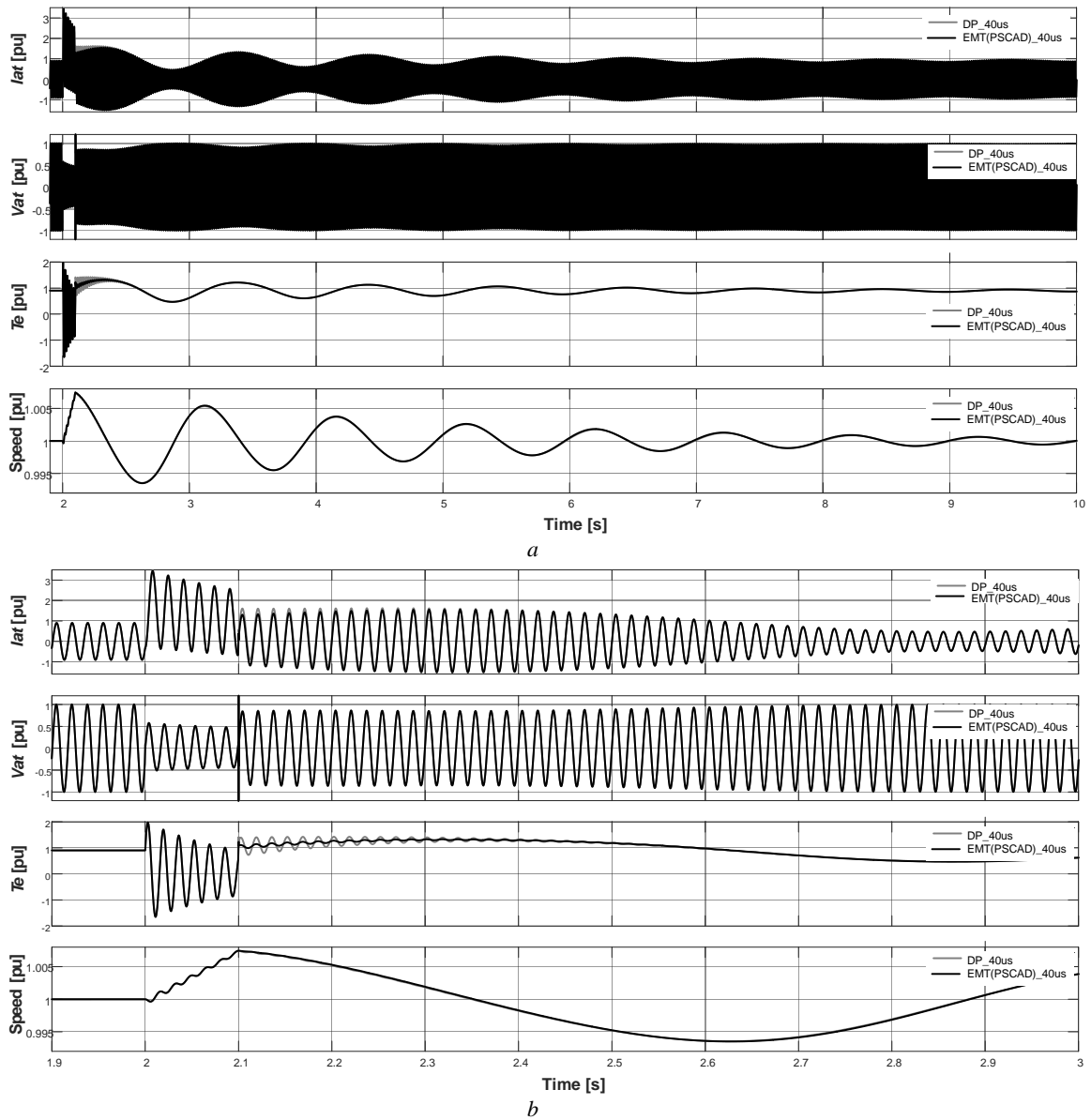


Figure 5-2 Comparison of synchronous machine models in DP (CP-VBR) and EMT (PSCAD Norton Current Injection)

a. Instantaneous voltage (V_{at}) and current (I_{at}) waveforms (phase-a) at the generator terminal, electrical torque (T_e) and mechanical speed ($Speed$)

b. Zoomed-in view of (a)

Note: The I_{at} and V_{at} in Figure 5-2 are per unitised with respect to the peak-line-current base and the peak line-to-neutral voltage base.

5.2 Synchronous Machine Model

According to the results shown in Figure 5-2, the CP-VBR model shows excellent conformity with the PSCAD/EMTDC results. The two models have slight mismatch at the instant of fault clearance. Differences in interfacing technique and the chatter removal algorithm in the two simulators contribute to these minute differences.

In order to investigate the impact of the time-step on the accuracy, models are run at different time-steps and compared with the 40- μs results as shown in Figure 5-3. The results show that the waveforms of EMT Norton current injection model significantly vary with the time-step and also the model becomes numerically unstable at a time-step of 1550 μs . However, the CP-VBR model shows only slight variations with time-step and also remains numerically stable even at a large 2000- μs time-step.

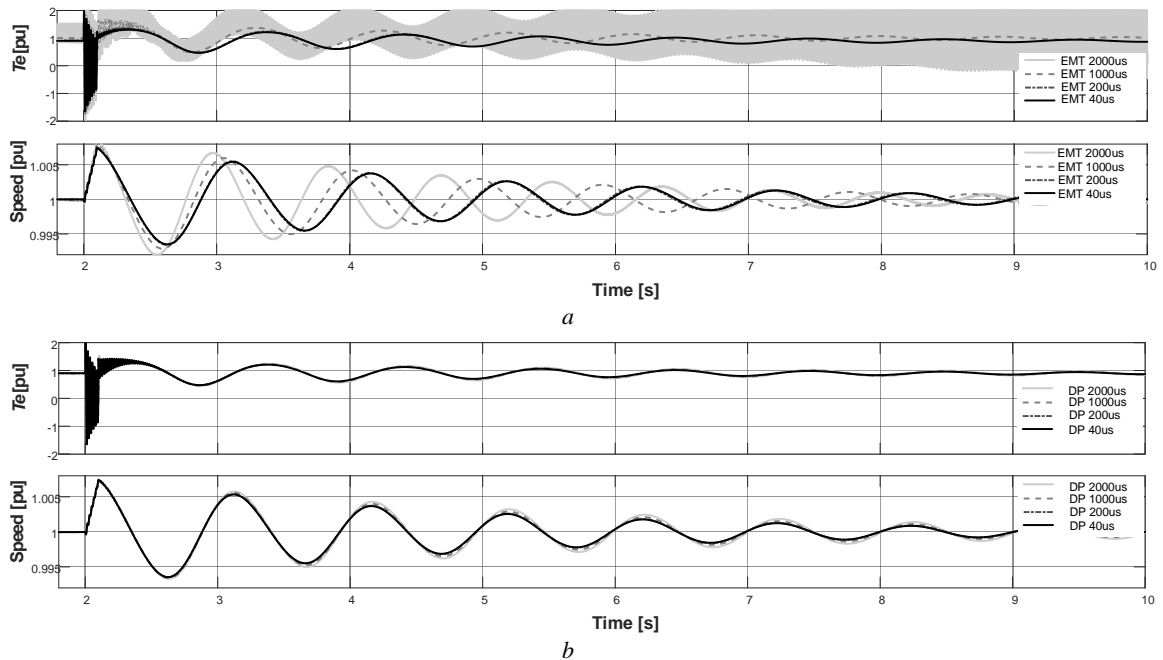


Figure 5-3 Comparison at different time-step

- a. EMT (PSCAD Norton Current Injection) model: Electrical torque (T_e) and mechanical speed (Speed)
- b. DP (CP-VBR) model: Electrical torque (T_e) and mechanical speed (Speed)

5.3 Simulation Example 1

In this example, the IEEE 118-bus system is studied to illustrate the accuracy and efficiency of the multi-rate DP-EMT simulation technique using the latency of transmission line described in Section 4.2. As shown schematically in Figure 5-4, a small portion (3 buses) of the system containing a Type-4 wind farm of 75 turbines (6 MW each) [65] is modeled in an EMT simulator (PSCAD/EMTDC) including detailed switching-level models of power electronic converters. An aggregate representation is used to model the wind farm, where only one wind turbine is simulated and is then scaled up to represent the concurrent operation of several wind turbines in the farm. The total capacity of the wind farm is 450 MW. Figure 5-5 shows the block diagram representation of the Type-4 aggregated windfarm in an EMT platform.

The remaining 115 buses of the system are modeled in the dynamic phasor domain in a custom simulation environment and the proposed DP-EMT interface is used to connect the two simulators. The existing 150-km transmission line between buses 9 and 8 is used as the DP-EMT interface. The positive-sequence parameters of this line are shown in Table 5-2. Communication between the two simulators is established using the control network interface (TCP/IP-based) of PSCAD/EMTDC.

Table 5-2 Transmission line (B₈ to B₉) positive-sequence parameters

| Parameter | Value [pu] on a 138 kV/100 MVA base |
|------------------------------|--|
| <i>R</i> (series resistance) | 0.0025 |
| <i>X</i> (series reactance) | 0.0305 |
| <i>B</i> (shunt admittance) | 1.1620 |

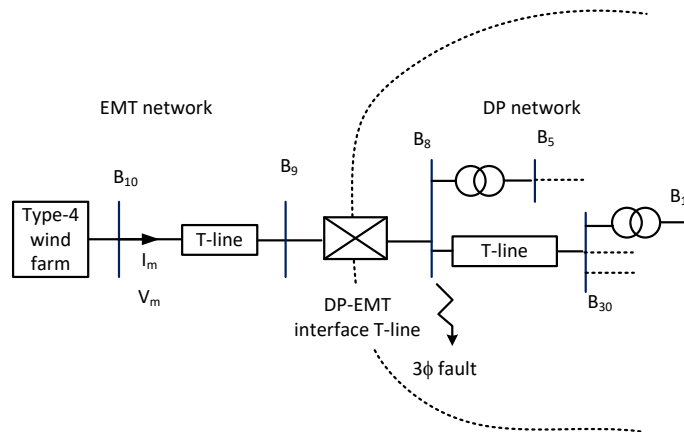


Figure 5-4 Segmented IEEE 118-bus test system with a wind farm

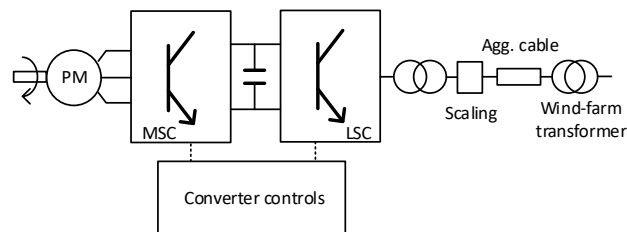


Figure 5-5 Type-4 windfarm model

Three sets of simulations are conducted: (1) a DP-EMT co-simulation with a 20- μ s time-step in both simulators; (2) a DP-EMT co-simulation with 500- μ s and 20- μ s time-steps for the DP and EMT segments, respectively; and (3) a full EMT simulation with a 20- μ s time-step. The full EMT simulation is used to validate the results of the DP-EMT co-simulations.

The first co-simulation with equal 20- μ s time-steps for both simulators is meant to verify that the co-simulator is able to replicate full EMT results. The second co-simulation with a 25:1 time-step ratio is meant to show that significant acceleration will be achieved

5.3 Simulation Example 1

with the use of a larger time-step for the dynamic phasor segment while maintaining the accuracy of representation of low-frequency oscillations.

In all simulations, a three-phase-to-ground fault is applied at bus 8 (see Figure 5-4) at 1.8 s and cleared 6 cycles later. Current and voltage measurements are captured at bus 10 (within the EMT segment) and bus 30 (within the DP segment).

Figure 5-6 shows a comparison between the results of the DP-EMT co-simulation (20- μ s:20- μ s) and the fully detailed EMT model of the whole network. These plots show that the DP-EMT simulator has complete conformity with the full EMT simulator when equal time-steps are used. This is due to the fact that fully-augmented dynamic phasors of EMT waveforms at the interface boundary are calculated and transferred to the dynamic phasor segment, thereby preserving the entire frequency spectrum of the waveform.

Figure 5-7 shows a comparison between the results of the DP-EMT co-simulation (500- μ s: 20- μ s) and the fully detailed EMT model of the whole network. These plots show that the DP-EMT simulator is able to capture the low-frequency contents of the waveforms before, during, and after the fault; some high-frequency transients are not observed in the DP-EMT results due to the fact that use of a larger time-step to gain simulation speed results in less harmonic bandwidth in the simulated waveforms.

5.3 Simulation Example 1

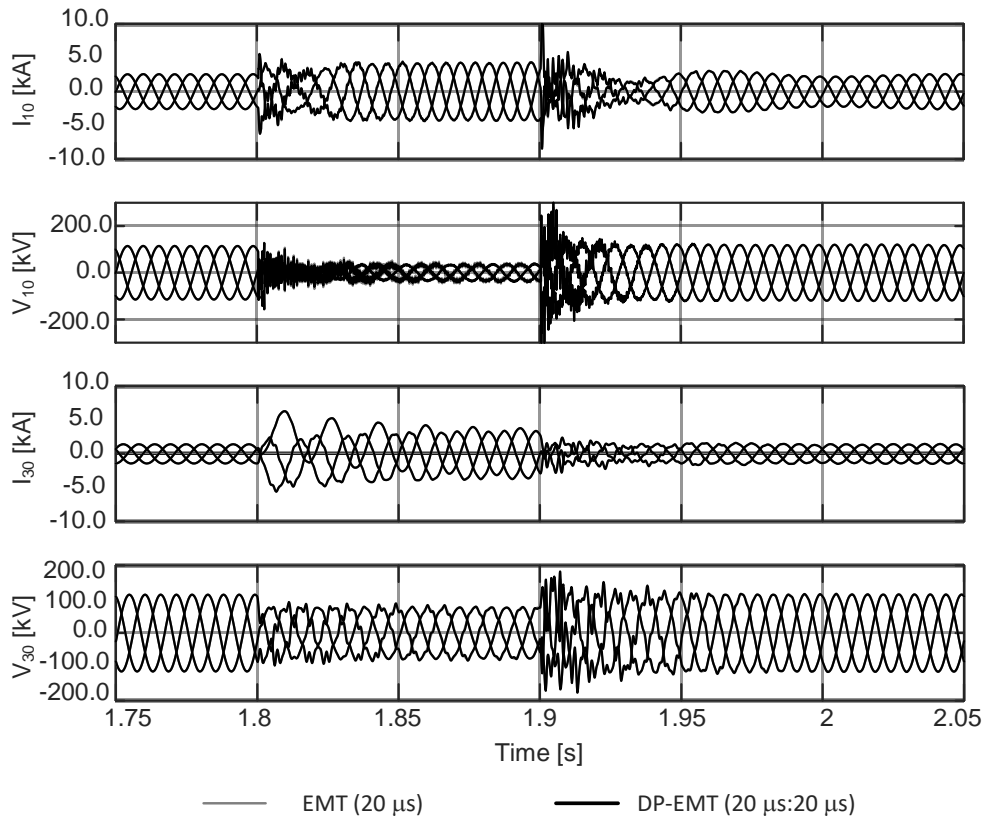


Figure 5-6 Instantaneous current and voltage waveforms at bus 10 (top two plots) and bus 30 (bottom two plots) for EMT (20- μ s) and DP-EMT (20- μ s: 20- μ s) simulations

Figure 5-8 shows a comparison of the per-unit (positive-sequence, fundamental frequency only) rms voltage as well as real and reactive power at the wind farm terminal for the DP-EMT (500- μ s:20- μ s) co-simulation. These traces clearly show the DP-EMT co-simulator closely replicates the results obtained using the full EMT model of the whole network.

5.3 Simulation Example 1

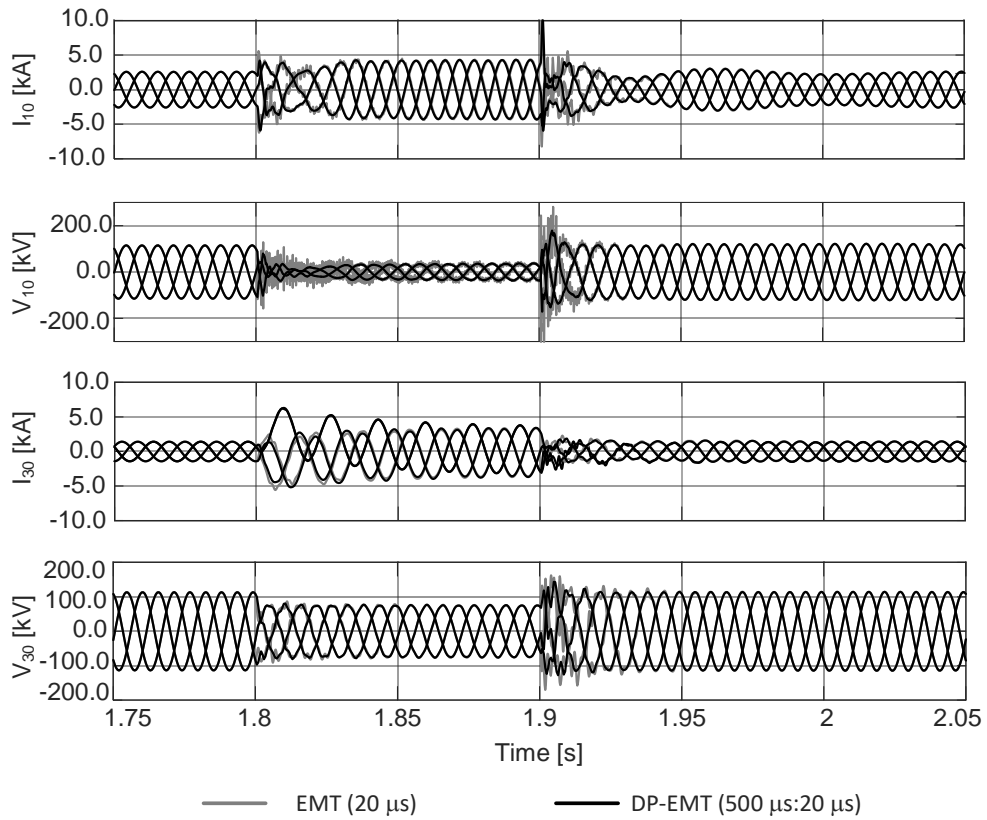


Figure 5-7 Instantaneous current and voltage waveforms at bus 10 (top two plots) and bus 30 (bottom two plots) for EMT (20- μ s) and DP-EMT (500- μ s:20- μ s) simulations

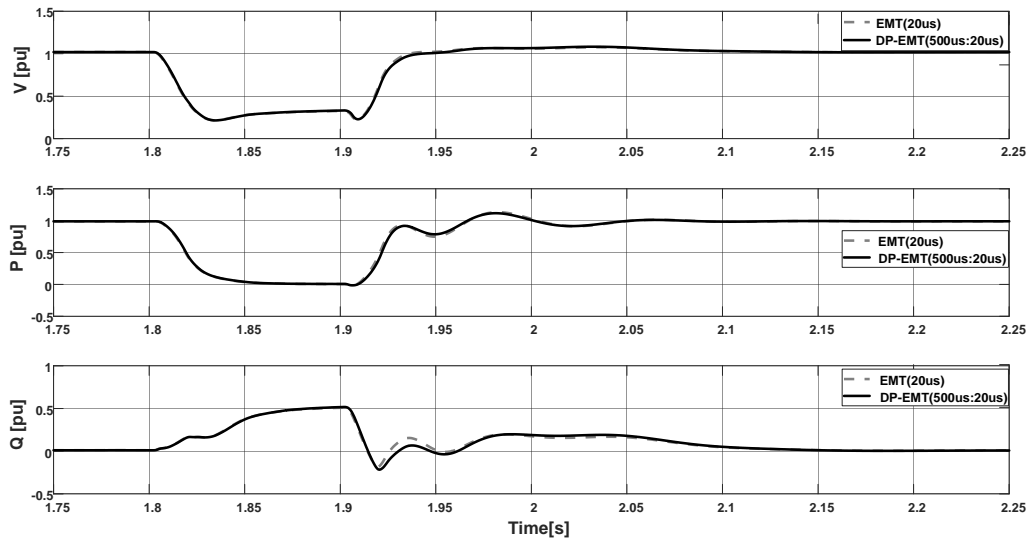


Figure 5-8 Terminal voltage (rms, fundamental), and real and reactive power at the windfarm terminal for EMT (20- μ s) and DP-EMT (500- μ s:20- μ s) simulations

5.3 Simulation Example 1

5.3.1 Speed-Up Gain

Total CPU time required to simulate a 3 second time duration is recorded and tabulated in Table 5-3. The simulations are conducted on a computer with a 2.7 GHz Intel® Core™ i7-4600U central processing unit. It must be noted that the speed-up gain shown in the table is due to the reduction of the number of floating point operations required to simulate the external subsystem (i.e., the DP side). The overall speed is still heavily contributed to by the EMT side, where detailed representation of power electronic switching events in the wind farm converters consumes considerable time. In fact, replacement of the wind-farm in the considered network with a controlled and dynamically-adjusted voltage source resulted in a speed-gain of more than 21, which is due the simplified switching converter model.

Table 5-3 Simulation time comparison

| Simulator | Time taken for a 3 s simulation |
|---------------------------|--|
| EMT for the whole network | 694 s |
| DP-EMT | 132 s |
| Simulation time gain | $694/132 = 5.26$ |
| DP-EMT(voltage source) | 32 s |
| Simulation time gain | $694/32 = 21.69$ |

5.4 Simulation Example 2

In this example, the IEEE 39-bus system is studied using the multi-rate DP-EMT simulation technique with the MATE formulation described in the Section 4.3.3. Buses 38, 28 and 29 are modeled in EMT and the rest of the network is modeled in the DP as shown in the Figure 5-9. In order to partition the system at bus 26, a lossless line segment with one time-step delay (with respect to the EMT side) is introduced borrowing inductance from the neighbouring transmission lines. Bus 26 is split into three (26_1, 26_2 and 26_3) in order to introduce the DP-EMT interface. The borrowed inductance and capacitance values to build the lossless line segments are small as the required latency is only 20- μ s.

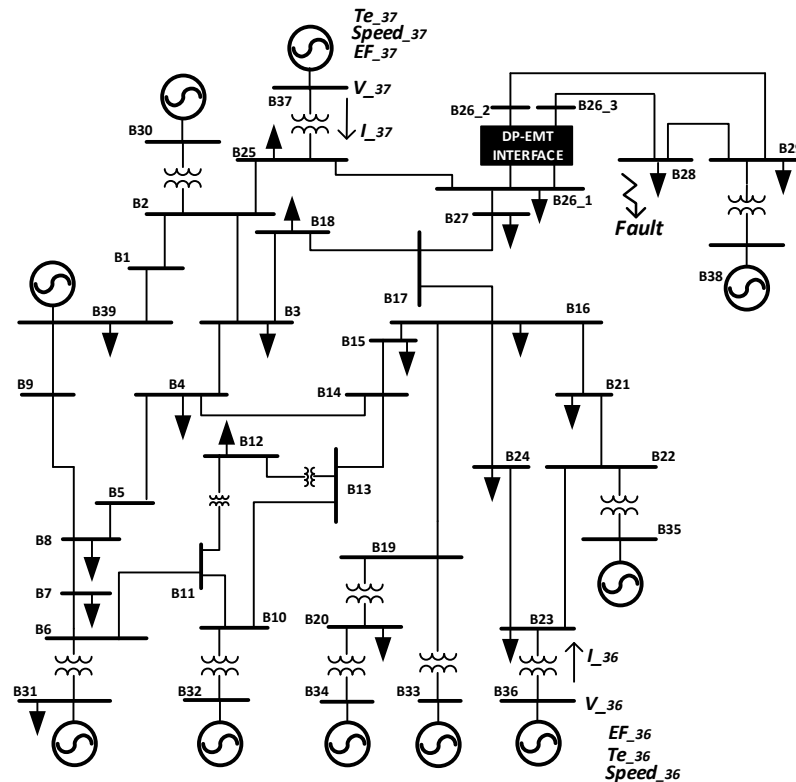


Figure 5-9 IEEE 39-bus system with the DP-EMT interfaces at bus 26

5.4 Simulation Example 2

Alternatively, it is possible to model the entire interfacing transmission line inside the algorithm as shown in Figure 5-10. This will eliminate artificial lossless line segments at the interface.

The voltage source at the EMT side is kept as an infinite bus and the sources at the DP side are represented using synchronous machines. The machines have two poles and are rated at 230 kV, 0.85 power factor, 3600 r/min. The MVA base and the inertia values of each machine are tabulated in the Table 5-4.

Table 5-4 Rated values of Machines

| Bus Numbers | Base [MVA] | Inertia [s] |
|-------------|------------|-------------|
| 30 | 325 | 3.6 |
| 31,32,33,35 | 835 | 5.6 |
| 34, 36, 37 | 635 | 4.6 |
| 39 | 1200 | 7.6 |

Further, all the machines in the study system are used following common per-unit impedance parameters [64]:

$$r_s = 0.003 \text{ pu}, X_{ls} = 0.19 \text{ pu}, X_{mq} = 1.61 \text{ pu}, r'_{kq1} = 0.00178 \text{ pu}, X'_{lkq1} = 0.8125 \text{ pu},$$

$$r'_{kq2} = 0.00841 \text{ pu}, X'_{lkq2} = 0.0939 \text{ pu}, X_{md} = 1.61 \text{ pu}, r'_{fd} = 0.000929 \text{ pu}, X'_{lfd} = 0.1414 \text{ pu},$$

$$r'_{kd} = 0.001334 \text{ pu}, X'_{lkd} = 0.08125 \text{ pu}$$

Machines are represented by the CP-VBR model discussed in Section 5.2. Each machine uses an automatic voltage regulator (AVR) comprising of simple proportional-integral (PI) controllers and a simple excitation system as shown in Figure 5-11. Table 5-5 tabulates the parameter set used for the AVR and excitation system. The governor responses of the

5.4 Simulation Example 2

machines are not considered and the mechanical torque of the machines are maintained at the initial value throughout the simulation.

Table 5-5 AVR and excitation system parameters

| Parameter | Value |
|------------------------|-----------|
| T_R | 0.02 |
| K_p | 0.5 |
| T_i | 3.0 |
| U_{Rmax}, U_{Rmin} | 1.0, -1.0 |
| EFD_{max}, EFD_{min} | 1.0, 0.1 |
| K_E | 1.0 |
| T_E | 0.01 |

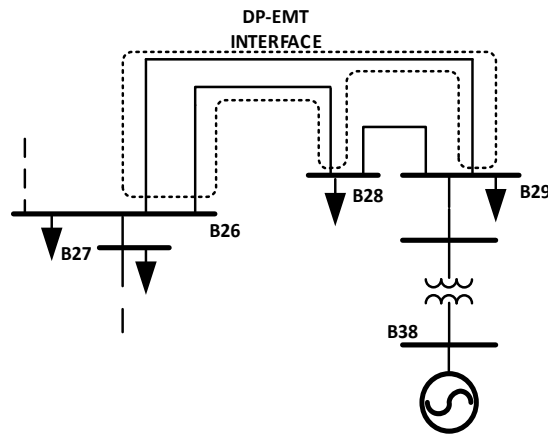


Figure 5-10 DP-EMT interface (only part of the network is shown)

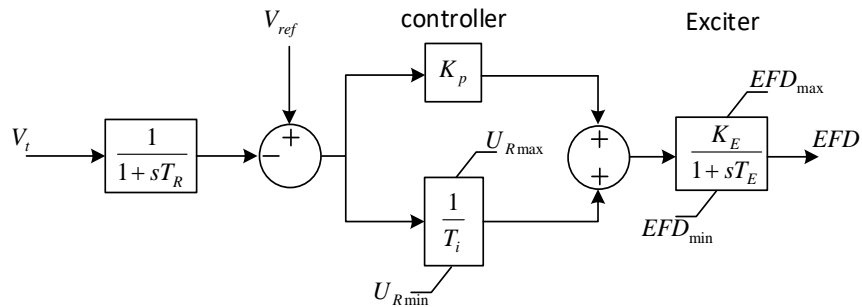


Figure 5-11 Simple PI-based AVR and excitation system

5.4 Simulation Example 2

The simulation results shown in Figure 5-12 and Figure 5-13 represent the waveforms at machines 36 and 37 upon a line-to-ground fault at bus 28 cleared by tripping the line between buses 28 and 26_3 after 8 cycles. Three runs of multi-rate DP-EMT simulations are carried out by varying the DP time-step as 20- μ s, 200- μ s and 1000- μ s. The EMT-side time-step is kept at 20- μ s for all three simulations.

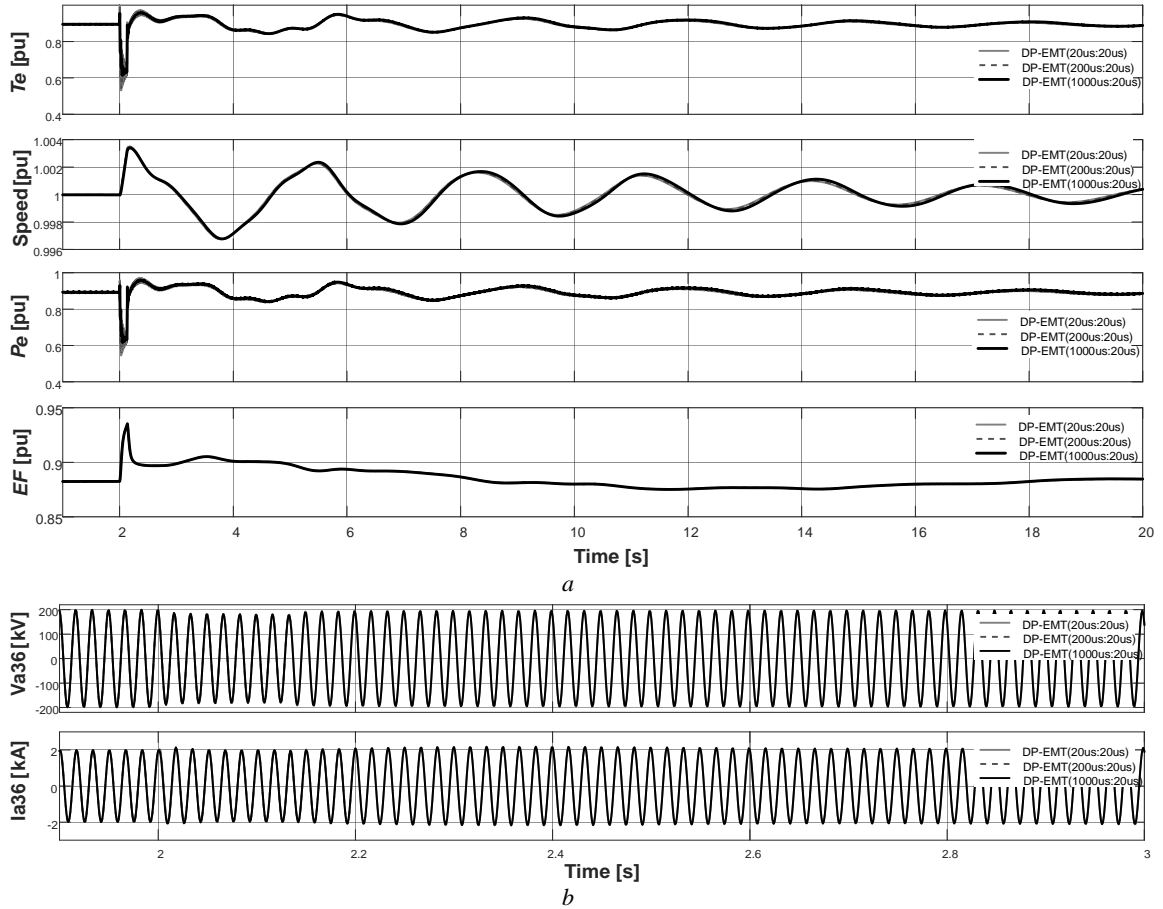


Figure 5-12 Waveforms at the synchronous machine at bus 36

a. Generator (bus 36) electro-mechanical quantities for time-step ratio 20- μ s:20- μ s , 200- μ s:20- μ s and 1000- μ s:20- μ s.

b. Instantaneous voltage and current waveforms (phase-a) at the generator terminal (bus 36) for time-step ratio 20- μ s:20- μ s , 200- μ s:20- μ s and 1000- μ s:20- μ s.

5.4 Simulation Example 2

In this exercise, the waveforms of the single time-step DP-EMT co-simulation (i.e., 20- μ s:20- μ s) are considered as the benchmark solution. Second (i.e., 200- μ s:20- μ s) and third (i.e., 1000- μ s:20- μ s) simulations use the MATE technique with interpolation. The multi-rate DP-EMT traces clearly show close conformity with the single-step DP-EMT traces. Therefore, this confirms that the proposed simulation technique introduces negligible inaccuracies on slower electro-mechanical transients.

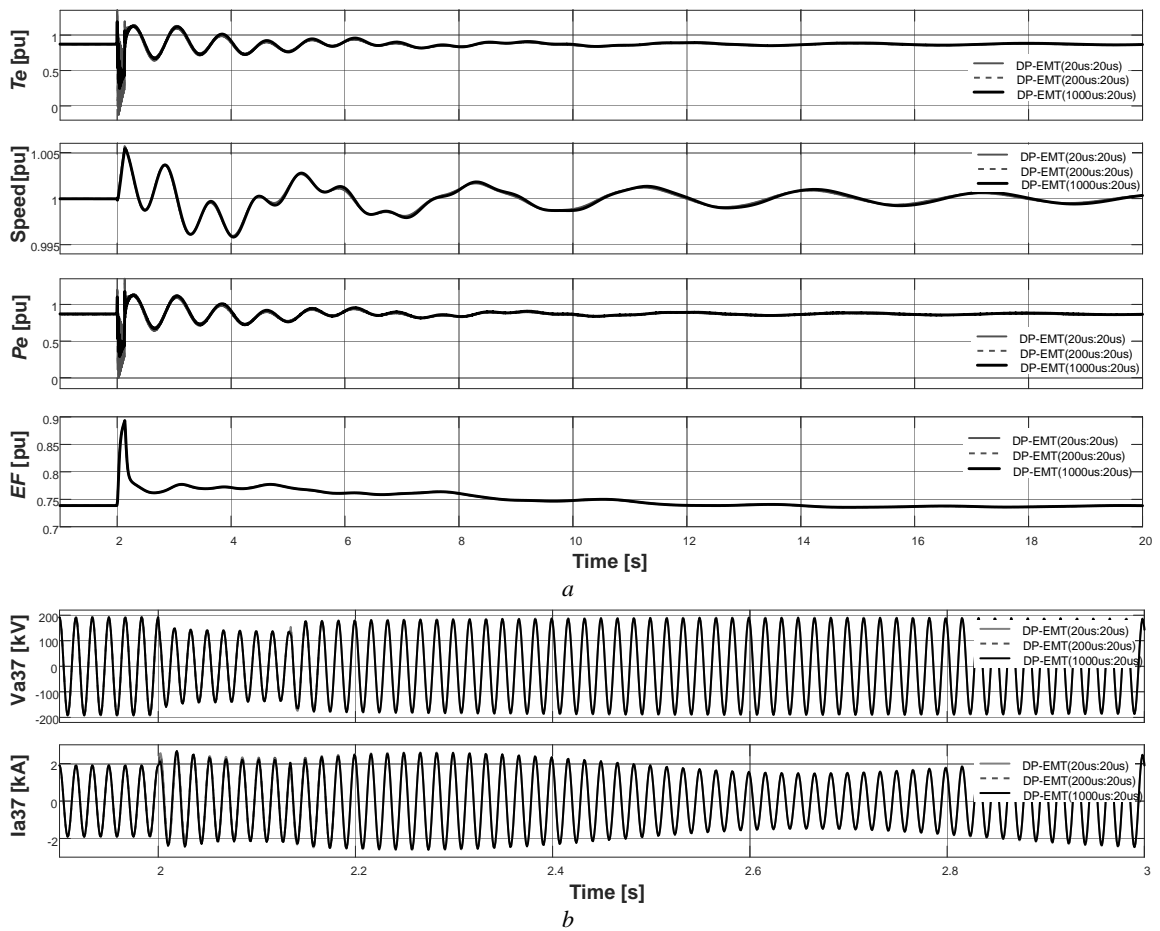


Figure 5-13 Waveforms at the synchronous machine at bus 37

a. Generator (bus 37) electro-mechanical quantities for time-step ratio 20- μ s:20- μ s , 200- μ s:20- μ s and 1000 μ s:20- μ s.

b. Instantaneous voltage and current waveforms (phase-a) at the generator terminal (bus 37) for time-step ratio 20- μ s:20- μ s , 200- μ s:20- μ s and 1000- μ s:20- μ s.

5.4.1 Speed-Up Gain

Simulations are repeated to investigate the variation of computation time with the time-step ratio. The segmented IEEE 39-bus test system discussed in the previous section is simulated for the same disturbance with different DP time-steps keeping the EMT time-step at 20- μ s. Total CPU time required to simulate a 10 s time duration is recorded and plotted against the DP time-step in Figure 5-14.

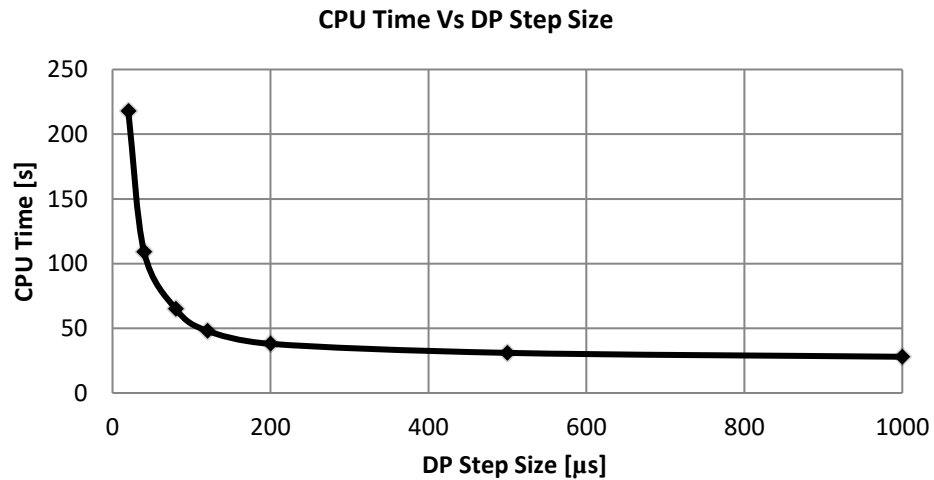


Figure 5-14 CPU Time variation with the DP time-step, IEEE 39-bus system

It is seen that the CPU time decreases significantly with the increment of DP time-step from 20- μ s to 200- μ s, which reduce CPU time from 218 s to 38 s, respectively. Also at the 500- μ s DP time-step, it only needs only 31 s of CPU time. Further increment of DP time-step (beyond 500- μ s) does not show significant reduction in CPU time and shows saturation at a certain minimum level. Hypothetical minimum saturation level is observed when the Thévenin equivalent circuit is indefinitely used at DP side, which represents an

5.4 Simulation Example 2

infinitely large DP time-step. Therefore, the saturation level depends on the size of the Thévenin equivalent system and also the simulation speed of the EMT subsystem.

Speed gain is also impacted by the ratio between the size of the Thévenin equivalent circuit and the size of the external DP system. The size of the Thévenin equivalent circuit depends on the number of interfacing branches between EMT and DP sides. The speed gain increases when the external system is larger and the Thévenin equivalent system is smaller.

For this system, the speed gain is 5.7 with the 200- μ s:20- μ s time-step ratio and 7 with the 500- μ s:20- μ s time-step ratio. Figure 5-14 also shows that the speed-up gain saturates around 7.9 when the DP time-step is increased beyond 500- μ s and speed gain increment when DP time-step increases from 200- μ s to 500- μ s is not significant. Therefore considering both the accuracy and the speed, it is reasonable to consider 5.7 as the effective speed-up gain for this system.

5.4.2 Impact on the Speed-Up Gain of the DP Network

In order to investigate the speed gain variation with the DP subsystem size, the IEEE 118-bus system is considered. The DP-EMT system shown in the Figure 4-10 is studied with a voltage source at the EMT side (infinite bus) and synchronous machines at the DP side. All machines are modeled using the CP-VBR model with the per-unit parameters set presented in Section 5.4. The fault event described in the Section 4.3.4 is applied for different DP time-steps while keeping the EMT time-step at 20- μ s. Total CPU time

5.4 Simulation Example 2

required to simulate a 10 s time duration is recorded and plotted against the DP time-step as shown in Figure 5-15.

Figure 5-15 shows that the required CPU time for the simulation decreases significantly with the increase of the DP time-step. For instance, CPU time decrease from 410 s to 45 s when the DP time-step increased from 20- μ s to 200- μ s. The speed gain achieved at the 200- μ s:20- μ s and 500- μ s:20- μ s time-step ratios are 9.1 and 20.5 respectively. Further, saturation speed-up gain is around 37 for this system.

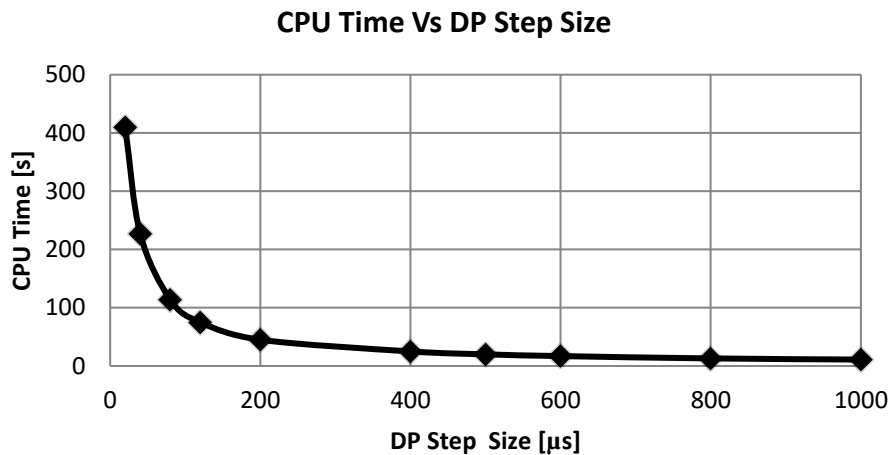


Figure 5-15 CPU Time variation with the DP time-step, IEEE 118-bus system

Chapter 6

Contributions, Conclusions and Recommendations for Future Work

6.1 Introduction

This thesis has contributed to the development of multi-rate co-simulation techniques between electromagnetic transient simulation programs (EMT) and the dynamic phasor (DP) transient simulation programs. Novel algorithms are developed and presented to accurately map the instantaneous signals in EMT to counterpart dynamic phasor samples. The proposed co-simulation approaches in this thesis will help to develop industrial-level DP-EMT co-simulators in the future, which can simulate larger electrical systems more efficiently, maintaining the accuracy and numerical stability. This chapter summarizes the contributions of the thesis and also identifies future research directions.

6.2 Main Contribution of the Thesis

The followings are considered as the main contribution of this thesis:

- 1) This thesis proposed a novel technique to convert an instantaneous real-valued signal into a corresponding dynamic phasor form accurately and efficiently. This approach extracts the entire harmonic contents of an instantaneous real waveform and shifts them altogether to the fundamental-component frame and forms a fully augmented complex signal. This complex signal, which preserves the entire frequency spectrum of the real waveform, is a dynamic phasor. The thesis demonstrated that a DP-EMT simulator that uses this fully augmented fundamental DP is able to exactly replicate EMT simulation results when the same time-step is used in both constituent simulators. The particular signal mapping technique also showed promising results in terms of maintaining the numerical stability of the DP-EMT co-simulator.
- 2) A DP-EMT co-simulation approach was developed by partitioning the electrical network at transmission lines. The equivalent impedance model of a lossless transmission line (common in EMT applications) was adapted as the interface between DP and EMT simulators. The traveling delay of the transmission line was used to develop a multi-rate DP-EMT co-simulation strategy and simulation examples were presented.
- 3) This thesis proposed a novel multi-rate DP-EMT co-simulation approach by adapting the multi-area Thévenin equivalent (MATE) technique. The proposed method first decouples the network equations of the DP and EMT sub-systems at

transmission lines (at least a one-step delay) and then applies the MATE formulation for the DP sub-system to obtain multi-rate solution.

6.2.1 Thesis Publications

The aforementioned contributions have led to the following publications.

- K. Mudunkotuwa, S. Filizadeh, U. Annakkage, “Development of a Hybrid Simulator by Interfacing Dynamic Phasors with Electromagnetic Transient Simulation,” *IET Gener., Transm. & Distrib.*, vol. 11, no. 12, pp. 2991-3001, Sept. 2017.
- K. Mudunkotuwa, S. Filizadeh, “Co-Simulation of Electrical Networks by Interfacing EMT and Dynamic-Phasor Simulators,” *International Conference on Power System Transients (IPST)*, Seoul, June 2017.
- K. Mudunkotuwa, S. Filizadeh, “Co-Simulation of Electrical Networks by Interfacing EMT and Dynamic-Phasor Simulators,” *Electric Power Systems Research (Elsevier)*, Manuscript submitted for publication.

6.3 Conclusions and Future Work

The natural decoupling available at the EMT transmission line interface provides an opportunity to solve the network equations of two sub-systems in two different simulators that use different modeling approaches to simulate electromagnetic transient phenomena. Chapter 3 presented the implementation of DP-EMT co-simulator using a phase domain lossless transmission line model. However, the approach can be applied to any detailed

6.3 Conclusions and Future Work

transmission line model that represents line losses and mutual coupling (e.g., mode-domain transmission line model). In this case, all calculations of the transmission line model and data conversion must be done at the EMT simulator, which runs at a smaller time-step and only the current injection values are passed to the DP side. Despite the fact that accurate transmission line representation is possible, it may be not necessary to maintain such accuracy in the DP-EMT interface as the multi-rate approach will only capture slower transients.

Transmission lines are always available in any power system. Therefore, partitioning at transmission lines is not considered as a major limitation. In cases where a physical transmission line may not exist in the exact location where the network needs to be segmented, a fictitious transmission line segment with one time-step traveling delay can be introduced. Typically this is done by borrowing inductance from neighbouring elements such as transformers. If the time-step of the EMT simulator is small enough (e.g., 20- μ s), then the shunt capacitance required for the fictitious line is very small (e.g., 40-pF), which can be either neglected or obtained from existing elements with shunt capacitance.

The multi-rate DP-EMT simulation strategy using the transmission delay discussed in Chapter 4 has a limitation as the largest time-step achievable in the DP side depends on the traveling delay of the transmission line. However, this approach has high efficiency in terms of the computations. Therefore, this co-simulation approach should be used whenever long transmission lines are available at the interface.

The MATE is a generalised network solution approach that allows the network to be partitioned at arbitrary locations and then obtains the overall solution systematically. Also

the MATE is used for multi-rate simulation in the EMT programs. However, the MATE approach cannot be directly employed in DP-EMT co-simulation as a result of two simulators using different network equation formulations. In particular, the DP and EMT Thévenin equivalent circuits cannot be directly solved to obtain the linking branch currents required in the MATE technique. However, the adapted MATE approach presented in the Chapter 4 removes this barrier as the transmission lines decouple the DP and EMT subsystems and MATE is used only at DP sub-system to achieve a multi-rate solution.

The speed-up gain of the multi-rate DP-EMT simulation depends on a number of factors. The results presented in Chapter 5 showed that the speed-up gain increases with the size of the DP sub-system as a result of complete DP solution being taken at larger steps and intermediate solutions are considered only for the smaller Thévenin equivalent circuit. In case where the EMT sub-system demands higher CPU time, as in the wind-farm example in Chapter 5, then the overall speed-up gain is governed by the EMT side.

6.3.1 Suggestions for Future Work

This research has laid the foundation for the DP and EMT co-simulation. The findings of this research open up further research opportunities in the following areas.

- 1) Applicability of the proposed DP extraction technique in TS-EMT hybrid simulation was briefly verified in Section 3.6.4. This should be further investigated and the possibility of multi-rate TS-EMT interface using MATE approach be explored.
- 2) The thesis showed that the DP simulator can be executed at large time-steps such as 1000- μ s. However, the DP network solution requires a longer computation time than the TS. When the DP network expands a considerable distance from the DP-EMT boundary, the rest of the system may be represented by TS. Therefore, further research should be done on the TS-DP interface.
- 3) The possibility of TS-DP-EMT simulator needs to be explored further. Investigations should be done to develop algorithms to determine the interfacing boundaries automatically, which will minimise the impact on the detailed EMT simulation.
- 4) Additional applications of the novel signal conversion technique should be further investigated.

Bibliography

- [1] D. M. Falcao, E. Kaszkurewicz, and H. L. S. Almeida, "Application of Parallel Processing Techniques to the Simulation of Power System Electromagnetic Transients," *IEEE Trans. on Power Systems*, vol. 8, no. 1, pp. 90-96, Feb. 1993.
- [2] S. Abhyankar, "Development of an Implicitly Coupled Electromechanical and Electromagnetic Transients Simulator for Power Systems," Ph.D. dissertation, Illinois Institute of Technology, 2011.
- [3] V. J. Marandi, V. Dinavahi, K. Strunz, J. A. Martinez, A. Ramirez, "Interfacing Techniques for Transient Stability and Electromagnetic Transient Programs," *IEEE Trans. on Power Delivery*, vol. 24, no. 4, pp. 2385-2395, Sept. 2009.
- [4] S. Chiniforoosh, J. Jatskevich, A. Yazdani, V. Sood, V. Dinavahi, J. A. Martinez, and A. Ramirez, "Definitions and Applications of Dynamic Average Models for Analysis of Power Systems," *IEEE Trans. on Power Delivery*, vol. 25, no. 4, pp. 2655-2669, Oct. 2010.
- [5] H. Ouquelle, L. A. Dessaint, and S. Casoria, "An Average Value Model-Based Design of a Deadbeat Controller for VSC-HVDC Transmission Link," in *Proc. IEEE Power & Energy Society General Meeting*, pp. 1-6, 2009.

- [6] H. Saad, S. Denetiere, J. Mahseredjian, P. Delarue, X. Guillaud, J. Peralta, S. Nguefeu, "Modular Multilevel Converter Models for Electromagnetic Transients," *IEEE Trans. on Power Delivery*, vol. 29, no. 3, pp. 1481-1489, June 2014.
- [7] S. E. M. de Oliveira, and A. G. Massaud, "Modal Dynamic Equivalent for Electric Power Systems I: Theory," *IEEE Trans. on Power Systems*, vol. 3, no. 4, pp. 1731-1737, Nov. 1988.
- [8] U. D. Annakkage, N. K. C. Nair, Y. Liang, A. M. Gole, V. Dinavahi, B. Gustavsen, T. Noda, H. Ghasemi, A. Monti, M. Matar, R. Iravani, and J. A. Martinez, "Dynamic System Equivalents: A Survey of Available Techniques," *IEEE Trans. on Power Delivery*, vol. 27, no. 1, pp. 411-420, Jan. 2012.
- [9] F. Ma, and V. Vittal, "Right-Sized Power System Dynamic Equivalents for Power System Operation," *IEEE Trans. on Power Systems*, vol. 26, no. 4, pp. 1998-2005, Nov. 2011.
- [10] J. M. Zavahir, J. Arrillaga, N. R. Watson, "Hybrid electromagnetic transient simulation with the state variable representation of HVDC converter plant," *IEEE Trans. on Power Delivery*, vol. 8, no. 3, pp. 1591-1598, July 1993.
- [11] X. Wang, P. Zhang, Z. Wang, V. Dinavahi, G. Chang, J. A. Martinez, A. Davoudi, A. Mehrizi-Sani, S. Abhyankar, "Interfacing Issues in Multiagent Simulation for Smart Grid Applications," *IEEE Trans. on Power Delivery*, vol. 28, no. 3, pp. 1918-1927, May 2013.
- [12] J. Mahseredjian, "Merging, Prototyping and Hybrid Tools for Power System Transient Simulation," in *Proc. Power Engineering Society Summer Meeting*, vol. 2, pp. 768-769, 2000.

- [13] IEEE Task Force in Interfacing techniques for Simulation Tools, “Interfacing Power System and ICT Simulators: Challenges, State-of-the-Art and Case Studies,” *IEEE Trans. on Smart Grid*, vol. PP, no. 99, doi: 10.1109/TSG.2016.2542824.
- [14] IEEE PES Task Force1 on Real-Time Simulation of Power and Energy Systems, “Real-Time Simulation Technologies for Power Systems Design, Testing, and Analysis,” *IEEE Power and Energy Technology Systems Journal*, vol. 2, no. 2, pp. 63-73, June 2015.
- [15] B. Asghari, V. Dinavahi, M. Rioual, J. A. Martinez, R. Iravani, “Interfacing Techniques for Electromagnetic Field and Circuit Simulation Programs,” *IEEE Trans. on Power Delivery*, vol. 24, no. 2, pp. 939-950, March 2009.
- [16] H. Vardhan, B. Akin, H. Jin, “A Low-Cost, High-Fidelity Processor-in-the-Loop Platform for Rapid Prototyping of Power Electronics circuits and Motor Drives,” *IEEE Power Electronics Magazine*, vol. 3, no. 2, pp. 18-28, June 2016.
- [17] G. Chongva, S. Filizadeh, “Non-real-time hardware-in-loop electromagnetic transient simulation of microcontroller-based power electronic control systems,” in *Proc. IEEE Power Engineering Society General Meeting*, 2013.
- [18] W. Ren, M. Sloderbeck, V. Dinavahi, S. Filizadeh, A.R. Chevretils, M. Matar, R. Iravani, C. Dufour, J. Belanger, M.O. Faruque, K. Strunz, J.A. Martinez, “Interfacing issues in real-time digital simulators,” *IEEE Trans. on Power Delivery*, vol. 26, no. 2, pp.1221-1230, April 2011.
- [19] V. Venkatasubramanian, “Tools for dynamic analysis of the general large power system using time-varying phasors”, *International Journal of Electrical Power & Energy Systems*, vol. 16, no. 6, pp. 365-376, Dec. 1994.

- [20] P. Zhang, J. R. Martí, H. W. Dommel, "Synchronous Machine Modeling Based on Shifted Frequency Analysis," *IEEE Trans. on Power Systems*, vol. 22, no. 3, pp.1139-1147, Aug. 2007.
- [21] T. H. Demiray, "Simulation of power system dynamics using dynamic phasor models," Ph.D. dissertation, Swiss Federal Institute of Technology, 2008.
- [22] F. Plumier, "Co-simulation of Electromagnetic Transients and Phasor Models of Electric Power Systems," Ph.D. dissertation, University of Liège, 2015.
- [23] K. Strunz, R. Shintaku, F. Gao, "Frequency-Adaptive Network Modeling for Integrative Simulation of Natural and Envelope Waveforms in Power Systems and Circuits," *IEEE Trans. on Circuits and Systems*, vol. 53, no. 12, pp. 2788-2802, Dec. 2006.
- [24] K. M. H. K. Konara, "Interfacing Dynamic Phasor Based System Equivalents to an Electromagnetic Transient Simulation," M.Sc. Thesis, University of Manitoba, 2015.
- [25] D. Shu, X. Xie, V. Dinavahi, C. Zang, X. Ye, Q. Jiang, "Dynamic Phasor Based Interface Model for EMT and Transient Stability Hybrid Simulations," *IEEE Trans. on Power Systems*, DOI: 10.1109/TPWRS.2017.2766269.
- [26] D. Gabor, "Theory of communication," *Journal of the Institution of Electrical Engineers*, vol. 93, no. 26, pp. 429–457, Nov. 1946.
- [27] C. P. Steinmetz, "Complex Quantities and their use in Electrical Engineering," in *Proc. International Electrical Congress, Chicago*, pp. 33–75, 1893.
- [28] A.E Kennelly, "Vector Power in Alternating-Current Circuits," *Transaction of the American Insti. of Elec. Eng.*, vol. XXIX, no. 2, pp.1233-1267, 1910.

- [29] S. R. Sanders, J. M. Noworolski, X. Z. Liu, G. C. Verghese, "Generalized Averaging Method for Power Conversion Circuits," *IEEE Trans. on Power Elec.*, vol. 6, no. 3, pp. 251-259, April 1991.
- [30] V.A Caliskan, G. C. Verghese, A. M. Stanković, "Multifrequency Averaging of DC/DC converters," *IEEE Trans. on Power Elec.*, vol. 14, no. 1, pp. 124-133, January 1999.
- [31] V. Venkatasubramanian, H. Schattler, and J. Zaborszky, "Fast Time-Varying Phasor Analysis in the Balanced Three-Phase Large Electric Power System," *IEEE Trans. on Automatic Control*, vol. 40, no. 11, pp. 1975-1982, Nov. 1995.
- [32] P. Mattavelli, A. M. Stanković, G. C. Verghese, "SSR Analysis with Dynamic Phasor Model of Thyristor-Controlled Series Capacitor," *IEEE Trans. on Power Sys.*, vol. 14, no. 1, pp. 200-208, Feb. 1999.
- [33] S. Henschel, "Analysis of Electromagnetic and Electromechanical Power System Transient with Dynamic phasors," Ph.D. dissertation, University of British Columbia, 1999.
- [34] B. Picinbono, "On Instantaneous Amplitude and Phase of Signals," *IEEE Trans. on Signal Processing*, vol. 45, no. 3, pp. 552-560, March 1997.
- [35] P. Zhang, J. R. Martí, H. W. Dommel, "Shifted-Frequency Analysis for EMTP Simulation of Power-System Dynamics," *IEEE Trans. on Circuits and Systems*, vol. 57, no. 9, pp. 1139-1147, Sept. 2010.
- [36] P. Kundur, *Power System Stability and Control*, McGraw-Hill, New York, 1994.

- [37] J. R. Martí, H. W. Dommel, B. D. Bonatto, A. F. R. Barreto “Shifted Frequency Analysis (SFA) concepts for EMTP modelling and simulation of Power System Dynamics,” in Proc. Power Sys. Comp. Conference (PSCC), Wroclaw, Poland, 2014.
- [38] R. Isermann, M. Munchhof , *Identification of Dynamic Systems*, Springer, 2011.
- [39] W. K. Chen, *The Electrical Engineering Handbook*, R. C. Dorf, Ed. Boca Raton: CRC Press, 2000.
- [40] Juan A. Martinez-Velasco, *Transient Analysis of Power Systems: Solution Techniques, Tools and Applications*, Wiley-IEEE Press, 2014.
- [41] E. S. Kuh, R. A. Rohrer, “The state-variable approach to network analysis,” *Proc. IEEE*, vol. 53, no. 7, pp. 672-686, July 1965.
- [42] C. Dufour, J. Mahseredjian, J. Bélanger, “A Combined State-Space Nodal Method for the Simulation of Power System Transients,” *IEEE Trans. Power Delivery*, vol. 26, no. 2, pp. 928-935, April 2011.
- [43] N. Watson and J. Arrillaga, *Power Systems Electromagnetic Transients Simulation*, IEE Power and Energy Series, The Institution of Engineering and Technology, 2003.
- [44] H.W. Dommel “Digital Computer Solution of Electromagnetic Transients in Single and Multiphase Networks,” *IEEE Trans. on Power App. Syst.*, vol. 88, no. 2, pp. 388–395, April 1969.
- [45] M. Sultan, J. Reeve, R. Adapa, “Combined Transient and Dynamic Analysis of HVDC and FACTS,” *IEEE Trans. on Power Delivery*, vol. 13, no. 4, pp. 1271-1277, Oct. 1998.

- [46] M. D. Heffernan, K. S. Turner, J. Arrillaga, and C. P. Arnold, "Computation of A.C.-D.C. system disturbances: Part I, II, and III," *IEEE Trans. Power App. Syst.*, vol. PAS-100, no. 11, pp. 4341–4363, Nov. 1981.
- [47] A. van der Meer, M. Gibescu, A. van der Meijden, W. Kling, and J. Ferreira, "Advanced Hybrid Transient Stability and EMT Simulation for VSC-HVDC Systems," *IEEE Trans. on Power Delivery*, vol. 30, no. 3, pp. 1057-1066, June. 2015.
- [48] S. Abhyankar, J. Flueck, "Multiphysics Solvers for Implicitly Coupled Electromechanical and Electromagnetic Transients Simulation," in *Proc. IEEE PES T&D Conference and Exposition*, pp. 1-5, 2014.
- [49] PSCAD/EMTDC User's Manual, Manitoba HVDC Research Center, Winnipeg, MB, Canada, 2010.
- [50] P.J. Loughlin, B. Tacer, "On the Amplitude- and Frequency-Modulation Decomposition of Signals," *The Journal of the Acoustical Society of America*, vol. 100, no. 3, pp. 1594-1601, March 1996.
- [51] S.C.D. Roy, B. Kumar, "On Digital Differentiators, Hilbert Transformers, and Half-Band Low-Pass Filters," *IEEE Trans. on Education*, vol. 32, no. 3, pp. 314-318, August 1989.
- [52] A. Semlyen, F. de Leon "Computation of Electro-Magnetic Transients Using Dual or Multiple Time Steps," *IEEE Trans. on Power Systems*, vol. 8, no. 3, pp.1274-1281, Aug. 1993.
- [53] L. R. Linares and J. R. Martí, "Sub-Area Latency in a Real-Time Power Network Simulator," in *Proc. Int. Conf. Power Syst. Transients*, Lisbon, Portugal, pp. 541–545, 1995.

- [54] S. Jiang, U. D. Annakkage, A. M. Gole, "A Platform for Validation of FACTS Models," *IEEE Trans. Power Delivery*, vol. 21, no. 1, pp. 484-491, Jan. 2006.
- [55] 'Illinois Center for a Smarter Electric Grid (ICSEG)', <http://icseg.iti.illinois.edu/ieee-39-bus-system/> and <http://icseg.iti.illinois.edu/ieee-118-bus-system/>, accessed 1 September 2016.
- [56] A. Ibrahim, S. Henschel, H. Dommel and T. Niimura, "Transmission Line Model for Large Step Size Transient Simulations," in *Proc. IEEE Canadian Conference on Electrical and Computer Engineering*, pp. 1191-1194, 1999.
- [57] F. A. Moreira, J.R. Martí, "Latency Techniques for Time-Domain Power System Transients Simulation," *IEEE Trans. on Power Systems*, vol. 20, no. 1, pp. 246-253, February 2005.
- [58] L. Wang, J. Jatskevich, V. Dinavahi, H. W. Dommel, J. A. Martinez, K. Strunz, M. Rioual, G. W. Chang, R. Iravani "Methods of Interfacing Rotating Machine Models in Transient Simulation Programs," *IEEE Trans. Power Delivery*, vol. 25, no. 2, pp. 891-903, April 2010.
- [59] H. Ye, F. Gao, K. Strunz, and Y. Xia, "Multi-Scale Modeling and Simulation of Synchronous Machine in Phase-Domain," in *Proc. IEEE PES Innovative Smart Grid Technologies (ISGT Europe)*, Oct. 2012.
- [60] S. D. Pekarek, O. Wasynczuk, and H. J. Hegner, "An Efficient and Accurate Model for the Simulation and Analysis of Synchronous Machine/Converter Systems," *IEEE Trans. on Energy Conversion*, vol. 13, no. 1, pp. 42-48, March 1998.

- [61] S. D. Pekarek and E. A. Walters, "An Accurate Method of Neglecting Dynamic Saliency of Synchronous Machines in Power Electronic Based Systems," *IEEE Trans. on Energy Conversion*, vol. 14, no. 4, pp. 1177-183, Dec. 1999.
- [62] M. Chapariha, F. Therrien, J. Jatskevich, H. W. Dommel, "Explicit Formulations for Constant-Parameter Voltage-Behind-Reactance Interfacing of Synchronous Machine Models," *IEEE Trans. Energy Conversion*, vol. 28, no. 4, pp. 1053-1063. Dec. 2013.
- [63] Y. Huang, M. Chapariha, F. Therrien, J. Jatskevich, J. R. Marti, "A Constant-Parameter Voltage-Behind-Reactance Synchronous Machine Model Based on Shifted-Frequency Analysis," *IEEE Trans. Energy Conversion*, vol. 30, no. 2, pp. 761-771, June 2015.
- [64] P. C. Krause, O. Wasynczuk, and S. D. Sudhoff, *Analysis of Electric Machines*, 2nd ed. Piscataway, NJ, USA: IEEE Press, 2002.
- [65] Wind Turbines - Part 27-1: Electrical Simulation Models-Wind Turbines, IEC Standard 61400-27-1, ed. 1, Feb. 2015.

Appendix-A: Quasi-Periodic Approach

In this appendix, the dynamic phasor extraction process of a time-varying signal using Quasi-Parodic Fourier approach is graphically presented. Consider the sinusoidal waveform shown in Figure A.1. The $x(t)$ is defined as follows:

$$x(t) = \begin{cases} a_m \cos(\omega_c t) & t \leq t_0 \\ b_m \cos(\omega_c t) & t_0 < t \end{cases} \quad (\text{A-1})$$

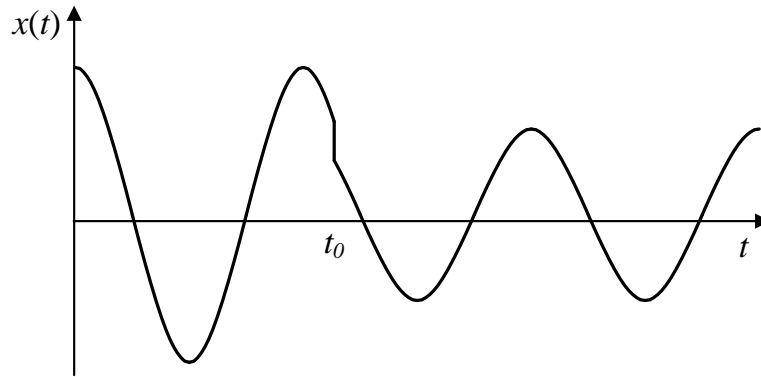


Figure A.1 Test signal with magnitude jump

Figure A.2(a) show four snapshots of the waveform at different time instants of the simulation. Point **P** represents the latest data point that falls into the sliding window, which covers the interval $(\tau - T, \tau]$. Point **P** is always on the right boundary (i.e., $t = \tau$) of the sliding window. In quasi-periodic Fourier approach, at every time-step of the simulation, the signal portion of the $x(t)$ inside the sliding window is assumed to be a periodic waveform, $y(t)$, as shown in Figure A.2(b). The instantaneous values at the point **P** on both waveforms are equal (i.e., $x(\tau) = y(\tau)$). Therefore, if $y(t)$ is represented by a Fourier series,

then the point **P** on the $x(t)$ (i.e., $x(\tau)$) also can be defined by the same Fourier series at t

$= \tau$.

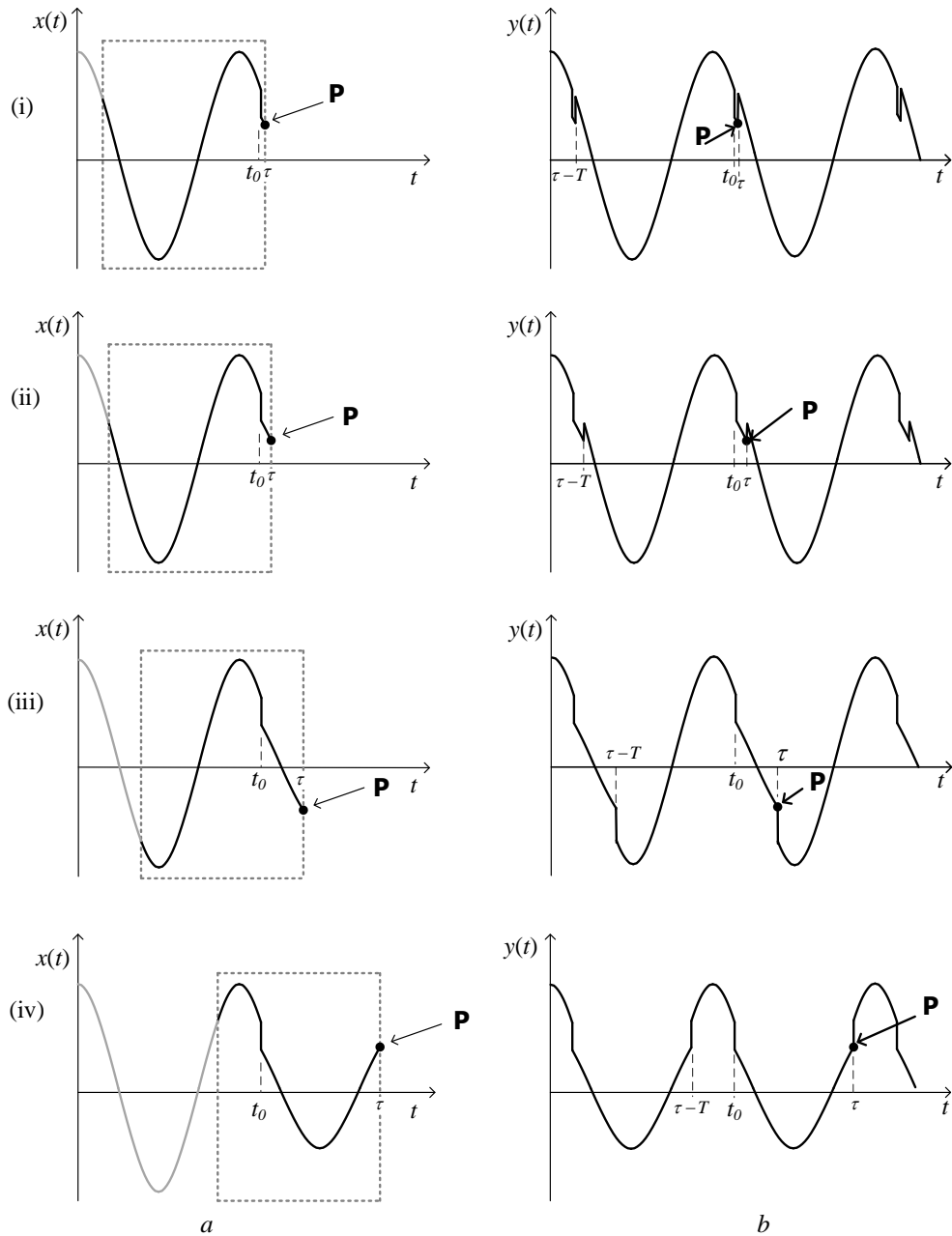


Figure A.2 Snapshots of the sliding window and assumed periodic waveform

a. Sliding window for Fourier coefficients calculation

b. Reconstructed waveform using Fourier coefficients

The periodic function $y(t)$ is defined as follows:

$$y(t) = \begin{cases} x_m \cos(\omega_c t) & \tau - T < t \leq t_0 \\ y_m \cos(\omega_c t) & t_0 < t \leq \tau \end{cases} \quad (\text{A-1})$$

The Fourier series of $y(t)$ is expressed as

$$y(t) = A_0 + \sum_{h=1}^{\infty} A_n \cos(h\omega_c t) + \sum_{h=1}^{\infty} B_n \sin(h\omega_c t), \quad (\text{A-2})$$

where the Fourier coefficients are calculated as follow.

$$\begin{aligned} A_0 &= \frac{x_m}{2\pi} (\sin(\omega_c t_0) - \sin((\tau - T)\omega_c)) + \frac{y_m}{2\pi} (\sin(\omega_c \tau) - \sin(\omega_c t_0)), \\ A_n &= \frac{x_m}{2\pi} \left(\frac{\sin[(n-1)\omega_c t_0]}{(n-1)} + \frac{\sin[(n+1)\omega_c t_0]}{(n+1)} - \frac{\sin[(n-1)(\tau - T)\omega_c]}{(n-1)} - \frac{\sin[(n+1)(\tau - T)\omega_c]}{(n+1)} \right) + \\ &\quad \frac{y_m}{2\pi} \left(\frac{\sin[(n-1)\omega_c \tau]}{(n-1)} + \frac{\sin[(n+1)\omega_c \tau]}{(n+1)} - \frac{\sin[(n-1)\omega_c t_0]}{(n-1)} - \frac{\sin[(n+1)\omega_c t_0]}{(n+1)} \right), \quad (\text{A-3}) \\ B_n &= \frac{x_m}{2\pi} \left(\frac{\cos[(n-1)(\tau - T)\omega_c]}{(n-1)} + \frac{\cos[(n+1)(\tau - T)\omega_c]}{(n+1)} - \frac{\cos[(n-1)\omega_c t_0]}{(n-1)} - \frac{\cos[(n+1)\omega_c t_0]}{(n+1)} \right) + \\ &\quad \frac{y_m}{2\pi} \left(\frac{\sin[(n-1)\omega_c t_0]}{(n-1)} + \frac{\sin[(n+1)\omega_c t_0]}{(n+1)} - \frac{\sin[(n-1)\omega_c \tau]}{(n-1)} - \frac{\sin[(n+1)\omega_c \tau]}{(n+1)} \right). \end{aligned}$$

While the sliding window contains the non-periodic portion of $x(t)$, the point **P** on $y(t)$ has a sudden sharp jump. Therefore, point **P** is practically impossible to capture considering finite number of Fourier terms and this point always has a large error. This is called as *Gibbs phenomenon* which states that a Fourier series cannot approximate a piecewise continuously differentiable periodic functions at jump discontinuities even if the number of series elements goes towards the infinity [38]. For instance, consider the groove in the second subplot of Figure A.2(b). Figure A.3 shows the zoomed plot of this groove. Exact function and truncated Fourier series functions are plotted in the same graph. Three

different truncation levels are considered (i.e., $h_{max}=100, 200$ and 1000). Figure A.3 shows that even with 1000 terms of the Fourier series, it is not possible to represent point **P**. Instead of point **P**, the truncated Fourier series pass through the point **Q** at $t = \tau$, which is located at the mid-point of the sudden jump.

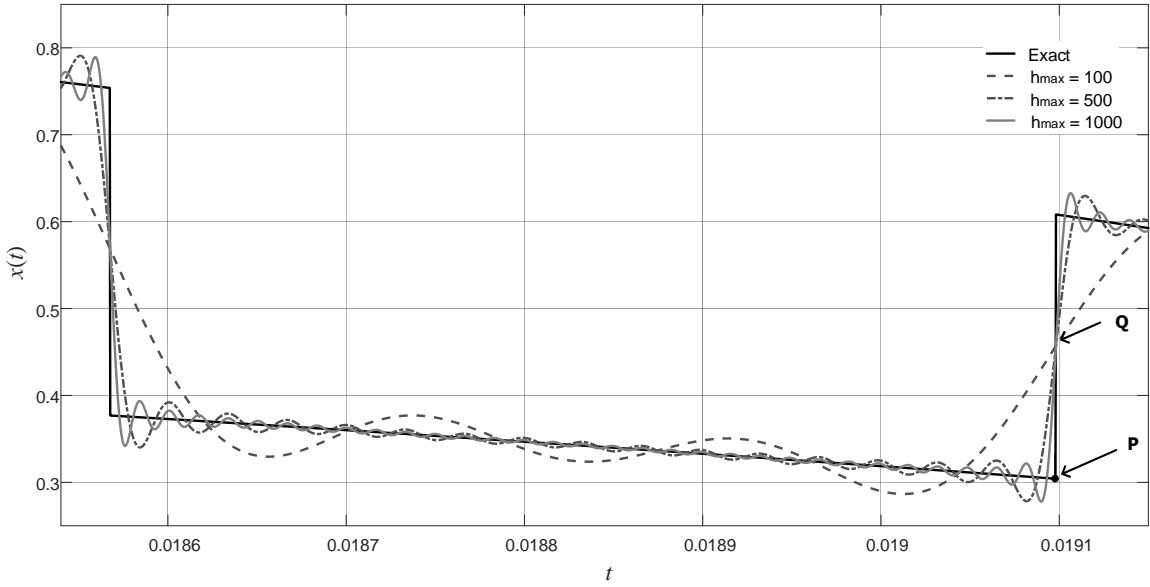


Figure A.3 Instantaneous signal with magnitude jump

The dynamic phasor signal $\mathbf{X}(t)$ of the real signal $x(t)$ can be calculated using the time-varying complex Fourier coefficients as follows:

$$\mathbf{X}(t) = \langle x \rangle_0(t) e^{-j\omega_c t} + 2 \sum_{h=1}^{\infty} \langle x \rangle_h(t) e^{j(h-1)\omega_c t} \quad (\text{A-4})$$

In practical applications, this infinite series has to be truncated to a finite number of terms. Due to the same reasons described in the previous explanation, the dynamic phasor signal $\mathbf{X}(t)$ does not accurately represents the behaviour of $x(t)$ while the sliding window contains the non-periodic portion of the $x(t)$.

Appendix-B: VBR Formulation

The stator voltage equation of the VBR formulation can be expressed as follows [60]:

$$v_{abc} = R_s i_{abc} + \frac{d}{dt} [L''_{abc}(\theta_r) i_{abc}] + e''_{abc} \quad (\text{B-1})$$

where stator resistance and sub-transient inductance matrices are

$$R_s = \begin{bmatrix} r_s & 0 & 0 \\ 0 & r_s & 0 \\ 0 & 0 & r_s \end{bmatrix}, \quad (\text{B-2})$$

$$L''_{abc} = \begin{bmatrix} L_S(2\theta_r) & L_M(2\theta_r - \frac{2\pi}{3}) & L_M(2\theta_r + \frac{2\pi}{3}) \\ L_M(2\theta_r - \frac{2\pi}{3}) & L_S(2\theta_r - \frac{4\pi}{3}) & L_M(2\theta_r) \\ L_M(2\theta_r + \frac{2\pi}{3}) & L_M(2\theta_r) & L_S(2\theta_r + \frac{4\pi}{3}) \end{bmatrix}. \quad (\text{B-3})$$

The entries can be calculated as

$$L_S(x) = L_{ls} + L_a - L_b \cos(x), \quad (\text{B-4})$$

$$L_M(x) = -\frac{L_a}{2} - L_b \cos(x), \quad (\text{B-5})$$

$$L_a = \frac{L''_{mq} + L''_{md}}{3}, L_b = \frac{L''_{md} - L''_{mq}}{3}. \quad (\text{B-6})$$

The inductance L''_{md} and L''_{mq} are calculated by

$$L''_{md} = \left[\frac{1}{L_{md}} + \frac{1}{L_{lfd}} + \frac{1}{L_{lkd}} \right]^{-1}, \quad (\text{B-7})$$

$$L''_{mq} = \left[\frac{1}{L_{mq}} + \frac{1}{L_{llkq1}} + \frac{1}{L_{lkq2}} \right]^{-1}. \quad (\text{B-8})$$

The sub-transient voltages in (B-1) can be calculated as

$$e''_{abcs} = [\mathbf{K}_s^r]^{-1} [e''_q \quad e''_d \quad 0]^T \quad (\text{B-9})$$

where \mathbf{K}_s^r is Park's transformation matrix [64] and

$$e''_q = \omega_r \lambda''_d + \sum_{j=1}^2 \frac{L''_{mq} r_{kj}}{L''_q L''_{lkj}} (\lambda_{mq} - \lambda_{kj}), \quad (\text{B-10})$$

$$e''_d = -\omega_r \lambda''_q + \frac{L''_{md} r_{kd}}{L''_{lkd}} (\lambda_{md} - \lambda_{kd}) + \frac{L''_{md} r_{fd}}{L''_{lfd}} (\lambda_{md} - \lambda_{fd}) + \frac{L''_{md}}{L''_{lfd}} v_{fd}. \quad (\text{B-11})$$

Appendix-C: CP-VBR Formulation

The interfacing equation of the CP-VBR model is given as follows:

$$V_{abcs} = R_s i_{abcs} + L'' \frac{d}{dt} i_{abcs} + e''_{abcs}, \quad (\text{C-1})$$

where the inductance matrix is

$$L'' = \begin{bmatrix} L''_S & L''_M & L''_M \\ L''_M & L''_S & L''_M \\ L''_M & L''_M & L''_S \end{bmatrix} \text{ and the entries are } L''_S = L_{ls} + \frac{2L''_{md}}{3}, \quad L''_M = -\frac{L''_{md}}{3}.$$

The sub-transient voltages are given by

$$e''_{abcs} = [\mathbf{K}_s^r]^{-1} [e''_q \quad e''_d \quad 0]^T, \quad (\text{C-2})$$

where \mathbf{K}_s^r is Park's transformation matrix [64] and

$$e''_q = \frac{L''_d}{L''_q} \left\{ \omega_r (\lambda''_d - (L''_q - L''_d) i_{ds}) + \sum_{j=1}^2 \frac{L''_{mq} r_{kqj}}{L''_q L''_{lkj}} (\lambda_{mq} - \lambda_{kqj}) \right\} + \frac{(L''_q - L''_d)}{L''_q} (\tilde{v}_{qs} - r_s i_{qs}), \quad (\text{C-3})$$

$$e''_d = -\omega_r (\lambda''_q + (L''_q - L''_d) i_{qs}) + \frac{L''_{md} r_{kd}}{L''_{lkd}} (\lambda_{md} - \lambda_{kd}) + \frac{L''_{md} r_{fd}}{L''_{lfd}} (\lambda_{md} - \lambda_{fd}) + \frac{L''_{md}}{L''_{lfd}} v_{fd}. \quad (\text{C-4})$$

The q - and d -axis sub-transient inductances are

$$L''_d = L_{ls} + L''_{md}, \quad L''_q = L_{ls} + L''_{mq}, \quad (\text{C-5})$$

where L''_{md} and L''_{mq} are given in Appendix B.

The rotor state model is given by

$$\frac{d\lambda_j}{dt} = -\frac{r_j}{L_{lj}}(\lambda_j - \lambda_{mq}); \quad j = kq1, kq2, \quad (\text{C-6})$$

$$\frac{d\lambda_j}{dt} = -\frac{r_j}{L_{lj}}(\lambda_j - \lambda_{md}) + v_j; \quad j = fd, kd, \quad (\text{C-7})$$

where λ_j represents the rotor flux linkages.

The electromagnetic torque is calculated by

$$T_e = \frac{3P}{4}(\lambda_{md}i_{qs} - \lambda_{mq}i_{ds}). \quad (\text{C-8})$$

Appendix-D: Mapping between $qd0$ and abc

The stator dynamic phasor quantities are converted to $q-d$ quantities using

$$x_{qd0s} = \mathbf{K}_s^r \Re[\mathbf{X}_{abc} e^{j\omega t}], \quad (\text{D-1})$$

where \mathbf{K}_s^r is Park's transformation matrix as in [64].

The stator sub-transient voltages in $q-d$ reference frame are converted to dynamic phasor quantities using

$$\mathbf{E}_{abc}'' = \mathbf{K}_{u,qd}^{U,abc} \begin{bmatrix} e_q'' \\ e_d'' \end{bmatrix}^T, \quad (\text{D-2})$$

where

$$\mathbf{K}_{u,qd}^{U,abc} = \begin{pmatrix} e^{j(\theta_r - \omega_s t)} & e^{j(\theta_r - \frac{\pi}{2} - \omega_s t)} \\ e^{j(\theta_r - \frac{2\pi}{3} - \omega_s t)} & e^{j(\theta_r - \frac{\pi}{2} - \frac{2\pi}{3} - \omega_s t)} \\ e^{j(\theta_r + \frac{2\pi}{3} - \omega_s t)} & e^{j(\theta_r - \frac{\pi}{2} + \frac{2\pi}{3} - \omega_s t)} \end{pmatrix}. \quad (\text{D-3})$$

Appendix-E: IEEE Test Systems Data

1) IEEE-12 bus system:

In this research, the IEEE-12 system data given in [54] is used. Transmission lines are modeled using PI-Sections. Transformers are represented by series R and L elements and parallel R and L elements are used represent the loads. The entire system is represented at 230 kV level.

Table E - 1 Transmission line (PI-section) parameters, IEEE-12 bus system

| <i>From Bus</i> | <i>To Bus</i> | <i>R</i> [Ω] | <i>L</i> [H] | <i>C</i> [μ F] |
|-----------------|---------------|-----------------------|--------------|---------------------|
| 1 | 2 | 6.05176 | 0.12784 | 0.91565 |
| 1 | 6 | 17.75324 | 0.37403 | 2.78174 |
| 2 | 5 | 17.75324 | 0.37403 | 2.78174 |
| 3 | 4 | 6.05176 | 0.12784 | 0.91565 |
| 3 | 4 | 6.05176 | 0.12784 | 0.91565 |
| 5 | 4 | 17.75324 | 0.37403 | 2.78174 |
| 6 | 4 | 17.75324 | 0.37403 | 2.78174 |
| 7 | 8 | 18.98581 | 0.54345 | 7.32141 |

Table E - 2 Transformer equivalent impedances, IEEE-12 bus system

| <i>From Bus</i> | <i>To Bus</i> | <i>R</i> [Ω] | <i>L</i> [H] |
|-----------------|---------------|-----------------------|--------------|
| 1 | 7 | 0.00000 | 0.01403 |
| 8 | 3 | 0.00000 | 0.01403 |

Table E - 3 Load impedances, IEEE-12 bus system

| <i>Bus</i> | <i>R</i> [Ω] | <i>L</i> [H] |
|------------|-----------------------|--------------|
| 2 | 1058.000 | 14.032 |
| 3 | 264.500 | 1.169 |
| 4 | 440.833 | 2.339 |
| 5 | 529.000 | 2.923 |
| 6 | 120.227 | 0.935 |

Table E - 4 Voltage source parameters, IEEE-12 bus system

| <i>Bus</i> | <i>R</i> [Ω] | <i>L</i> [H] | <i>E</i> [kV] | <i>Phase</i> [deg] | <i>P</i> [MW] | <i>Q</i> [MVA] |
|------------|-----------------------|--------------|---------------|--------------------|---------------|----------------|
| 2 | 0.001 | 0.014032 | 234.60 | 0.10 | 460.00 | 155.88 |
| 1 | 0.001 | 0.014032 | 234.60 | 0.00 | 326.81 | -67.42 |
| 6 | 0.001 | 0.028064 | 236.90 | -25.43 | 400.00 | 185.47 |
| 3 | 0.001 | 0.014032 | 236.90 | -36.31 | 300.00 | 250.61 |

2) IEEE-39 bus system:

In this research, the IEEE-39 system data given in [55] is used. Transmission lines are modeled using PI-Sections. Transformers are represented by a series R and L elements and parallel R and L elements are used represent the loads. Entire system is represented at 230 kV level.

Table E - 5 Transmission line (PI-section) parameters, IEEE-39 bus system

| <i>From Bus</i> | <i>To Bus</i> | <i>R</i> [Ω] | <i>L</i> [H] | <i>C</i> [μ F] |
|-----------------|---------------|-----------------------|--------------|---------------------|
| 1 | 2 | 1.85150 | 0.05767 | 3.50351 |
| 1 | 39 | 0.52900 | 0.03508 | 3.76075 |
| 2 | 3 | 0.68770 | 0.02119 | 1.28969 |
| 2 | 25 | 3.70300 | 0.01207 | 0.73209 |
| 3 | 4 | 0.68770 | 0.02989 | 1.11017 |
| 3 | 18 | 0.58190 | 0.01866 | 1.07206 |
| 4 | 5 | 0.42320 | 0.01796 | 0.67292 |
| 4 | 14 | 0.42320 | 0.01810 | 0.69298 |
| 5 | 6 | 0.10580 | 0.00365 | 0.21762 |
| 5 | 8 | 0.42320 | 0.01572 | 0.74012 |
| 6 | 7 | 0.31740 | 0.01291 | 0.56662 |
| 6 | 11 | 0.37030 | 0.01151 | 0.69649 |
| 7 | 8 | 0.21160 | 0.00645 | 0.39112 |
| 8 | 9 | 1.21670 | 0.05094 | 1.90745 |
| 9 | 39 | 0.52900 | 0.03508 | 6.01720 |
| 10 | 11 | 0.21160 | 0.00603 | 0.36554 |
| 10 | 13 | 0.21160 | 0.00603 | 0.36554 |
| 13 | 14 | 0.47610 | 0.01417 | 0.86397 |
| 14 | 15 | 0.95220 | 0.03045 | 1.83525 |
| 15 | 16 | 0.47610 | 0.01319 | 0.85745 |

| | | | | |
|----|----|---------|---------|---------|
| 16 | 17 | 0.37030 | 0.01249 | 0.67292 |
| 16 | 19 | 0.84640 | 0.02736 | 1.52436 |
| 16 | 21 | 0.42320 | 0.01894 | 1.27765 |
| 16 | 24 | 0.15870 | 0.00828 | 0.34097 |
| 17 | 18 | 0.37030 | 0.01151 | 0.66139 |
| 17 | 27 | 0.68770 | 0.02428 | 1.61261 |
| 21 | 22 | 0.42320 | 0.01965 | 1.28618 |
| 22 | 23 | 0.31740 | 0.01347 | 0.92565 |
| 23 | 24 | 1.16380 | 0.04911 | 1.81017 |
| 25 | 26 | 1.69280 | 0.04532 | 2.57235 |
| 26 | 27 | 0.74060 | 0.02063 | 1.20143 |
| 26 | 28 | 2.27470 | 0.06651 | 3.91218 |
| 26 | 29 | 3.01530 | 0.08770 | 5.15975 |
| 28 | 29 | 0.74060 | 0.02119 | 1.24857 |

Table E - 6 Transformer equivalent impedances, IEEE-39 bus system

| <i>From Bus</i> | <i>To Bus</i> | <i>R</i> [Ω] | <i>L</i> [H] |
|-----------------|---------------|-----------------------|--------------|
| 2 | 30 | 0.00000 | 0.02540 |
| 6 | 31 | 0.00000 | 0.03508 |
| 10 | 32 | 0.00000 | 0.02806 |
| 11 | 12 | 0.84640 | 0.06104 |
| 12 | 13 | 0.84640 | 0.06104 |
| 19 | 20 | 0.37030 | 0.01936 |
| 19 | 33 | 0.37030 | 0.01993 |
| 20 | 34 | 0.47610 | 0.02526 |
| 22 | 35 | 0.00000 | 0.02007 |
| 23 | 36 | 0.26450 | 0.03817 |
| 25 | 37 | 0.31740 | 0.03255 |
| 29 | 38 | 0.42320 | 0.02189 |

Table E - 7 Load impedances, IEEE-39 bus system

| <i>Bus</i> | <i>R</i> [Ω] | <i>L</i> [H] |
|------------|-----------------------|--------------|
| 3 | 164.2857 | 58.4673 |
| 4 | 105.8000 | 0.7626 |
| 7 | 226.2618 | 1.6705 |
| 8 | 101.3410 | 0.7973 |
| 12 | 7053.3333 | 1.5946 |
| 15 | 165.3125 | 0.9171 |

| | | |
|----|-----------|---------|
| 16 | 160.5950 | 4.3443 |
| 18 | 334.8101 | 4.6774 |
| 20 | 77.7941 | 1.3623 |
| 21 | 193.0657 | 1.2202 |
| 23 | 213.7374 | 1.6586 |
| 24 | 171.4193 | -1.5219 |
| 25 | 236.1607 | 2.9729 |
| 26 | 380.5755 | 8.2542 |
| 27 | 188.2562 | 1.8586 |
| 28 | 256.7961 | 5.0841 |
| 29 | 186.5961 | 5.2164 |
| 31 | 5750.0000 | 30.5047 |
| 39 | 47.9167 | 0.5613 |

Table E - 8 Shunt (capacitive) impedances, IEEE-39 bus system

| <i>Bus</i> | <i>C</i> [μ F] |
|------------|---------------------|
| 4 | 5.014333 |
| 5 | 10.02867 |

Table E - 9 Voltage source parameters, IEEE-39 bus system

| <i>Bus</i> | <i>R</i> [Ω] | <i>L</i> [H] | <i>E</i> [kV] | <i>Phase</i> [deg] | <i>P</i> [MW] | <i>Q</i> [MVA] |
|------------|-----------------------|--------------|---------------|--------------------|---------------|----------------|
| 30 | 0.001 | 0.028064 | 240.93 | -5.26 | 250.00 | 123.84 |
| 31 | 0.001 | 0.028064 | 234.60 | -1.59 | 574.42 | 129.29 |
| 32 | 0.001 | 0.028064 | 230.00 | 0.49 | 650.00 | 65.36 |
| 33 | 0.001 | 0.028064 | 239.20 | 1.32 | 632.00 | 131.34 |
| 34 | 0.001 | 0.028064 | 241.50 | 0.01 | 508.00 | 161.51 |
| 35 | 0.001 | 0.028064 | 241.34 | 3.83 | 650.00 | 212.65 |
| 36 | 0.001 | 0.028064 | 244.61 | 6.66 | 560.00 | 191.52 |
| 37 | 0.001 | 0.028064 | 236.39 | 0.61 | 540.00 | -8.36 |
| 38 | 0.001 | 0.028064 | 236.10 | 6.2 | 830.00 | 32.50 |
| 39 | 0.001 | 0.028064 | 236.90 | -11.94 | 1000.00 | 132.36 |

3) IEEE-118 bus system:

In this research, the IEEE-118 system data given in [55] is used. Transmission lines are modeled using PI-Sections. Transformers are represented by a series R and L elements and parallel R and L elements are used represent the loads. Entire system is represented at 230 kV level.

Table E - 10 Transmission line (PI-section) parameters, IEEE-39 bus system

| <i>From Bus</i> | <i>To Bus</i> | <i>R</i> [Ω] | <i>L</i> [H] | <i>C</i> [μ F] |
|-----------------|---------------|-----------------------|--------------|---------------------|
| 1 | 2 | 16.02870 | 0.14018 | 0.12736 |
| 1 | 3 | 6.82410 | 0.05950 | 0.05426 |
| 2 | 12 | 9.89230 | 0.08644 | 0.07883 |
| 3 | 5 | 12.74890 | 0.15155 | 0.14241 |
| 3 | 12 | 25.60360 | 0.22451 | 0.20358 |
| 4 | 5 | 0.93104 | 0.01120 | 0.01053 |
| 4 | 11 | 11.05610 | 0.09654 | 0.08765 |
| 5 | 6 | 6.29510 | 0.07577 | 0.07150 |
| 5 | 11 | 10.73870 | 0.09570 | 0.08715 |
| 6 | 7 | 2.42811 | 0.02919 | 0.02758 |
| 7 | 12 | 4.55998 | 0.04771 | 0.04383 |
| 8 | 9 | 1.29076 | 0.04280 | 5.82666 |
| 8 | 30 | 2.27999 | 0.07072 | 2.57737 |
| 9 | 10 | 1.36482 | 0.04518 | 6.16763 |
| 11 | 12 | 3.14755 | 0.02750 | 0.02517 |
| 11 | 13 | 11.77025 | 0.10258 | 0.09407 |
| 12 | 14 | 11.37350 | 0.09921 | 0.09106 |
| 12 | 16 | 11.21480 | 0.11703 | 0.10731 |
| 12 | 117 | 17.40410 | 0.19645 | 0.17951 |
| 13 | 15 | 39.35760 | 0.34295 | 0.31430 |
| 14 | 15 | 31.47550 | 0.27363 | 0.25172 |
| 15 | 17 | 6.98280 | 0.06132 | 0.22264 |
| 15 | 19 | 6.34800 | 0.05529 | 0.05064 |
| 15 | 33 | 20.10200 | 0.17456 | 0.16016 |
| 16 | 17 | 24.01660 | 0.25272 | 0.23367 |
| 17 | 18 | 6.50670 | 0.07086 | 0.06509 |
| 17 | 31 | 25.07460 | 0.21932 | 0.20007 |
| 17 | 113 | 4.82977 | 0.04224 | 0.03851 |
| 18 | 19 | 5.91951 | 0.06918 | 0.05726 |

| | | | | |
|----|-----|----------|---------|---------|
| 19 | 20 | 13.33080 | 0.16418 | 0.14943 |
| 19 | 34 | 39.78080 | 0.34659 | 0.31691 |
| 20 | 21 | 9.68070 | 0.11913 | 0.10831 |
| 21 | 22 | 11.05610 | 0.13611 | 0.12335 |
| 22 | 23 | 18.09180 | 0.22311 | 0.20258 |
| 23 | 24 | 7.14150 | 0.06904 | 0.24971 |
| 23 | 25 | 8.25240 | 0.11226 | 0.43324 |
| 23 | 32 | 16.76930 | 0.16179 | 0.58818 |
| 24 | 70 | 1.16909 | 0.57742 | 0.51136 |
| 24 | 72 | 25.81520 | 0.27503 | 0.24470 |
| 25 | 27 | 16.82220 | 0.22872 | 0.88453 |
| 26 | 30 | 4.22671 | 0.12068 | 4.55301 |
| 27 | 28 | 10.11977 | 0.11997 | 0.10831 |
| 27 | 32 | 12.11410 | 0.10594 | 0.09658 |
| 27 | 115 | 8.67560 | 0.10398 | 0.09888 |
| 28 | 29 | 12.53730 | 0.13232 | 0.11934 |
| 29 | 31 | 5.71320 | 0.04645 | 0.04162 |
| 30 | 38 | 2.45456 | 0.07577 | 2.11605 |
| 31 | 32 | 15.76420 | 0.13822 | 0.12586 |
| 32 | 113 | 32.53350 | 0.28485 | 0.25974 |
| 32 | 114 | 7.14150 | 0.08588 | 0.08163 |
| 33 | 37 | 21.95350 | 0.19926 | 0.18352 |
| 34 | 36 | 4.60759 | 0.03761 | 0.02848 |
| 34 | 37 | 1.35424 | 0.01319 | 0.04934 |
| 34 | 43 | 21.84770 | 0.23588 | 0.21191 |
| 35 | 36 | 1.18496 | 0.01431 | 0.01344 |
| 35 | 37 | 5.81900 | 0.06974 | 0.06609 |
| 37 | 39 | 16.98090 | 0.14874 | 0.13539 |
| 37 | 40 | 31.36970 | 0.23574 | 0.21060 |
| 38 | 65 | 4.76629 | 0.13836 | 5.24499 |
| 39 | 40 | 9.73360 | 0.08489 | 0.07782 |
| 40 | 41 | 7.67050 | 0.06834 | 0.06128 |
| 40 | 42 | 29.35950 | 0.25679 | 0.23367 |
| 41 | 42 | 21.68900 | 0.18943 | 0.17249 |
| 42 | 49 | 37.82350 | 0.45324 | 0.43123 |
| 43 | 44 | 32.16320 | 0.34435 | 0.30427 |
| 44 | 45 | 11.84960 | 0.12643 | 0.11232 |
| 45 | 46 | 21.16000 | 0.19028 | 0.16648 |
| 45 | 49 | 36.18360 | 0.26100 | 0.22264 |
| 46 | 47 | 20.10200 | 0.17821 | 0.15845 |
| 46 | 48 | 31.79290 | 0.26521 | 0.23668 |

| | | | | |
|----|-----|----------|---------|---------|
| 47 | 49 | 10.10390 | 0.08770 | 0.08043 |
| 47 | 69 | 44.64760 | 0.38981 | 0.35562 |
| 48 | 49 | 9.46910 | 0.07086 | 0.06308 |
| 49 | 50 | 14.12430 | 0.10552 | 0.09397 |
| 49 | 51 | 25.70940 | 0.19224 | 0.17149 |
| 49 | 54 | 45.97010 | 0.40834 | 0.36605 |
| 49 | 66 | 9.52200 | 0.12896 | 0.12436 |
| 49 | 69 | 52.10650 | 0.45464 | 0.41519 |
| 50 | 57 | 25.07460 | 0.18803 | 0.16648 |
| 51 | 52 | 10.73870 | 0.08251 | 0.07000 |
| 51 | 58 | 13.48950 | 0.10089 | 0.08966 |
| 52 | 53 | 21.42450 | 0.22943 | 0.20348 |
| 53 | 54 | 13.91270 | 0.17119 | 0.15544 |
| 54 | 55 | 8.94010 | 0.09921 | 0.10129 |
| 54 | 56 | 1.45475 | 0.01340 | 0.03670 |
| 54 | 59 | 26.60870 | 0.32176 | 0.29986 |
| 55 | 56 | 2.58152 | 0.02119 | 0.01875 |
| 55 | 59 | 25.06931 | 0.30281 | 0.28311 |
| 56 | 57 | 18.14470 | 0.13555 | 0.12135 |
| 56 | 58 | 18.14470 | 0.13555 | 0.12135 |
| 56 | 59 | 42.47870 | 0.33537 | 0.26877 |
| 59 | 60 | 16.76930 | 0.20347 | 0.18854 |
| 59 | 61 | 17.35120 | 0.21048 | 0.19456 |
| 60 | 61 | 1.39656 | 0.01894 | 0.07301 |
| 60 | 62 | 6.50670 | 0.07872 | 0.07361 |
| 61 | 62 | 4.35896 | 0.05276 | 0.04914 |
| 62 | 66 | 25.49780 | 0.30590 | 0.28983 |
| 62 | 67 | 13.64820 | 0.16418 | 0.15544 |
| 63 | 64 | 0.90988 | 0.02806 | 1.08310 |
| 64 | 65 | 1.42301 | 0.04238 | 1.90545 |
| 65 | 68 | 0.73002 | 0.02245 | 3.19914 |
| 66 | 67 | 11.84960 | 0.14243 | 0.13448 |
| 68 | 81 | 0.92575 | 0.02834 | 4.05158 |
| 68 | 116 | 0.17986 | 0.00568 | 0.82235 |
| 69 | 70 | 15.87000 | 0.17821 | 0.61175 |
| 69 | 75 | 21.42450 | 0.17119 | 0.62178 |
| 69 | 77 | 16.34610 | 0.14172 | 0.52049 |
| 70 | 71 | 4.66578 | 0.04981 | 0.04403 |
| 70 | 74 | 21.21290 | 0.18565 | 0.16888 |
| 70 | 75 | 22.64120 | 0.19785 | 0.18052 |
| 71 | 72 | 23.59340 | 0.25258 | 0.22284 |

| | | | | |
|----|-----|----------|---------|---------|
| 71 | 73 | 4.58114 | 0.06371 | 0.05907 |
| 74 | 75 | 6.50670 | 0.05697 | 0.05185 |
| 75 | 77 | 31.79290 | 0.28050 | 0.24961 |
| 75 | 118 | 7.67050 | 0.06749 | 0.06007 |
| 76 | 77 | 23.48760 | 0.20768 | 0.18453 |
| 76 | 118 | 8.67560 | 0.07633 | 0.06799 |
| 77 | 78 | 1.98904 | 0.01740 | 0.06338 |
| 77 | 80 | 15.55260 | 0.14734 | 0.11433 |
| 77 | 82 | 15.76420 | 0.11969 | 0.40987 |
| 78 | 79 | 2.88834 | 0.03424 | 0.03249 |
| 79 | 80 | 8.25240 | 0.09879 | 0.09377 |
| 80 | 96 | 18.83240 | 0.25539 | 0.24771 |
| 80 | 97 | 9.68070 | 0.13106 | 0.12736 |
| 80 | 98 | 12.59020 | 0.15155 | 0.14341 |
| 80 | 99 | 24.01660 | 0.28906 | 0.27378 |
| 82 | 83 | 5.92480 | 0.05143 | 0.19034 |
| 82 | 96 | 8.56980 | 0.07437 | 0.27278 |
| 83 | 84 | 33.06250 | 0.18522 | 0.12937 |
| 83 | 85 | 22.74700 | 0.20768 | 0.17450 |
| 84 | 85 | 15.97580 | 0.08995 | 0.06188 |
| 85 | 86 | 18.51500 | 0.17260 | 0.13840 |
| 85 | 88 | 10.58000 | 0.14313 | 0.13840 |
| 85 | 89 | 12.64310 | 0.24276 | 0.23567 |
| 86 | 87 | 14.96012 | 0.29103 | 0.22314 |
| 88 | 89 | 7.35310 | 0.09991 | 0.09698 |
| 89 | 90 | 12.59020 | 0.13990 | 0.53152 |
| 89 | 92 | 20.78970 | 0.22185 | 0.20759 |
| 90 | 91 | 13.43660 | 0.11731 | 0.10731 |
| 91 | 92 | 20.47230 | 0.17849 | 0.16387 |
| 92 | 93 | 13.64820 | 0.11899 | 0.10931 |
| 92 | 94 | 25.44490 | 0.22171 | 0.20358 |
| 92 | 100 | 34.27920 | 0.41395 | 0.23668 |
| 92 | 102 | 6.50670 | 0.07844 | 0.07341 |
| 93 | 94 | 11.79670 | 0.10272 | 0.09407 |
| 94 | 95 | 6.98280 | 0.06090 | 0.05566 |
| 94 | 96 | 14.23010 | 0.12194 | 0.11533 |
| 94 | 100 | 9.41620 | 0.08139 | 0.30287 |
| 95 | 96 | 9.04590 | 0.07676 | 0.07391 |
| 96 | 97 | 9.15170 | 0.12418 | 0.12034 |
| 98 | 100 | 21.00130 | 0.25118 | 0.23868 |
| 99 | 100 | 9.52200 | 0.11408 | 0.10831 |

| | | | | |
|-----|-----|----------|---------|---------|
| 100 | 101 | 14.65330 | 0.17709 | 0.16447 |
| 100 | 103 | 8.46400 | 0.07367 | 0.26877 |
| 100 | 104 | 23.85790 | 0.28626 | 0.27128 |
| 100 | 106 | 32.00450 | 0.32134 | 0.31089 |
| 101 | 102 | 13.01340 | 0.15716 | 0.14742 |
| 103 | 104 | 24.65140 | 0.22227 | 0.20408 |
| 103 | 105 | 28.30150 | 0.22802 | 0.20458 |
| 103 | 110 | 20.66274 | 0.25440 | 0.23116 |
| 104 | 105 | 5.25826 | 0.05304 | 0.04944 |
| 105 | 106 | 7.40600 | 0.07676 | 0.07191 |
| 105 | 107 | 28.03700 | 0.25679 | 0.23668 |
| 105 | 108 | 13.80690 | 0.09865 | 0.09246 |
| 106 | 107 | 28.03700 | 0.25679 | 0.23668 |
| 108 | 109 | 5.55450 | 0.04041 | 0.03811 |
| 109 | 110 | 14.70620 | 0.10693 | 0.10129 |
| 110 | 111 | 11.63800 | 0.10594 | 0.10029 |
| 110 | 112 | 13.06630 | 0.08981 | 0.31089 |
| 114 | 115 | 1.21670 | 0.01459 | 0.01384 |

Table E - 11 Transformer equivalent impedances, IEEE-118 bus system

| <i>From Bus</i> | <i>To Bus</i> | <i>R</i> [Ω] | <i>L</i> [H] |
|-----------------|---------------|-----------------------|--------------|
| 5 | 8 | - | 0.0267 |
| 17 | 30 | - | 0.0388 |
| 25 | 26 | - | 0.0382 |
| 37 | 38 | - | 0.0375 |
| 59 | 63 | - | 0.0386 |
| 61 | 64 | - | 0.0268 |
| 65 | 66 | - | 0.0370 |
| 68 | 69 | - | 0.0370 |
| 80 | 81 | - | 0.0370 |

Table E - 12 Shunt (inductive/capacitive) impedances, IEEE-118 bus system

| <i>Bus</i> | <i>L</i> [H] | <i>C</i> [μ F] |
|------------|--------------|---------------------|
| 5 | 3.50804 | - |
| 34 | - | 0.70201 |
| 37 | 5.61286 | - |
| 44 | - | 0.50143 |
| 45 | - | 0.50143 |

| | | |
|-----|---|---------|
| 46 | - | 0.50143 |
| 48 | - | 0.75215 |
| 74 | - | 0.60172 |
| 79 | - | 1.00287 |
| 82 | - | 1.00287 |
| 83 | - | 0.50143 |
| 105 | - | 1.00287 |
| 107 | - | 0.30086 |
| 110 | - | 0.30086 |

Table E - 13 Load impedances, IEEE-118 bus system

| <i>Bus</i> | <i>R</i> [Ω] | <i>L</i> [H] |
|------------|-----------------------|--------------|
| 1 | 1037.25 | 5.20 |
| 2 | 2645.00 | 15.59 |
| 3 | 1356.41 | 14.03 |
| 4 | 1356.41 | 11.69 |
| 6 | 1017.31 | 6.38 |
| 7 | 2784.21 | 70.16 |
| 8 | 1889.29 | - |
| 11 | 755.71 | 6.10 |
| 12 | 1125.53 | 14.03 |
| 13 | 1555.88 | 8.77 |
| 14 | 3778.57 | 140.32 |
| 15 | 587.78 | 4.68 |
| 16 | 2116.00 | 14.03 |
| 17 | 4809.09 | 46.77 |
| 18 | 881.67 | 4.13 |
| 19 | 1175.56 | 5.61 |
| 20 | 2938.89 | 46.77 |
| 21 | 3778.57 | 17.54 |
| 22 | 5290.00 | 28.06 |
| 23 | 7557.14 | 46.77 |
| 24 | 4069.23 | - |
| 27 | 745.07 | 10.79 |
| 28 | 3111.76 | 20.05 |
| 29 | 2204.17 | 35.08 |
| 31 | 1230.23 | 5.20 |
| 32 | 896.61 | 6.10 |
| 33 | 2300.00 | 15.59 |
| 34 | 896.61 | 5.40 |

| | | |
|----|---------|-------|
| 35 | 1603.03 | 15.59 |
| 36 | 1706.45 | 8.25 |
| 39 | 1959.26 | 12.76 |
| 40 | 801.52 | 6.10 |
| 41 | 1429.73 | 14.03 |
| 42 | 551.04 | 6.10 |
| 43 | 2938.89 | 20.05 |
| 44 | 3306.25 | 17.54 |
| 45 | 998.11 | 6.38 |
| 46 | 1889.29 | 14.03 |
| 47 | 1555.88 | - |
| 48 | 2645.00 | 12.76 |
| 49 | 608.05 | 4.68 |
| 50 | 3111.76 | 35.08 |
| 51 | 3111.76 | 17.54 |
| 52 | 2938.89 | 28.06 |
| 53 | 2300.00 | 12.76 |
| 54 | 468.14 | 4.39 |
| 55 | 839.68 | 6.38 |
| 56 | 629.76 | 7.80 |
| 57 | 4408.33 | 46.77 |
| 58 | 4408.33 | 46.77 |
| 59 | 190.97 | 1.24 |
| 60 | 678.21 | 46.77 |
| 62 | 687.01 | 10.02 |
| 66 | 1356.41 | 7.80 |
| 67 | 1889.29 | 20.05 |
| 70 | 801.52 | 7.02 |
| 72 | 4408.33 | - |
| 73 | 8816.67 | - |
| 74 | 777.94 | 5.20 |
| 75 | 1125.53 | 12.76 |
| 76 | 777.94 | 3.90 |
| 77 | 867.21 | 5.01 |
| 78 | 745.07 | 5.40 |
| 79 | 1356.41 | 4.39 |
| 80 | 406.92 | 5.40 |
| 82 | 979.63 | 5.20 |
| 83 | 2645.00 | 14.03 |
| 84 | 4809.09 | 20.05 |
| 85 | 2204.17 | 9.35 |

| | | |
|-----|----------|--------|
| 86 | 2519.05 | 14.03 |
| 88 | 1102.08 | 14.03 |
| 90 | 324.54 | 3.34 |
| 91 | 5290.00 | - |
| 92 | 813.85 | 14.03 |
| 93 | 4408.33 | 20.05 |
| 94 | 1763.33 | 8.77 |
| 95 | 1259.52 | 4.53 |
| 96 | 1392.11 | 9.35 |
| 97 | 3526.67 | 15.59 |
| 98 | 1555.88 | 17.54 |
| 99 | 1259.52 | - |
| 100 | 1429.73 | 7.80 |
| 101 | 2404.55 | 9.35 |
| 102 | 10580.00 | 46.77 |
| 103 | 2300.00 | 8.77 |
| 104 | 1392.11 | 5.61 |
| 105 | 1706.45 | 5.40 |
| 106 | 1230.23 | 8.77 |
| 107 | 1058.00 | 11.69 |
| 108 | 26450.00 | 140.32 |
| 109 | 6612.50 | 46.77 |
| 110 | 1356.41 | 4.68 |
| 112 | 777.94 | 10.79 |
| 113 | 8816.67 | - |
| 114 | 6612.50 | 46.77 |
| 115 | 2404.55 | 20.05 |
| 116 | 287.50 | - |
| 117 | 2645.00 | 17.54 |
| 118 | 1603.03 | 9.35 |

Table E - 14 Voltage source parameters, IEEE-118 bus system

| <i>Bus</i> | <i>R</i> [Ω] | <i>L</i> [H] | <i>E</i> [kV] | <i>Phase</i> [deg] | <i>P</i> [MW] | <i>Q</i> [MVA] |
|------------|-----------------------|--------------|---------------|--------------------|---------------|----------------|
| 1 | 0.001 | 0.028064 | 224.07 | 8.66 | 0.00 | 54.07 |
| 4 | 0.001 | 0.028064 | 230.00 | 13.43 | 0.00 | -12.95 |
| 6 | 0.001 | 0.028064 | 230.00 | 11.07 | 0.00 | 32.19 |
| 8 | 0.001 | 0.028064 | 230.00 | 18.97 | 0.00 | 36.53 |
| 10 | 0.001 | 0.028064 | 230.00 | 34.96 | 450.00 | -93.22 |
| 12 | 0.001 | 0.028064 | 230.00 | 10.28 | 85.00 | 59.52 |
| 15 | 0.001 | 0.028064 | 229.13 | 9.07 | 0.00 | 38.83 |

| | | | | | | |
|-----|-------|----------|--------|-------|--------|---------|
| 18 | 0.001 | 0.028064 | 230.00 | 9.40 | 0.00 | 29.30 |
| 19 | 0.001 | 0.028064 | 228.87 | 8.81 | 0.00 | 43.37 |
| 24 | 0.001 | 0.028064 | 230.00 | 19.04 | 0.00 | -3.73 |
| 25 | 0.001 | 0.028064 | 235.84 | 26.32 | 220.00 | -148.80 |
| 26 | 0.001 | 0.028064 | 230.00 | 28.12 | 314.00 | 88.45 |
| 27 | 0.001 | 0.028064 | 230.00 | 13.14 | 0.00 | 43.95 |
| 31 | 0.001 | 0.028064 | 230.00 | 10.64 | 7.00 | 39.50 |
| 32 | 0.001 | 0.028064 | 230.00 | 12.55 | 0.00 | 44.07 |
| 34 | 0.001 | 0.028064 | 230.97 | 8.70 | 0.00 | -41.60 |
| 36 | 0.001 | 0.028064 | 230.00 | 8.26 | 0.00 | 28.53 |
| 40 | 0.001 | 0.028064 | 230.00 | 2.39 | 0.00 | 65.95 |
| 42 | 0.001 | 0.028064 | 230.00 | 1.34 | 0.00 | 56.70 |
| 46 | 0.001 | 0.028064 | 230.00 | 16.43 | 19.00 | 20.87 |
| 49 | 0.001 | 0.028064 | 230.00 | 19.29 | 204.00 | 45.07 |
| 54 | 0.001 | 0.028064 | 230.00 | 11.75 | 48.00 | 61.55 |
| 55 | 0.001 | 0.028064 | 228.80 | 11.71 | 0.00 | 36.11 |
| 56 | 0.001 | 0.028064 | 228.92 | 11.76 | 0.00 | 65.35 |
| 59 | 0.001 | 0.028064 | 230.00 | 18.81 | 155.00 | 64.99 |
| 61 | 0.001 | 0.028064 | 230.00 | 24.06 | 160.00 | -31.10 |
| 62 | 0.001 | 0.028064 | 230.00 | 23.68 | 0.00 | 37.42 |
| 65 | 0.001 | 0.028064 | 230.00 | 27.95 | 391.00 | 206.00 |
| 66 | 0.001 | 0.028064 | 237.04 | 29.01 | 392.00 | -206.14 |
| 69 | 0.001 | 0.028064 | 230.00 | 30.00 | 513.39 | -278.12 |
| 70 | 0.001 | 0.028064 | 226.04 | 21.22 | 0.00 | 35.24 |
| 72 | 0.001 | 0.028064 | 230.00 | 19.13 | 0.00 | -1.75 |
| 73 | 0.001 | 0.028064 | 230.00 | 20.42 | 0.00 | -0.47 |
| 74 | 0.001 | 0.028064 | 218.91 | 20.25 | 0.00 | 53.35 |
| 76 | 0.001 | 0.028064 | 214.45 | 20.17 | 0.00 | 76.11 |
| 77 | 0.001 | 0.028064 | 223.88 | 25.40 | 0.00 | 122.94 |
| 80 | 0.001 | 0.028064 | 230.00 | 29.54 | 477.00 | -112.00 |
| 85 | 0.001 | 0.028064 | 225.72 | 36.21 | 0.00 | 49.83 |
| 87 | 0.001 | 0.028064 | 230.00 | 35.22 | 4.00 | 1.76 |
| 89 | 0.001 | 0.028064 | 230.00 | 46.15 | 607.00 | -63.10 |
| 90 | 0.001 | 0.028064 | 230.00 | 33.63 | 0.00 | 96.23 |
| 91 | 0.001 | 0.028064 | 230.00 | 31.69 | 0.00 | 1.41 |
| 92 | 0.001 | 0.028064 | 223.93 | 29.98 | 0.00 | 81.30 |
| 99 | 0.001 | 0.028064 | 230.00 | 25.60 | 0.00 | 6.64 |
| 100 | 0.001 | 0.028064 | 230.00 | 26.11 | 252.00 | 4.85 |
| 103 | 0.001 | 0.028064 | 230.00 | 22.20 | 40.00 | 17.04 |
| 104 | 0.001 | 0.028064 | 228.55 | 19.16 | 0.00 | 33.54 |
| 105 | 0.001 | 0.028064 | 228.85 | 17.98 | 0.00 | 29.92 |

| | | | | | | |
|-----|-------|----------|--------|-------|-------|--------|
| 107 | 0.001 | 0.028064 | 230.00 | 14.85 | 0.00 | 22.28 |
| 110 | 0.001 | 0.028064 | 229.59 | 15.71 | 0.00 | 27.19 |
| 111 | 0.001 | 0.028064 | 230.00 | 17.37 | 36.00 | -10.92 |
| 112 | 0.001 | 0.028064 | 230.00 | 12.77 | 0.00 | 38.14 |
| 113 | 0.001 | 0.028064 | 230.00 | 11.92 | 0.00 | -35.23 |
| 116 | 0.001 | 0.028064 | 230.00 | 27.32 | 0.00 | 153.89 |